Design of Powder Core Inductors

Håkan Skarrie

LUND UNIVERSITY

Licentiate Thesis
Department of Industrial Electrical Engineering
and Automation

Department of
Industrial Electrical Engineering and Automation
Lund Institute of Technology
Lund University
P.O. Box 118
SE-221 00 LUND
SWEDEN

http://www.iea.lth.se

ISBN 91-88934-19-5
CODEN:LUTEDX/(TEIE-1027)/1-162/(2001)

Printed in Sweden by Universitetstryckeriet
Lund University
Lund 2001

Abstract

In this work an inductor design program is developed. For evaluation of the program two iron powder core inductors with different core materials have been designed. The resulting designs have been manufactured and the inductance and total loss of the inductors are determined by a resonant measurement system and compared to corresponding figures estimated by the program.

In the design program different core materials, core geometries and winding configurations, can be selected from three databases included in the program. Before making a design also the electrical specifications, thermal restrictions etc. are settled. Within defined restrictions the program calculates the optimum design based on the specified parameters and the selected object function.

The expressions used in the program for estimating core and winding losses are thoroughly presented together with the physical background of the different loss parts. For the estimation of hysteresis loss the Preisach model is used. An extension to the model is also suggested to improve the accuracy. The expressions for eddy current and anomalous loss use coefficients determined by loss separation. Skin and proximity effects in the winding becomes apparent at an increasing frequency, these eddy current effects are included in the winding loss equations.

Two iron powder core inductors with different core materials have been designed. Both materials are based on the iron powder Somaloy 500, manufactured by Höganäs AB, Sweden, but with a difference in mixes and heat treatment they experience diverse magnetic and electric properties. The inductors are designed for use as line side filter inductors in a battery charger for charging of electrical vehicles.

The inductors are manufactured and tested in a developed resonant measurement system. The system uses the damped oscillation originating when a charged capacitor, with known parameters, is discharged over an 'unknown'

inductor for determining the inductor parameters, inductance and series resistance. By determining the resistance and measuring the current in the *LCR*-circuit the total loss of the inductor can be estimated. By changing the size of the capacitor the parameters can be determined at different frequencies.

Comparisons between inductance and total loss calculated by the design program respectively measured by the resonant system for the two inductors are presented. The maximum error in the inductance is 3% while the error in the total loss is within 12%. Calculated and measured losses as a function of the current are also compared at some different frequencies. A slight increase in the discrepancy with increasing frequency is observed for the LB1-inductor, i.e. the frequency dependence is somewhat overestimated in the employed loss expression.

Approximate calculations are performed on a laminated core inductor with thick laminates, 0.5 mm. Comparison with the powder core inductors indicate the possibility of reduce inductor size and weight when using a laminated core in the low frequency application investigated in this thesis.

Acknowledgements

First of all, I would like to thank my supervisor Professor Mats Alaküla for initiating this project. I am also most thankful for his support and never-ending enthusiasm during the work.

I also wish to express my sincere gratitude to the steering committee consisting of, besides Professor Mats Alaküla, Patricia Jansson, Höganäs AB, Professor Lars Gertmar, ABB and LTH (IEA), Lennart Ängquist, ABB, and Tord Cedell, LTH (MTV). The committee meetings have formed a nice base for interesting discussions and provided the work with many suggestions and new ideas.

Furthermore I would like to thank everyone at IEA for providing a great atmosphere to work in. Especially I am grateful to my roommate Svante Andersson, always available for discussions and most helpful in keeping me cold, and Per Karlsson, constantly prepared with advise in power electronics and everything else regarding life. Special thanks also to Bengt Simonsson and Getachew Darge for always being ready to help with anything practical.

I am most thankful to my family for their love, trust and support. And last but most important, I would like to thank my beloved wife Cecilia for always believing in me.

This work has been financially supported by Elforsk AB, within the Elektra research program, and Höganäs AB. This support is greatly acknowledged.

Håkan Skarrie

Contents

Chapter 1

Introduction

This chapter gives a brief discussion on the use of inductors as line filters in power electronic circuits. The possible use of iron powder material in the inductor cores as an alternative to laminated cores is also discussed.

1.1 Background

In recent years a large increase in the use of electrical loads supplied through power electronics has taken place. Power electronic loads connected to the utility grid cause distorted line currents due to their non-linear characteristics. The distorted currents will, due to internal impedance in the grid, distort the voltage waveform of other loads connected to the same grid. Voltage distortion may cause malfunction or even damage to sensitive grid connected equipment. Furthermore the current distortion may e.g. cause overheating in distribution and transmission equipment.

Most power electronic circuits use line filters in the interface to the grid. One often-used filter configuration consists of an inductor in series with each phase connected to the grid. The switching of a self commutated power electronics converter generates a current spectrum consisting of components at the mains frequency together with harmonics around the switching frequency and multiples of the switching frequency. The switching frequency of the converter may be high, some tens of kHz, which impose the inductor a wide current spectrum. To minimise the power losses in the inductor introduced by the distorted current the design must be made with care and a suitable core material must be chosen.

A line side filter inductor with the core composed of an iron powder composite material is an interesting alternative to the, so far, most often used laminated steel sheet cores.

1.2 Iron powder cores for use in line filter inductors

Insulated iron powder materials, sometimes also called Soft Magnetic Composites (SMC), have been used for several years in cores of inductors and transformers for high frequency applications due to their ability to prevent eddy current loss. However at the mains frequency, 50 Hz, the hysteresis loss is the dominating loss part of these materials. The hysteresis is partly due to stresses introduced in the material at compaction. Therefore in order to reduce hysteresis a stress relieving heat treatment most often follows the compaction, but the heat also degrades the insulation between powder particles and thus increases the presence of eddy currents in the material. Still the total core loss in iron powder materials exceeds the one generated in laminated materials at these low frequencies. Though, development of insulations that withstands heat treatment at higher temperatures together with increased purity of powders points towards a reduction of the losses even at low frequencies (Jansson, 1998).

Höganäs AB, Sweden, manufactures SMC:s aiming for low frequency applications. Figure 1.1 shows a comparison between two Höganäs SMC:s (Höganäs AB, 1997) and two laminated steel sheet materials at three different levels of flux density. The iron powder materials are, Somaloy 500 + 0.5% Kenolube (continuous line) and Somaloy 500 + 0.6% LB1 (broken line). The laminated materials are two materials with different qualities available from Surahammars Bruk AB, Sweden, (Surahammars Bruk AB, 1998), DK70 (dotted line) and the superior quality CK40 (dash-dotted line). Both laminated materials have a lamination thickness of 0.5 mm. The core losses of the iron powder materials are extrapolated at frequencies above 1000 Hz and for the laminated materials at frequencies above 400 Hz. The figure shows that the losses at 50Hz are higher in the SMC:s than in the laminated materials but it also indicates a higher frequency dependence in the laminated materials losses. At an increasing frequency the loss of the laminated materials exceeds the loss of the SMC:s.

In many applications where the utilisation of iron powder can be interesting, e.g. electric motors and transformers, a high permeability material is a goal. In an inductor, on the other hand, air gaps is used in the magnetic

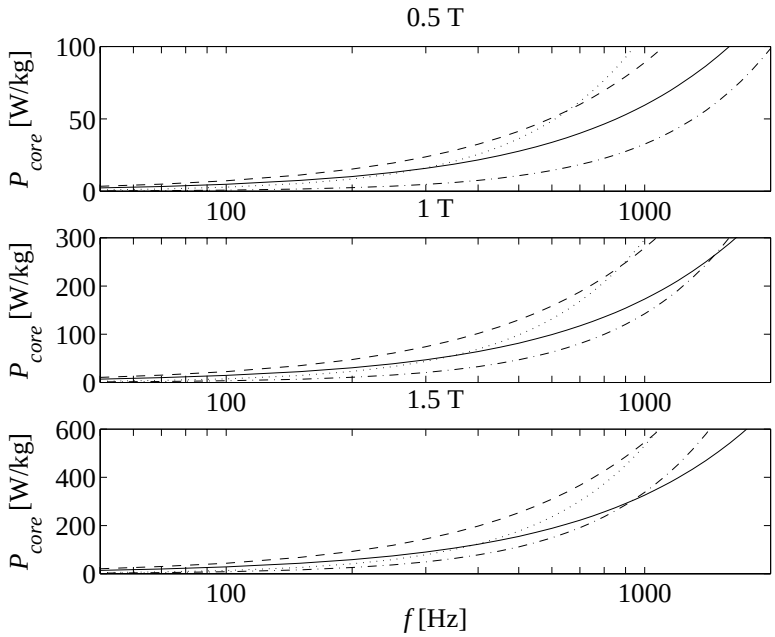

Figure 1.1: Comparison of core losses between iron powder materials and laminated materials at 0.5, 1.0 and 1.5 T. Iron powder materials available from Höganäs AB: Somaloy 500 + 0.5% Kenolube (continuous line) and Somaloy 500 + 0.6% LB1 (broken line). Laminated materials (0.5 mm) available from Surahammars Bruk AB: CK40 (dash-dotted line) and DK70 (dotted line).

path in order to obtain a desired effective permeability and a more linear behaviour of the component. In an iron powder material this air gap is distributed in the material, with a small gap between each particle. An increase in insulating materials in the bulk material increases the distance between particles and thus the total air gap. Hence, the effective permeability of a core can be achieved by including a suitable amount of insulatives. In Figure 1.2 the permeability curves of the iron powder materials Somaloy 500 + 0.5% Kenolube (continuous line) and Somaloy 500 + 0.6% LB1 (broken line) are plotted. The LB1-material has a higher degree of insulating material, which reduces the permeability. In the figure also the permeability of the laminated material CK40 (dash-dotted line) is plotted.

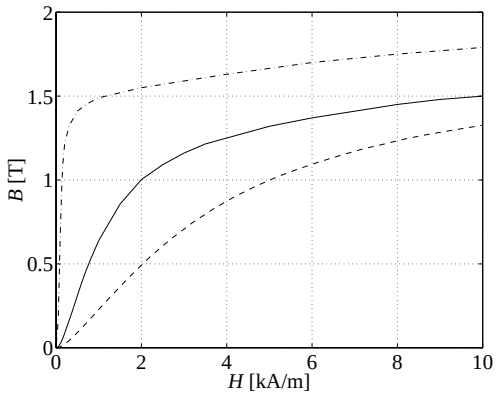

Figure 1.2: Comparison of permeability curves between iron powder materials and a laminated material. Iron powder materials: Somaloy 500 + 0.5% Kenolube (continuous line) and Somaloy 500 + 0.6% LB1 (broken line). Laminated material (0.5 mm): CK40 (dash-dotted line).

By varying the composition of an iron powder composite material, e.g. particle size and the amount of insulation, and controling the fabrication process, e.g. the compaction pressure and heat treatment, a material with suitable properties can be achieved. Besides this possibility of tailoring material properties another advantage of these materials are its isotropic behaviour. The thermal isotropy makes the thermal conductivity the same in all directions while the magnetic isotropy makes three-dimensional flux paths possible. A laminated material suffers from high anisotropy that makes only two-dimensional flux paths possible and also gives a big difference in thermal conductivity in a direction parallel to the laminations and a direction perpendicular to the lamination.

The pressing process also makes it possible to fabricate components with a complex geometry not possible by stacked laminations. The two steps of stamping and stacking in the manufacturing of laminated cores are replaced by a single step of pressing in a powder core. Considering environmental aspects the material waste can be made a minimum at fabrication and the brittleness of the material simplifies separation of the powder from the winding when recycling.

1.3 Main contributions

The main contributions of this thesis can be referred to the following:

- The inductor design program, a system where the losses, thermal heating etc. is carefully calculated for optimisation of an inductor design.
- Evaluation of the use of iron powder composites in inductor cores for low frequency applications.
- A resonant measurement system for fast determination of the inductance and loss of an inductor, and their variation with frequency and current.

1.4 Thesis outline

Chapter 2 deals with the magnetisation process and the properties of different magnetic materials for use in inductor cores. In Chapter 3 core losses in magnetic materials are treated, while the winding losses is discussed in Chapter 4. The losses produced in a component give rise to thermal heating, which is the subject of Chapter 5. In Chapter 6 the developed inductor design program and its field of application is treated. The resonant measurement system for determining the inductor parameters, inductance and resistances, is presented in Chapter 7. Furthermore the inductor design program is used to design the filter inductors of a battery charger for electrical vehicles, Chapter 8 is devoted to this application. As a comparison approximate calculations on an inductor using a laminated core are also performed. In Chapter 9 measurements on the designed and manufactured inductors are carried out by the measurement system. Finally Chapter 10 concludes the thesis.

Chapter 2

Magnetic materials

Magnetic materials are divided into different groups depending on their magnetic behaviour. There are three main groups, diamagnetic, paramagnetic and ferromagnetic materials. Diamagnetic materials, e.g. copper, have susceptibility of about -10^{-5}, i.e. their magnetic response opposes an applied magnetic field. Paramagnetic materials, e.g. aluminium, have small and positive susceptibility, typically 10^{-5} to 10^{-3}, and produce a small magnetisation in alignment with an applied magnetic field. The last main group, ferromagnetic materials have susceptibility well above 1, typically 50 to 10 000. Iron, nickel and cobalt are examples of ferromagnetic materials. There are some other groups besides the main groups with a magnetic behaviour closely related to ferromagnetism. Ferrimagnetic materials are such a group with typical susceptibility of 10 to 10 000.

The discussion in this thesis is concentrated to ferromagnetic materials and specifically iron and silicon-iron alloys.

2.1 Magnetisation

The magnetisation of a ferromagnetic material is a complex process treated by many authors, e.g. (Bozorth, 1978), (Chikazumi, 1997) and (Jiles, 1998). The short explanation here begins on the atomic level of the material.

Material structure

In an atom each electron spins around its own axis, this spin of the electrostatic charged electron makes the electron exhibit a magnetic moment. Some of the

electrons spin in a positive direction and some in a negative, in atoms with an even number of electrons the magnetic moments cancel and the net magnetic moment of the atom is zero. When the number of electrons are odd there will be one uncompensated spin, in most cases this spin originates from a valence electron and is then compensated by the spin of other valence electrons. However, the ferromagnetic materials have a higher number of uncompensated spins due to a not completely filled inner shell. These atoms expose a net magnetic moment and each atom acts as a magnetic dipole.

When an external field is applied to a ferromagnetic material the dipole of an atom interacts with dipoles of neighbouring atoms and the dipoles line up in the direction of the applied field. This interactive behaviour provides an amplification of the applied field and results in high magnetisation even for small values of the applied field.

Even without any external field applied dipoles interacts with its neighbours and shows parallel alignment, a region with all dipoles aligned is called a magnetic domain. In a domain the atoms are regularly ordered in a crystal structure. In iron, for example, the atoms are ordered in a so-called body-centred cubic (BCC) crystal structure. The BCC structure means that the iron crystal is cubic with one atom in each corner and one in the centre of the cube, see Figure 2.1.

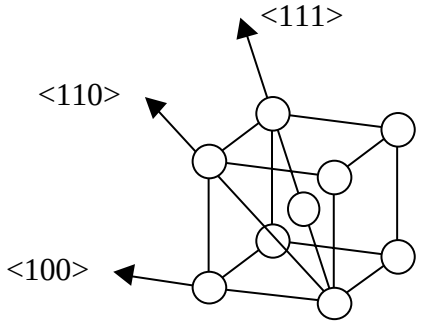

Figure 2.1: Iron crystal with BCC-structure and magnetisation directions, easy <100>, medium <110> and hard <111>.

Within the crystal the directions of magnetisation are restricted to three groups of possible directions, defined by the crystal structure. In an iron crystal the possible groups of magnetisation directions are, along an edge <100>,

diagonal on a side <110> or diagonal in the cube <111>. In iron the <100>-group is the directions of minimum energy or the directions of easy magnetisation, i.e. with no external field applied all domains will be in the <100>-directions. There are six possible directions in the <100>-group, in a demagnetised material the domains are randomly distributed between these directions and the bulk material expose no net magnetisation.

The domains are separated by regions where the dipoles gradually and continuously change direction between the directions of dipoles in surrounding domains. These boundary regions are called domain walls or Bloch walls, the directions of dipoles in a 180° domain wall is seen in Figure 2.2.

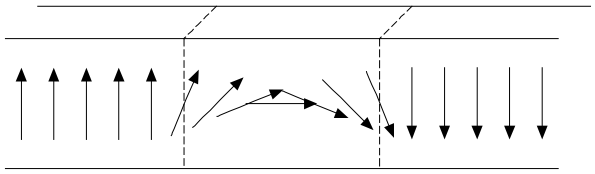

Figure 2.2: Continuously change of dipole alignment in a 180° domain wall.

Magnetisation

Magnetisation of a ferromagnetic material from demagnetised state to saturation magnetisation includes some different types of magnetisation processes, domain wall motion, reversible and irreversible and domain rotation, reversible and irreversible. However, irreversible domain rotation may occur only in a rotating field. At domain wall motion the volume of a domain changes while at domain rotation the magnetisation direction of a domain with fixed volume changes.

When an external field is applied domains with easy magnetisation directions in a direction favourably to the applied field are growing at the expense of domains with unfavourably easy magnetisation directions. Growing of a domain implies that the domain incorporate dipoles of adjacent domains and the magnetisation direction of the incorporated dipoles are changed to the direction of the growing domain. The growing of favourable domains occurs to minimise the energy stored in the structure. In this reshaping of domains the domain walls moves towards the domains with a direction that opposes the

field, the process is called domain wall motion and consist of a reversible and an irreversible part. In a material there are grain boundaries and imperfections such as voids, stressed regions, etc that acts as pinning sites and hinders the domain wall motion. When the applied field is small a wall is hindered to move by the pinning sites, instead the wall starts to bow around the pinning sites. If the field is removed the bowing terminates and the domain wall returns to the original location. This motion is reversible and gives only small increases in the magnetisation because only the dipoles in the bowing area change direction. When the applied field is further increased the wall releases from the pinning site and jumps to a new site. This domain wall motion is irreversible and the magnetisation rises steeply, all dipoles in the area between the old and the new site changes direction. These jumps between pinning sites are called Barkhausen jumps and causes small steps in the magnetisation.

A sufficiently high increase of the applied field makes all domain walls to vanish, due to the irreversible domain wall motion, and the magnetisation is in the easy magnetising direction closest to the direction of the applied field. Further increase of the field cause reversible domain rotation, i.e. the magnetisation vector rotates until fully aligned with the applied field. The increase in magnetisation due to this process is small and the magnetisation starts to saturate. When all domains are aligned with the applied field the material is fully saturated and no further increase in the magnetisation is possible.

In Figure 2.3 a simplified representation of the magnetising processes are shown. The initial magnetising curve, from a demagnetised state to saturation, and the parts associated with the different processes are also shown. The circles represents pinning sites, like impurities or imperfections in the crystal structure.

Figure 2.3 a. shows a region of four domains when no external field is applied, the domains are randomly distributed in the easy magnetising directions and no net magnetisation is present. When the field is increased domains in a favourable easy direction starts to grow. The growing of domains starts with a bowing of domain walls around pinning sites, 2.3 b. Bowing of domain walls are a reversible process and gives only a small rise in magnetisation, range I in 2.3 g. A further increase in the field makes domain walls release from a pinning site and jump to a new site, 2.3 c and d shows this. This process is irreversible and causes a steep rise in magnetisation, range II in 2.3 g correspond to that.

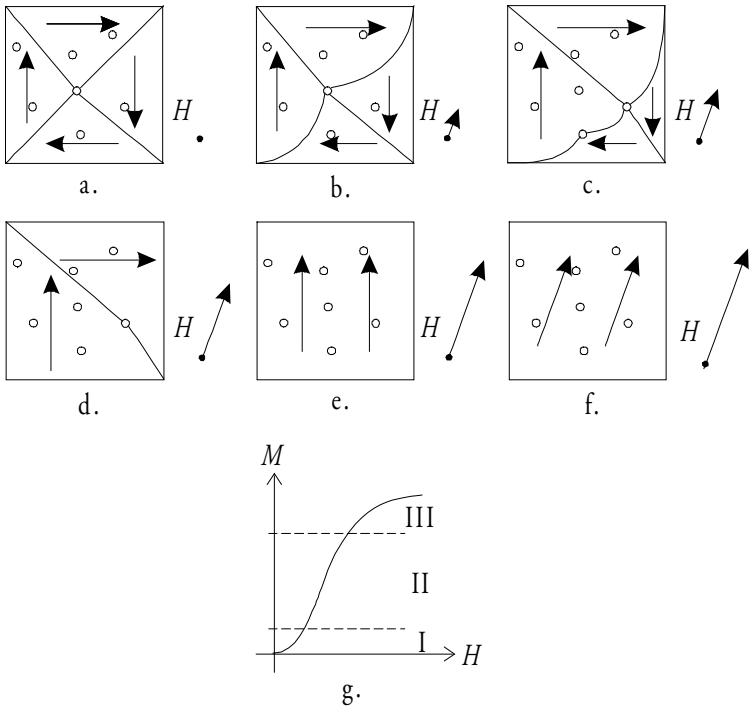

Figure 2.3: A simplified representation of the magnetising processes and the corresponding initial magnetising curve.

Finally at sufficiently high field reversible domain rotation occurs, 2.3 f, domains rotate until fully aligned with the field and causes a small increase in magnetisation, range III in 2.3 g, the magnetisation starts to saturate.

Hysteresis

When a material is magnetised into saturation and the applied field then is removed the decreasing magnetisation do not follow the initial magnetising curve. Domains remain in the easy directions near the direction of the applied field and cause a net magnetisation, corresponding to the remanence B_r (Figure 2.5), at no applied field. A coercive field applied in the opposite direction is required to force the domains into random orientation and cancel the net magnetisation, the magnetisation is zero at coercivity H_c (Figure 2.5). With an

alternating field applied, the magnetisation versus the applied field traces out a loop due to the irreversible magnetisation process. The phenomenon is called magnetic hysteresis and the loop is called a hysteresis loop.

The hysteresis of a soft ferromagnetic material like iron depends on the irreversible magnetisation process and is principally determined by pinning of domain wall motion (Jiles, 1998). The pinning sites that hinders domain wall motion originates from imperfections in the material due to for example dislocations, impurity elements and stressed regions, also grain boundaries contributes to the pinning sites.

The hysteresis of a soft ferromagnetic material is highly connected to the coercivity. A low applied alternating field is for the most part subjected to reversible domain rotation, the coercivity is small and so is the hysteresis. When the field increases into the region dominated by irreversible domain rotation the coercivity increases rapidly. Finally when the magnetisation approaches saturation and the domain rotation is dominating the coercivity reaches a stable value. The conclusion is, a purer material with reduced internal stresses decreases coercivity and gives a smaller hysteresis loop.

Figure 2.4 shows the coercive force with respect to the peak value of the applied magnetic field. A periodic magnetic field with very low frequency, to make eddy currents neglectable, are applied to a ring-shaped sample of iron powder at a number of different amplitudes. A pick-up coil measure the flux density induced in the core, the flux density lags the magnetic field and a hysteresis loop are traced out. In Figure 2.4 a, the hysteresis loop of one measurement are shown. The coercive force at the different amplitudes applied are measured and plotted in Figure 2.4 b with respect to the peak value of the field.

At peak values lower than about 5 kA/m the coercive force increases rapidly, which indicates that irreversible domain wall motion dominates in this region. The irreversible part of the domain wall motion is the main contribution to hysteresis. Domain wall motion is a high permeability process, which is seen in Figure 2.4 a as a steep rise up to about 5 kA/m. Between 5 and 8 kA/m the domain wall motion diminishes and above 8 kA/m there is only reversible domain rotation acting. This reversible process does not increase the coercive force, i.e. it makes almost no contribution to the hysteresis. As seen in 2.4 a, the reversible domain rotation is a low permeability process.

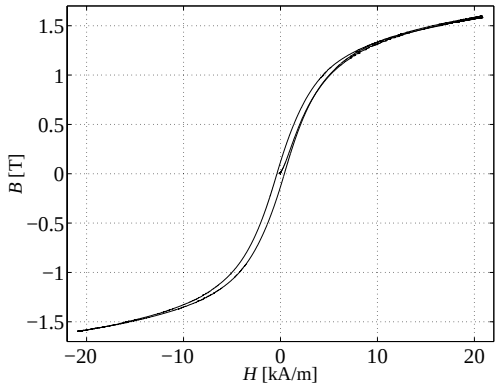

a.

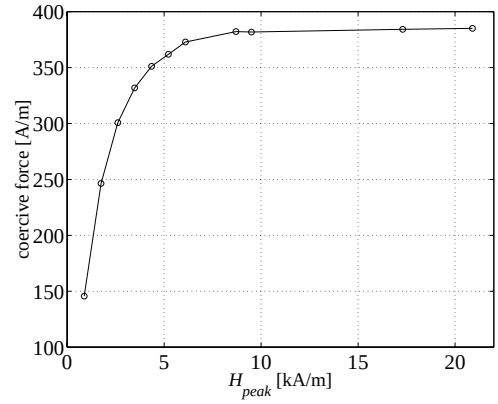

b.

Figure 2.4: a. One measured hysteresis loop. b. Coercive force with respect to the peak value of magnetic field, from measurements of the hysteresis loop.

Permeability

Figure 2.3 shows the initial magnetisation curve of a ferromagnetic material, the slope of the curve determines the permeability of the material. A ferromagnetic material is non-linear, i.e. the permeability is not constant but changes with the magnetic field in the material. Above is the non-linear

behaviour of the permeability explained depending on the different magnetisation processes.

There are various types of permeabilities used to define the magnetic behaviour of a ferromagnetic material. The two permeabilities most commonly used to describe the magnetic properties of a material are initial permeability, μ_i, and maximum permeability, μ_m, see Figure 2.5. For low power applications where the magnetic fields are low the initial permeability is the most important one, while in high power applications the fields are high and the maximum permeability is the most valid.

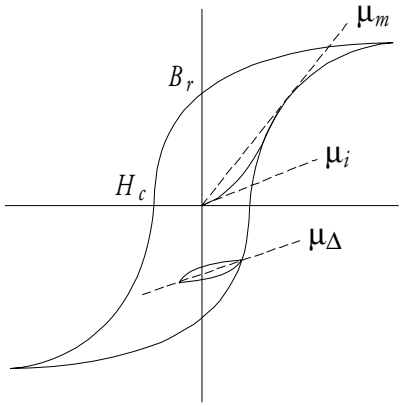

Figure 2.5: Various types of permeabilities, maximum permeability, μ_m, initial permeability, μ_i, and incremental permeability, μ_Δ. The remanence B_r and coercivity H_c are also marked.

In magnetic calculations the definitions amplitude permeability, μ_a, and incremental permeability, μ_Δ, are used. The amplitude permeability is the slope between the tips of a symmetrical loop. At very low applied fields the amplitude permeability coincide with the initial permeability. Increasing the applied field increases the amplitude permeability until the maximum permeability is reached, further increase reduces the permeability. If the loop is non-symmetrical, an ac component is superimposed on a dc component, the slope between the loop tips are the incremental permeability, the slope of the minor loop in Figure 2.5.

The slope at any point on the hysteresis loop or initial curve is referred to as the differential permeability.

The amplitude permeability is the permeability used further in the thesis, and is referred to only as the permeability or sometimes as the relative permeability.

2.2 Materials for inductor cores

The purpose of an magnetic material core in an inductor is to, by a given applied field, produce a higher flux compared to the flux produced in air, and to form a magnetic path for the flux. The type of materials used is ferromagnetic, iron and iron alloys, or ferrimagnetic materials, soft ferrites.

Four important parameters describing the properties of a material from an inductor designer's point of view are relative permeability, μ_r, maximum flux density, B_{max}, coercivity, H_c, and resistivity, ρ. The relative permeability determines a materials capability of conduct magnetic flux. With a high possible maximum flux density the core cross section can be decreased. A small coercivity reduces hysteresis loss and a high resistivity reduces eddy current loss.

Unalloyed commercial iron, containing 0.2% impurities, has a maximum relative permeability μ_{max} = 5 000, B_{max} = 2.15 T, H_c = 80 A/m, and ρ = 0.1 μΩm. High purity iron, containing 0.05% impurities, has μ_{max} = 200 000, B_{max} = 2.15 T, H_c = 4 A/m, and ρ = 0.1 μΩm. The resistivity of iron is very low, i.e. it experience high eddy current losses. To increase resistivity a small amount of silicon often is added to the iron. With 3% of silicon in the iron (non-oriented) the parameters changes to μ_{max} = 6 000, B_{max} = 2.0 T, H_c = 40 A/m, and ρ = 0.5 μΩm, which gives a considerable reduction in eddy current losses. Grain-orientation of the silicon-iron with 3% silicon gives the permeability μ_{max} = 40 000, B_{max} = 2.0 T, H_c = 8 A/m, and ρ = 0.5 μΩm in the oriented direction, but the material will be highly anisotropic. Further increase in permeability and decrease in coercive force can be achieved by nickel-iron alloys, e.g. 78 Permalloy (78% Ni, 22% Fe) has μ_{max} = 100 000 and H_c = 4 A/m, but maximum flux density and resistivity decreases to B_{max} = 1.1 T and ρ = 0.16 μΩm.

Addition of alloys to iron increases resistivity but eddy current losses are still to high, even at 50 Hz. Hence, inductors with laminated cores, with a laminate thickness of about 0.1 – 0.5 mm, are used, this reduces the path of eddy currents and thereby the corresponding losses. In Chapter 3.2 an equation for determining the eddy current losses with respect to lamination

thickness and resistivity is derived. A laminated steel sheet silicon-iron core is suitable for low frequency applications, < 1 kHz. An alternative to the laminated steel sheet core is the tape wound core where a thin tape is wound, most often, into toroids or C-cores. The thickness of the tape can be made thinner than a laminated sheet, down to about 0.003 mm, hence the usable region increases in frequency range.

For medium frequencies, 1 - 100 kHz, iron powder cores are used. An iron powder core consists of small particles, about 100 μm, of pure iron, coated with a thin electrically insulating layer and pressed to a bulk material at high pressure. The insulating coating of every particle gives very small eddy current paths inside a particle and a relatively high resistivity of the bulk material. The small non-magnetic distances between every particle act as air gaps and decreases the permeability of the bulk material. Typical values of an iron powder material with optimum magnetic properties is μ_{max} = 500, B_{max} = 1.9 T, H_c = 250 A/m, and ρ = 10 μΩm. Iron powder cores are more thoroughly treated in Chapter 2.3.

At higher frequencies, > 100 kHz, soft ferrites are particularly good because of their high resistivity. Ferrites denote a group of materials with ferrous oxides combined with one or more metallic ions as for example manganese, zinc and nickel. Ferrites has, as mentioned, high resistivity but they suffer from low maximum flux density. Two common types are manganese zinc ferrite, MnZn-ferrite, and nickel zinc ferrite, NiZn-ferrite. Typical values for MnZn-ferrite are μ_{max} = 4000, B_{max} = 0.4 T, H_c = 8 A/m, and ρ = 1 Ωm and is not suitable for extremely high frequencies. NiZn-ferrite has μ_{max} = 400, B_{max} = 0.25 T, H_c = 80 A/m, and ρ = 10 kΩm and is due to its very high resistivity well suited for very high frequencies.

2.3 Iron powder

Soft Magnetic Composite or dielectromagnetic materials consist of metal particles where every particle is coated with a continuous insulative oxide layer. The particles are compacted, together with an addition of lubricant and possibly a binder, at high pressure into a bulk material. The lubricant eases compaction and the ejection of the components after compaction, while an addition of a binder increases the strength of the material. The lubricant and the binder also provide the insulation between particles. During compaction internal stresses are generated in the material. In order to relieve these stresses a heat treatment process, curing, can be applied. The heat treatment also

increases the strength of the material. If required the ready components may be covered by a protective coating to improve the mechanical strength and provide insulation. Iron powder materials are most often magnetically, thermally and mechanically isotropic in their behaviour.

Making components in iron powder gives a lot of flexibility to the design. The material can be tailored for a specific application by changing the composition of the material and adapt the fabrication process. Due to the magnetic isotropy of most iron powder composites components utilising flux flowing in three dimensions can be considered in contrast to the two-dimensional flux paths available in the highly anisotropic laminated materials. The pressing process also simplifies the possibility to fabricate components with complex geometries.

In the design of inductor cores the effective permeability of the core can be achieved without any large air gap in the magnetic circuit, instead the air gap becomes distributed in the core due to the small gaps between each particle. The small air gap length minimises fringing flux and thereby reduces air gap losses in the core (Chapter 3.5) and in the winding (Chapter 4.4).

Looking at environmental aspects the material waste can be made a minimum because of the pressing. The brittleness of the material simplifies separation of the core from the winding when recycling, the core is pulverised by crushing and than the copper winding easily can be separated from the powder.

Tailoring material properties

Maximised magnetic properties, permeability and maximum flux density, is provided by a maximised iron content, i.e. maximal density of the bulk material. Large particle size, a low content of lubricant and binder and a high compaction pressure gives high density. At low frequencies the hysteresis loss (Chapter 3.1) is the main core loss part and can be reduced by large particle size, higher purity of the iron in the particles and stress relieving heat treatment. An increased particle size gives fewer particle boundaries that hinder magnetisation.

At an increased frequency the eddy current loss (Chapter 3.2) becomes more pronounced and currents circling in the material must be reduced by an increased bulk resistivity. The use of smaller particles and an increased content of insulating materials between particles provide this. The use of iron-alloy particles can increase resistivity even further and a limited heat treatment gives a minimum in deterioration of the insulatives.

Table 2.1 shows the typical changes of some material properties due to variations in composition and the fabrication process. An increase in resistivity reduces the eddy current loss and a decrease in coercivity and/or an increase in permeability reduce hysteresis loss. For a given application a compromise between the adjustable parameters in the table defines the composition and fabrication process that gives the optimum behaviour.

	I	**II**	**III**	**IV**	**V**
permeability	↑	↓	↓	↑	↑
maximum flux density	↑	↓	↓	↑	↑
coercivity	↓	→	→	↑	↓
resistivity	↓	↑	↑	↓	↓
thermal conductivity	↑	↓	↓	↑	↑
strength	↓	↓	↑	↑↓ *	↑ **

I. increasing particle size
II. addition of lubricant
III. addition of binder
IV. increasing compaction pressure
V. heat treatment

* In a material with a binder the strength increases with increasing compaction (Jansson, 2000) while the opposite behaviour occurs in a material without binder (Jansson, 1998).

** In a material including a binder the strength increases up to typically 200°C, (Gélinas et al., 1998) and (Jansson, 2000), due to an improved distribution of the binder, further increase deteriorates the binder and the strength decreases. A material without a binder (including a lubricant) shows a monotonously increase in strength with increasing temperature (Jansson, 1998).

Table 2.1: Parameter dependence on composition and the fabrication process.

The materials used

The two SMC materials used in this thesis are manufactured by Höganäs AB. Both materials are composed by Somaloy 500, a water atomised high purity iron powder with particle size <150 μm and coated by a thin layer of inorganic

insulation. In the first material the powder are mixed with 0.6% lubricating binder, here called Somaloy 500 + 0.6% LB1. The material is compacted at 800 MPa and then heat treated at 275°C for 60 minutes in air. The other material is called Somaloy 500 + 0.5% Kenolube, where Kenolube is a lubricant, the material is compacted at 800 MPa and heat treated at 500°C for 30 minutes in air. The difference in composition and heat treatment makes Somaloy 500 + 0.5% Kenolube a material with optimised magnetic properties and Somaloy 500 + 0.6% LB1 suitable for higher frequencies with a little deteriorated magnetic properties. Some typical properties of the two materials are listed in Appendix B.

How the properties of Somaloy 500 varies with composition and fabrication is investigated in (Jansson, 2000). The impact of different lubricants and the amount of lubricant, compaction pressure and curing temperature are investigated.

In (Jansson, 2000) the materials are also exposed to thermal cycling and the influence on the losses is examined. The samples are exposed to a higher temperature for 2 to 4 weeks, cooling to ambient for one day and then heated again for another 2 to 4 weeks. After 18 weeks three samples, heated to 100°C, 150°C respectively 200°C was compared with a reference sample. The samples of Somaloy 500 + 0.5% Kenolube showed no significant increase in loss for temperatures up to 150°C, while samples of Somaloy 500 + 0.6% LB1 showed no significant increase even for the highest temperature, 200°C.

The effects of thermal cycling is also studied in (Pelletier et al., 1998). A thermal cycle where the temperature is -40°C for two hours and then 150°C for two hours is used. Measurements on an iron powder material with 0.8% of a phenolic resin showed no significant change in core loss.

The frequency dependence of the initial permeability for Somaloy 500 + 0.5% Kenolube and Somaloy 500 + 0.6% LB1 is seen in Figure 2.6. At a sufficiently high frequency of the external field applied to a sample eddy currents induced in the material generates a field opposing the applied field and an increased field is needed for generating a given flux density (Chapter 3.2), i.e. the permeability decreases. Hence, the composition and fabrication determines the upper frequency limit, the bandwidth, of the material. The higher degree of insulating materials in Somaloy 500 + 0.6% LB1 makes it suitable for higher frequencies (f < 100 kHz) than Somaloy 500 + 0.5% Kenolube (f < 10 kHz).

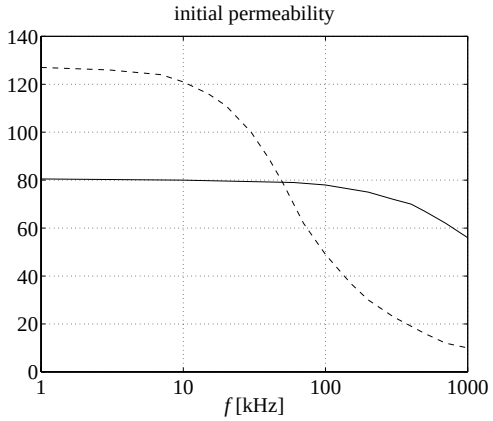

Figure 2.6: The frequency dependence of the initial permeability for Somaloy 500 + 0.6% LB1, continuous line, and Somaloy 500 + 0.5% Kenolube, broken line.

Chapter 3

Core losses

When an inductor core is exposed to a varying magnetic field, losses originate in the core material. These losses can be divided into three types depending on the physical background of the loss. The types are hysteresis, eddy current and anomalous loss. Hysteresis loss is a static loss that is due to the hysteresis of the material. The other two are dynamic losses, both depending on eddy currents in the material, but in different scales. The macroscopic eddy current loss, sometimes referred to as the classical eddy current loss, origins from currents in the material set up by an applied varying magnetic field, while the microscopic eddy current loss, often called anomalous loss, is due to eddy currents generated by domain wall motion.

3.1 Hysteresis loss

The static loss or hysteresis loss originates from the hysteresis phenomenon, treated in Chapter 2.1. At magnetisation the domain walls in the material moves, but the motion is hindered by internal stress, impurities etc. An applied magnetising force must therefore exceed the force pinning the domain walls. That means, when a ferromagnetic material is magnetised most of the applied energy is stored in the material but some energy is converted to heat while moving the reluctant domain walls. Subjected to a cyclic magnetisation the $B(H)$ characteristic describes a loop, as in Figure 3.1. The power dissipated per unit volume due to the hysteresis, at an applied magnetic field H with the frequency f, is

$$p_h = f \int H dB = f A_{hyst} \tag{3.1}$$

where the integral corresponds to the area enclosed by the hysteresis loop in one cycle, A_{hyst}. The energy loss due to hysteresis is independent of the rate of change of the flux density, i.e. it is a static loss.

A good model of the hysteresis loop makes determination of the hysteresis loss possible. A hysteresis loop model must be able to model not only major loops, symmetric - without bias, and asymmetric - with bias, but also minor loops that arises when an applied field contain local minima and maxima, see Figure 3.1. The previous magnetisation of a material depends to a great extent on the magnetic history, which the model also has to consider.

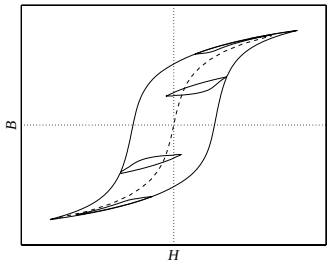

Figure 3.1: A major hysteresis loop with minor loops and the anhysteretic curve (broken line).

There are many different models described in the literature. The two most common in use are the Jiles-Atherton model and the Preisach model. The Jiles-Atherton model is a physical model of hysteresis while the Preisach model is a more mathematical model. The model used in this thesis is the Preisach model, which will be explained in detail, but first a short description of the Jiles-Atherton model and some comments on advantages and disadvantages.

The Jiles-Atherton model

The Jiles-Atherton model (Jiles, Atherton, 1986) is a physically based model that includes the different mechanisms that take place at magnetisation of a ferromagnetic material. The model is composed of an equation describing the anhysteretic curve, to which expressions taking care of the hysteresis are added. The anhystertic curve is the trajectory the magnetisation follows when hysteresis is disregarded, broken line in Figure 3.1. This means that each point on the anhysteretic curve correspond to a domain configuration that gives a

global energy minimum for a given applied field, however points on the hysteresis curve only correspond to local energy minima. To determine the anhysteretic curve a slowly decreasing ac magnetic field with low frequency superimposed on a dc field is applied, when the ac field has decayed to zero the anhysteretic value corresponding to the applied dc field is found.

Before using the J-A model five parameters must be determined. The first parameter, α, is a mean field parameter defining the magnetic coupling between domains in the material, and is required to calculate the effective magnetic field, H_e, composed by the applied external field and the internal magnetisation. The model also need an equation describing the anhysteretic curve, $M_{an}=M_s f(H_e)$, (Jiles, Atherton, 1983) suggests the use of a Langevin function. Two parameters are to be specified and included in the function, the saturation value of magnetisation, M_s, and a Langevin parameter, a. Hysteresis is added by including pinning of domain walls, this is done by a parameter, k, defining the pinning site density, in J-A the pinning of domain wall motion is assumed to be the major contribution to hysteresis. At this stage only irreversible magnetisation is considered, the last parameter, c, defines the amount of reversible magnetisation, due to wall bowing and reversal rotation, included in the magnetisation process.

Finally the J-A model ends up in following differential equations

$$\frac{dM_{irr}}{dH} = \frac{M_{an} - M_{irr}}{\delta k - \alpha\left(M_{an} - M_{irr}\right)} \tag{3.2}$$

$$\frac{dM_{rev}}{dH} = c\left(\frac{dM_{an}}{dH} - \frac{dM_{irr}}{dH}\right) \tag{3.3}$$

$$\frac{dM}{dH} = \frac{dM_{irr}}{dH} + \frac{dM_{rev}}{dH} \tag{3.4}$$

where M_{irr} and M_{rev} is the irreversible respectively the reversible part of the magnetisation. The Langevin function for the anhysteretic curve is

$$M_{an} = M_s\left[\coth\left(\frac{H_e}{a}\right) - \left(\frac{a}{H_e}\right)\right] \tag{3.5}$$

and the effective field H_e is composed by the external field and the internal magnetisation

$$H_e = H + \alpha M \tag{3.6}$$

The parameter δ in (3.2) is a directional parameter equal to +1 for increasing H and –1 for decreasing H.

The major advantages of the J-A model is that it is based on physical properties describing the magnetisation process, and the limited number of parameters (α, M_s, a, k and c) required.

One big disadvantage is the difficulty of identifying the parameters. (Jiles et al., 1992) suggests how to extract the parameters from experimental data, still some subsequent refinement of the parameters is necessary to obtain an accurate model.

The Preisach model

The Preisach model is a mathematically based model of hysteresis. The model was first suggested by Preisach in 1935 (Preisach, 1935) but has been subjected to many improvements over the years.

In the Preisach model a magnetic material is assumed to consist of an infinite number of magnetic elemental dipoles with a rectangular hysteresis loop, Figure 3.2.

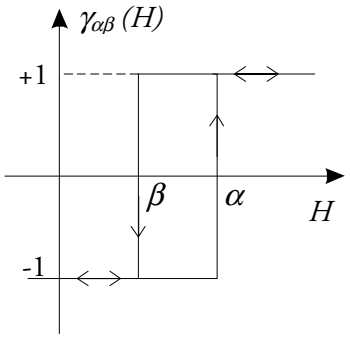

Figure 3.2: Rectangular hysteresis loop of an elemental dipole.

An elemental dipole has two possible states, either in the same direction as an applied field H, $\gamma_{\alpha\beta}$ = +1, or in the opposite direction, $\gamma_{\alpha\beta}$ = -1. The switching of the sign of $\gamma_{\alpha\beta}$ occurs at the threshold value α, for a field in a positive increasing direction and at the threshold value β, for a field in negative

increasing direction. The threshold values α and β is specific for each dipole but $\alpha \geq \beta$ is always true.

An applied magnetic field *H*, will induce a magnetic flux density *B* expressed by

$$B = \int_S \mu(\alpha, \beta)\gamma_{\alpha\beta}(H)d\alpha d\beta \tag{3.7}$$

where *S* is the Preisach plane, the triangular region $H_{sat} \geq \alpha \geq \beta \geq -H_{sat}$, in the Preisach diagram of Figure 3.3.

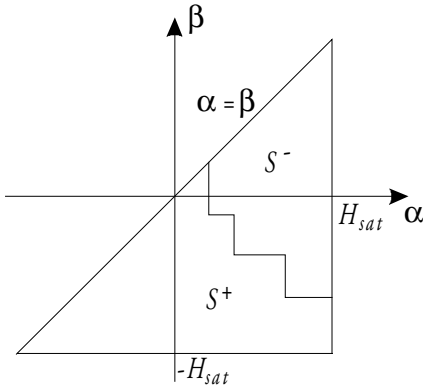

Figure 3.3: Preisach diagram.

Each point, with coordinates (α,β), in the Preisach plane is represented by a density of probability of finding an elemental dipole with threshold values α and β. This distribution function of the dipoles is defined by $\mu(\alpha,\beta)$, which is zero everywhere outside the triangle *S* but has a positive non-zero value inside the triangle. Due to symmetry of major hysteresis loops $\mu(\alpha,\beta) = \mu(-\beta,-\alpha)$ The region S^+ in Figure 3.3 corresponds to dipoles with $\gamma_{\alpha\beta}(H) = +1$ and S^- corresponds to dipoles with $\gamma_{\alpha\beta}(H) = -1$, then (3.7) can be expressed as

$$B = \int_{S+} \mu(\alpha, \beta)d\alpha d\beta - \int_{S-} \mu(\alpha, \beta)d\alpha d\beta \tag{3.8}$$

The magnetic history and the present state of magnetisation determine the interface between the region of positive dipoles, S^+, and negative dipoles, S^-.

So, from the Preisach diagram it is possible to construct the hysteresis loop, including minor loops, of a magnetic material. The way of doing this is described by the help of Figure 3.4. Initially the material is in a demagnetised state, Figure 3.4 a, where $S^+ = S^-$ and (3.8) becomes

$$B = \int_{S+} \mu(\alpha,\beta)d\alpha d\beta - \int_{S-} \mu(\alpha,\beta)d\alpha d\beta = 0 \tag{3.9}$$

Now an increasing positive field is applied over the material, H increases in the positive α-direction, Figure 3.4 b, S^+ grow at the expense of S^- and the flux density increases. With a sufficiently high field applied, positive saturation is attained, 3.4 c, S^+ covers the entire Preisach plane and the maximum flux density is reached, (3.8) becomes

$$B = \int_{S+} \mu(\alpha,\beta)d\alpha d\beta \tag{3.10}$$

From the demagnetised state up to saturation the initial magnetisation curve is traced, when the applied field is decreased to zero and then increased to negative saturation a new curve is traced out due to the hysteresis, 3.4 d-g. Now, the region S^- grow in negative β-direction, at negative saturation, 3.4 g, (3.8) obviously becomes

$$B = -\int_{S-} \mu(\alpha,\beta)d\alpha d\beta \tag{3.11}$$

and the minimum flux density is reached.

On the downward path a local minimum/maximum is added on the applied field and as a consequence a minor loop is traced out, 3.4 e-f. The construction of a minor loop follows the same procedure as for the major loop. A field in positive direction increases S^+ in positive α-direction, 3.4 e, and a field in negative direction decreases S^+ in negative β-direction, 3.4 f. When the minor loop is completed and the negatively increasing field sinks below the reversal point at the local minimum the minor loop is wiped out and erased from the history of the magnetisation. The 'wiping-out' property implies that when a minor loop is completed the magnetisation depends only on the past major minimum/maximum and not on minor loop minima/maxima. This property agrees with the natural property of magnetic materials (Mayergoyz, 1986), the shape of a major hysteresis loop is not dependent on minor loops in the magnetic history.

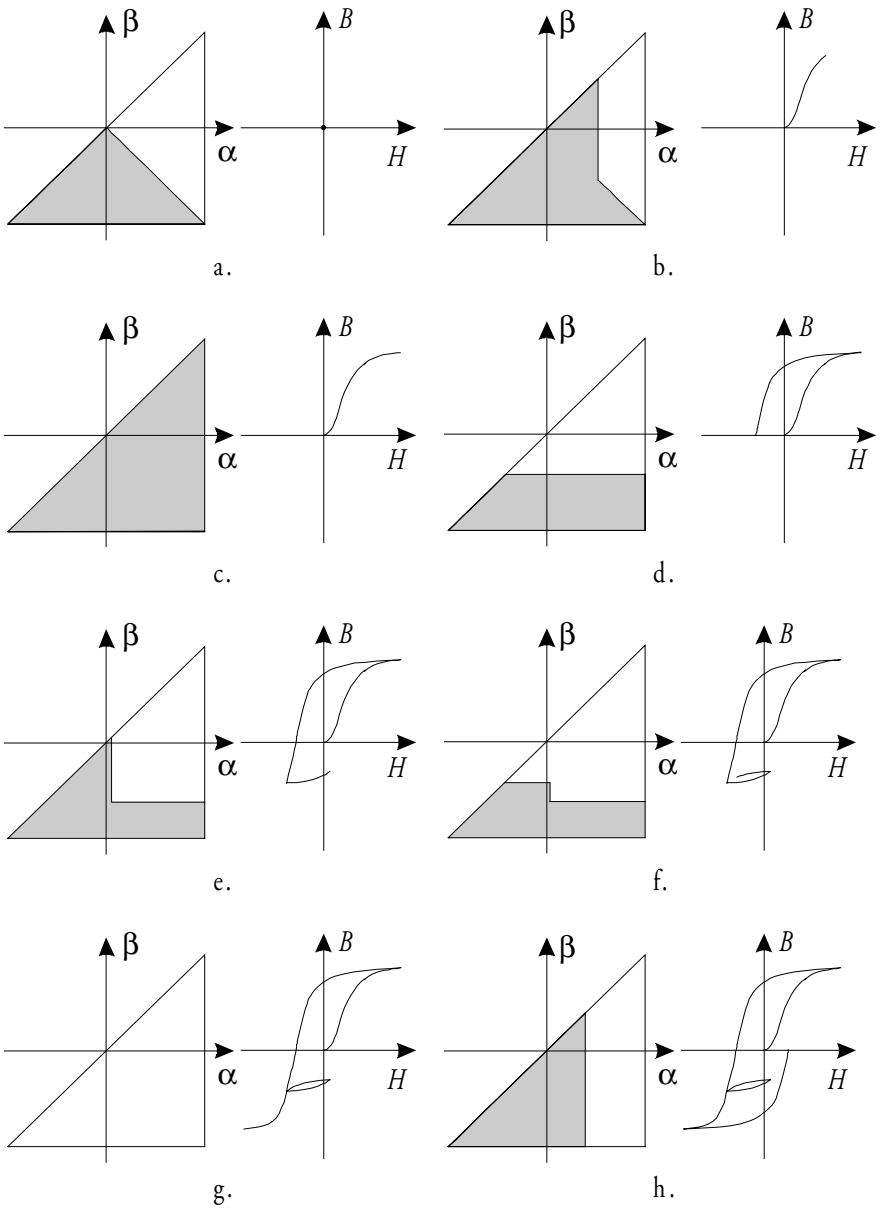

Figure 3.4: Construction of a major loop, including the initial magnetisation and a minor loop, from a Preisach diagram.

Finally, the applied field is decreased from negative saturation to zero and S^+ again grow in positive α-direction, 3.4 h. If the field is increased to positive saturation the major loop is completed and the enclosed area, with a small contribution of the minor loop area, correspond to the hysteresis loss.

A point where the field is changing from increasing to decreasing, or the opposite, is called a reversal point. This term is used in the following discussions.

Numerical implementation

Numerical implementation of the Preisach model encounters some problems (Mayergoyz, 1986). First, the distribution function of the dipoles, $\mu(\alpha,\beta)$, must be determined, this requires a set of first-order transition curves, which is not any standardised data provided by manufacturers nor easily found by simple measurements. Furthermore differentiation of a function calculated from the transition curves is required. A second problem is that computation of the flux density demands for numerical evaluation of double integrals.

A nice way to avoid these problems is suggested in (Zhu, 1994), where the computation of the flux density is graphically related to the Preisach diagram. The flux density for a given applied field is expressed in terms of the flux density of the last reversal point and the area integration of a triangle in the Preisach plane bounded by the magnetic field of the last reversal point and the given applied field. The area integration is related to the limiting loop and the need of the dipole distribution function is avoided. The method is described in Appendix A and also, in more detail, in (Zhu, 1994). Only the resulting expressions for calculation of the flux density are presented here.

The general expression of the flux density after n reversal points, from Appendix A, is

$$B(H) = B(H_n) - 2T(H_n, H) \tag{3.12}$$

on a downward trajectory, and

$$B(H) = B(H_n) + 2T(H, H_n) \tag{3.13}$$

on a upward trajectory. The index n denotes the last reversal point, H_n the magnetic field of the last reversal point and $B(H_n)$ the corresponding flux density. T is the area integration of the triangle and is expressed by

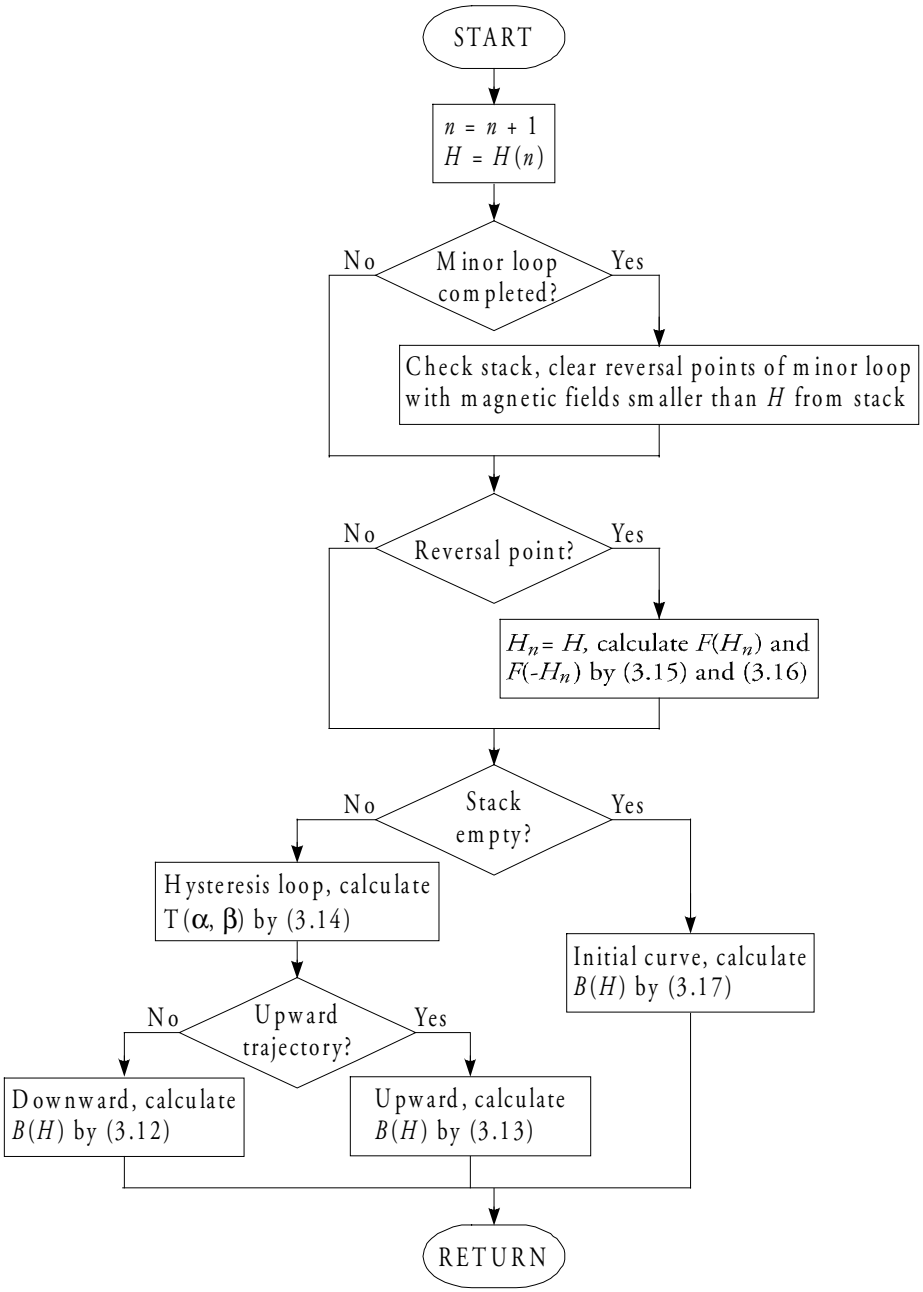

Figure 3.5: Flowchart of the Preisach model.

$$T(\alpha,\beta)=\frac{B_u(\alpha)-B_d(\beta)}{2}+F(\alpha)F(-\beta) \tag{3.14}$$

where $B_u(\alpha)$ and $B_d(\beta)$ is the flux density of the upward trajectory respectively the downward trajectory of the limiting loop. $F(H)$ is a mathematical function described by

$$F(H)=\frac{B_d(H)-B_u(H)}{2\sqrt{B_d(H)}}, \quad H\geq 0 \tag{3.15}$$

$$F(H)=\sqrt{B_d(-H)}, \quad H<0 \tag{3.16}$$

Magnetisation from a demagnetised state follows the initial magnetisation curve, the flux density on the initial curve is calculated by

$$B_i(H)=\left[F(-H)-F(H)\right]^2 \tag{3.17}$$

With these six equations, (3.12) – (3.17), any hysteresis loop, including minor loops, can be modelled. The only input of data needed is the limiting hysteresis loop and, of course, the specified applied magnetic field. This way of describing the Preisach model is fairly easy to implement in software. A flow chart illustrating the different steps needed when implementing the model in software is seen in Figure 3.5.

Implementation in software

The only input data needed in the model is the limiting hysteresis loop, separated in an upward trajectory, $B_u(H)$, respectively a downward trajectory, $B_d(H)$, and a vector with the specified applied magnetic field $H(n)$. To keep track of the magnetic history a stack that contains reversal points is included in the program. When starting on the initial magnetisation curve the stack is initialised empty. If the applied H-field has local extremes a minor loop is traced out between a local minimum and a local maximum and the reversal points of the minor loop, i.e. the local minimum and maximum point, is stored in the stack. When the applied field exceeds the value of the reversal points representing the last minor loop, the reversal points of the minor loop are removed from the stack and the minor loop is wiped out of the magnetic history. This is in accordance with the 'wiping-out' property of the Preisach model.

With the flux density vector $B(n)$ calculated from the vector of the applied magnetic field $H(n)$ the magnetic energy per unit volume stored in the material is determined by

$$w = \int HdB \approx \sum H\Delta B \tag{3.18}$$

To get an accurate result without using too high resolution in the vector of the applied field, which is highly time consuming, the average of a backward and a forward difference of equation (3.18) is used for calculating the vector representing the stored energy

$$w_b(n) = \sum_1^n H(m)\big[B(m) - B(m-1)\big] \tag{3.19}$$

$$w_f(n) = \sum_1^n H(m)\big[B(m+1) - B(m)\big] \tag{3.20}$$

$$w(n) = \frac{w_b(n) + w_f(n)}{2} \tag{3.21}$$

Then the energy loss per unit volume associated with the hysteresis is determined by the difference in stored energy in one period of the time.

Verification

This implementation of the Preisach model, suggested by Zhu, used here gives fairly good results when calculating the flux density $B(H)$ compared to measurements. The plot in Figure 3.6 shows a loop measured on a toroidal ring sample composed of Somaloy 500 + 0.6% LB1, the continuous line, and the corresponding loop modelled by Preisach, the broken line. The modelled loop follows the measured loop well, but there is a small discrepancy in flux density for $B > 0$ on the downward trajectory and for $B < 0$ on the upward trajectory.

The main reason of using the Preisach model in this thesis is for estimation of the hysteresis loss, i.e. the area enclosed by the loop. When this implementation of the Preisach model is used for hysteresis loss estimation the small discrepancy in flux density gives a considerable error. Figure 3.7 shows the hysteresis loss calculated by Preisach, the continuous line, compared to measurements, circles. Also the error related to this hysteresis loss prediction is

seen in the figure. The error in this estimation is up to about 30 % in the range of 0.4 – 0.6 T, which is a considerable error.

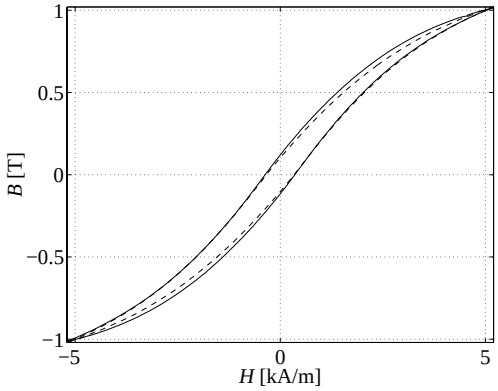

Figure 3.6: Measured loop – continuous line, loop modelled by Preisach – broken line.

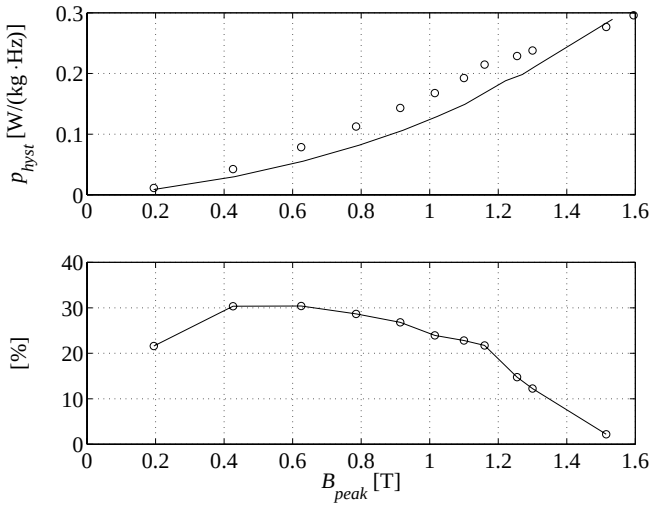

Figure 3.7: Hysteresis loss estimation, measurements – circles, calculated by Preisach – continuous line (top) and error between measurement and calculation (bottom).

In order to reduce the discrepancy in flux density and hence improve the hysteresis loss estimation an extension to the originally used Preisach is suggested.

An extended Preisach model

Initially the nature of the discrepancy will be investigated. Figure 3.8 shows the difference in flux density between a loop measured on the toroidal ring of Somaloy 500 + 0.6% LB1 and the corresponding loop modelled by Preisach. The difference $B_{diff} = B_{meas} - B_{preis}$, on a downward trajectory, i.e. from $+B_{max}$ down to $-B_{max}$, is plotted for a number of loops with different maximum flux densities. Due to the symmetry of the loop an upward trajectory, i.e. from $-B_{max}$ up to $+B_{max}$, will show a similar result. It is obvious from the plots that the discrepancy occurs mainly in the interval $0 < B < B_{max}$, with a maximum at approximately $B_{max}/2$ for the downward trajectory. In the same way the interval of the main discrepancy for an upward trajectory is $-B_{max} < B < 0$ with a maximum at $B_{max}/2$.

In order to reduce the discrepancy the flux density of the extended model, B_{ext}, is calculated by adding a new function, $dB(B)$, to the flux density calculated by the originally used Preisach, B.

$$B_{ext} = dB(B) + B \tag{3.22}$$

For a symmetrical major loop the function is added in the interval $0 < B < B_{max}$ on a downward trajectory and in $-B_{max} < B < 0$ on an upward trajectory, where B_{max} is the maximum flux density of the loop, everywhere else $dB = 0$. A squared function which is zero for $B = 0$ and $B = B_{max}$ and hence has its maximum for $B = B_{max}/2$ is suggested for dB

$$dB(B) = k\left[B_m - \frac{1}{B_m}(B - B_m)^2\right] = kB\left[2 - \frac{B}{B_m}\right] \tag{3.23}$$

where $B_m = B_{max}/2$ and k is a material dependent parameter that settles the magnitude of dB. Next step is to investigate the behaviour of the parameter k.

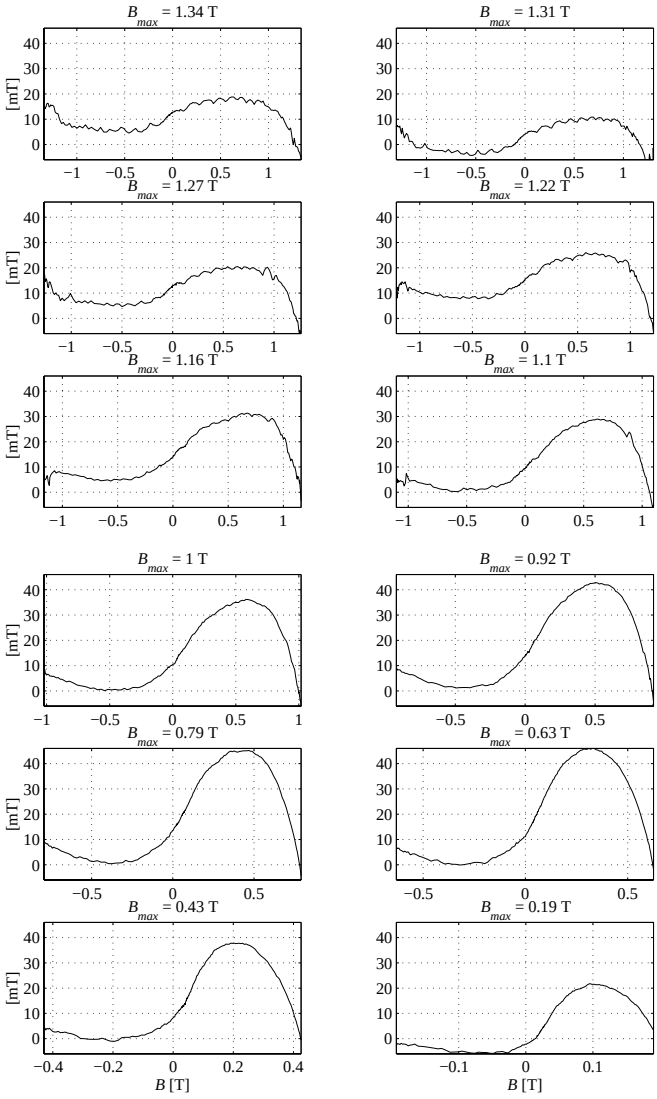

Figure 3.8: Difference in flux density on a downward trajectory between a measured hysteresis loop and a loop modelled by Preisach, B_{diff} = B_{meas} - B_{preis}, at a number of different maximum flux densities.

Parameter determination of the extended model

The suggested function, $dB(B)$ in (3.23) has, as stated, its maximum at $B_m = B_{max}/2$, i.e.

$$dB_{max} = dB(B_m) = kB_m \tag{3.24}$$

hence

$$k = dB_{max} / B_m$$

In the same way with the maximum values of $B_{diff} = B_{meas} - B_{preis}$ in Figure 3.8, denoted $B_{diff_{max}}$

$$k' = B_{diff_{max}} / B_m$$

The parameter k should have the same behaviour as k', the behaviour of k' is examined by plotting k' as a function of B_{max} in Figure 3.9. The plot shows an almost linearly decrease in k' as B_{max} approaches the maximum flux density of the limiting loop, thereby the following expression for k is suggested

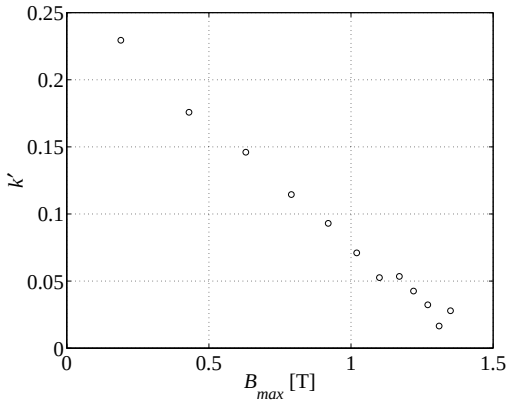

Figure 3.9: $k' = B_{diff_{max}}/B_m$, where $B_{diff_{max}} = \max(B_{meas} - B_{preis})$ from Figure 3.8 and $B_m = B_{max}/2$.

$$k = k_0\left(1 - \left|\frac{B_{max}}{B_{lim_{max}}}\right|^n\right) \tag{3.25}$$

where k_0 and n are material dependent parameters and $B_{lim_{max}}$ is the maximum flux density of the limiting loop.

Finally, k_0 and n will be determined, this is done by inserting k from (3.25) in (3.24) and fit dB_{max} to the maximum values of the discrepancy, $B_{diff_{max}}$, from Figure 3.8. The best fit gives the necessary parameters k_0 and n.

To summarise the use of the suggested extension to the Preisach model the new flux density is calculated by (3.22) with

$$dB(B) = kB\left[2 - \frac{B}{B_m}\right], \quad 0 < B < B_{max} \text{ on a downward trajectory}$$

$$dB(B) = kB\left[2 - \frac{B}{B_m}\right], \quad -B_{max} < B < 0 \text{ on an upward trajectory}$$

$$dB(B) = 0, \quad \text{everywhere else}$$

and k calculated by (3.25).

Verification of the extended Preisach model

The extended model is verified by comparing hysteresis loss modelling to measurements of an iron powder material, Somaloy 500 + 0.6% LB1. Measurements on this material is already used in earlier plots, Figure 3.6 – 3.9.

At first the parameters k_0 and n of the material will be determined. The maximum value of the discrepancies in the flux density, B_{diff}, from Figure 3.8 is plotted as circles in Figure 3.10 (top). dB_{max} from (3.24) is fitted to these values by adjusting k_0 and n. The best fit gives parameters k_0 = 0.27 and n = 1.3, the continuous line in 3.10 (top). Figure 3.10 (bottom) shows the agreement between k', circles, and k, continuous line.

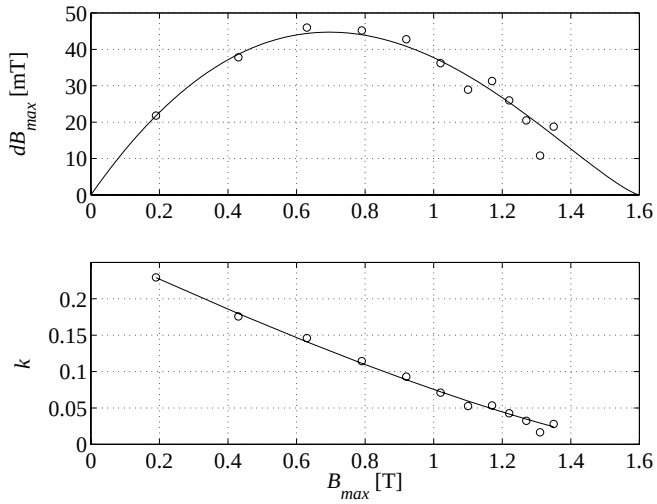

Figure 3.10: dB_{max}, continuous line, fitted to $B_{diff_{max}}$, circles, (top) and k, continuous line, compared to $k' = B_{diff_{max}}/B_m$, circles, (bottom) with $k_0 = 0.27$ and $n = 1.3$.

In Figure 3.11 $B_{diff}(B)$ from Figure 3.8 is plotted again, as a continuous line, this time the adapted function $dB(B)$ is also plotted, as a broken line. The function shows good correspondence with the discrepancy in flux density between measurements and modelling by the originally used Preisach.

For the final verification a hysteresis loop is calculated and the hysteresis loss is predicted by the extended Preisach model and compared to a measured loop respectively measurements of the loss. Figure 3.12 shows the comparison between a measured loop and the corresponding loop calculated by the extended Preisach model. The same comparison was made in Figure 3.6, but for the loop calculated by the original Preisach model. A great improvement when using the extended model is evident, in Figure 3.12 the calculated loop is almost fully concealed by the measured loop.

This evident improvement in flux density estimation should also improve the hysteresis loss prediction. The hysteresis loss calculated by the originally used Preisach model was shown in Figure 3.7, with a maximal error of about 30%.

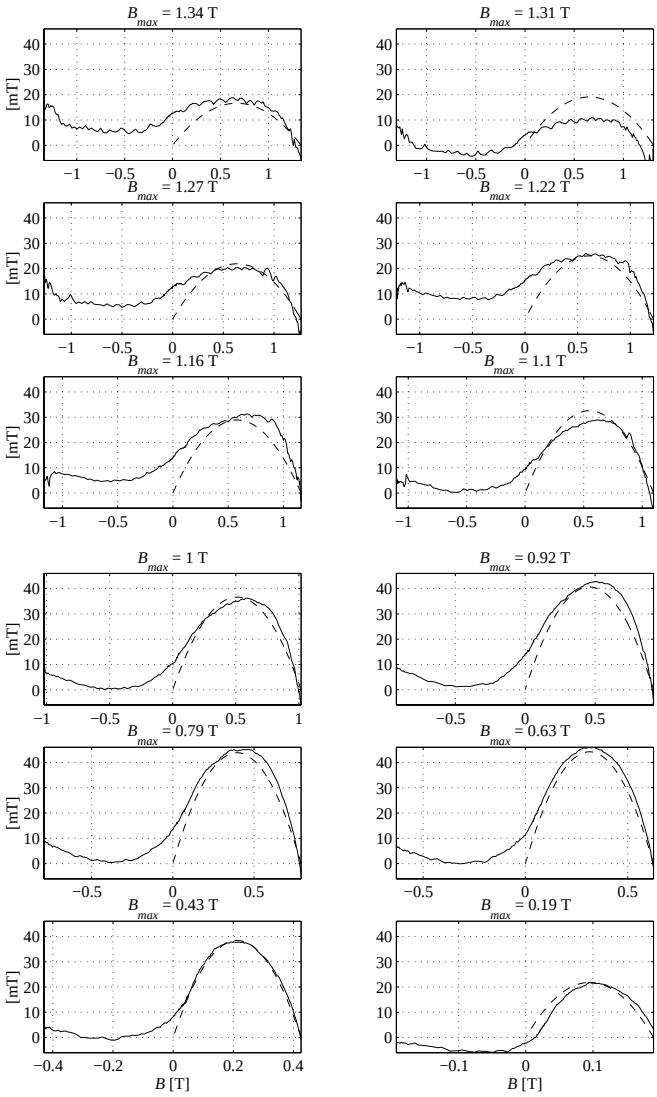

Figure 3.11: $B_{diff}(B)$, continuous line, and the adapted function $dB(B)$ of the extended Preisach model, broken line.

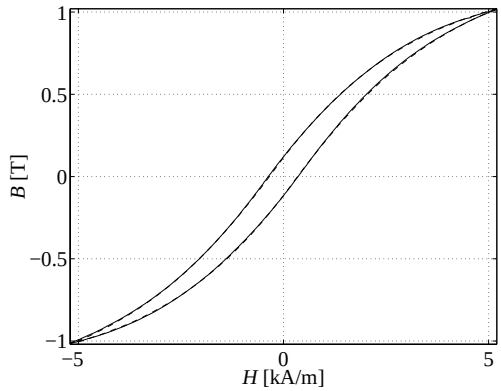

Figure 3.12: Measured loop – continuous line, loop modelled by extended Preisach – broken line (which is almost covered by the measured loop)

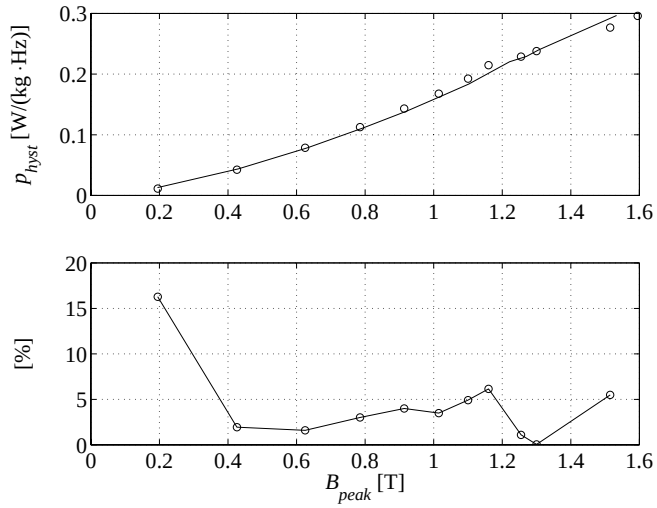

Figure 3.13: Hysteresis loss, measurements – circles, calculated by the extended Preisach – continuous line (top) and error between measurements and calculations (bottom).

In Figure 3.13 the extended Preisach model is used for estimating the hysteresis loss. The maximal error in this case is 16%, obtained at 0.2 T, if this point is disregarded the maximum error is about 6% at about 1.2 T. A plot of the two loops at B = 0.2 T shows good agreement in the region where $dB > 0$. The discrepancy occurs for $-B_{max} < B < 0$ on a downward trajectory and for $0 < B < -B_{max}$ on an upward trajectory, i.e. in the region not affected by dB. In inductors for use in the low frequency applications this thesis aiming for, high flux density mostly are favourable, i.e. the point at 0.2 T can be disregarded in this case. Even if not this low flux density point is disregarded the improvement compared to the originally used Preisach model is significant.

Hysteresis loss at sinusoidal flux density

In a material exposed to a periodic flux without any local extremes and without any dc bias, e.g. pure sinusoidal flux, it is not necessary to determine the loop area each time the hysteresis loss will be calculated. In this special case equation (3.1) for the hysteresis loss per unit volume can be written as

$$p_h = f\int HdB = k_h f\hat{B}^n \tag{3.26}$$

where k_h is a constant and the exponent n range between 1.5 and 2.5 depending on the material. The parameters k_h and n are specific for each material and can be determined by e.g. the Preisach model. By adapting (3.26) to the estimation of hysteresis loss, made at some different amplitudes of the applied field, by e.g. the extended Preisach model, the parameters k_h and n can be determined. This is made for the used iron powder materials Somaloy 500 + 0.6% LB1 and Somaloy 500 + 0.5% Kenolube with the resulting parameters tabulated in Table 3.1.

Material	k_h	n
Somaloy 500 + 0.6% LB1	1160	1.6
Somaloy 500 + 0.5% Kenolube	880	1.7

Table 3.1: Hysteresis loss parameters for use in (3.22).

The approximate expression of the hysteresis loss in (3.26) is valid for symmetrical major loops at flux densities up to about three-quarters of the

saturation flux density. When the flux density approaches saturation the reversible domain rotation starts to get evident, which due to its reversibility not contributes to the hysteresis loss, i.e. the hysteresis loop starts to increase more slowly.

Hysteresis loss in iron powder

The hysteresis loss is related to the coercive force of the material. The coercive force in its turn is determined by the ability of the domain walls to move in the material. In an iron powder material impurities in the iron particles and stressed regions give rise to pinning sites that hinder domain wall motion. The coercive force raised by these causes can be reduced by using a high purity iron for the particles and provide a heat treatment procedure following the compaction to improve the stressed regions.

Another source of hindering the domain wall motion is possible grain boundaries inside the particles. One particle may consist of a number of grains, regions with a regular crystal structure, and within each grain a substructure composed of magnetic domains. With large grains, i.e. few grains in a particle, the domain walls are able to move more freely inside the particle and the coercive force contribution due to the grain boundaries is low. Grain growth inside the particles is supported by heat treatment.

However (Kordecki, et al., 1990) states that the internal stresses is the main influence on coercive force, and hence the heat treatment procedure following the compaction is the main step to be taken to reduce hysteresis loss.

3.2 Eddy current loss

According to Faraday's law of induction a varying magnetic field, **B**, will always be surrounded by an electric field, **E**. The line integral of the electric field along a closed contour C is given by the magnetic flux, Φ, crossing the surface, S, bounded by the contour.

$$\oint_C \mathbf{E} \cdot dl = -\frac{d}{dt} \int_S \mathbf{B} \cdot ds = -\frac{d}{dt} \Phi \tag{3.27}$$

If an electrical conducting material is exposed to the varying magnetic field, a current density is set up along the closed contour.

$$\mathbf{i} = \frac{\mathbf{E}}{\rho} \tag{3.28}$$

where ρ is the resistivity of the material. These eddy currents is a source of resistive power loss in the material, the instantaneous eddy current power loss per unit volume is

$$p_{ec}(t) = \rho\,\mathbf{i}^2 = \frac{\mathbf{E}^2}{\rho} \tag{3.29}$$

There are mainly two ways to reduce this eddy current loss, either by substituting the material to a higher resistivity material, or by restricting the possible paths for the eddy currents, as in a laminated core.

Eddy current loss in a lamination

A magnetic field with a uniform distribution is applied in the *z*-direction, **B** = B_z, to the laminate in Figure 3.14 with thickness *d* and width *w*. Within a thin laminate the induced electric field is assumed to be only in the *x*-direction, i.e.

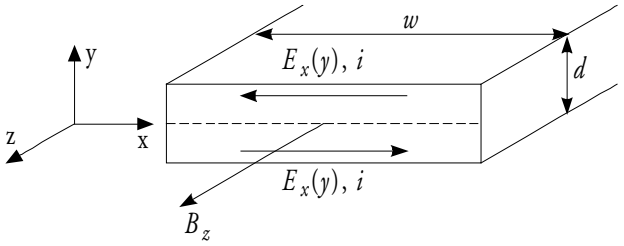

Figure 3.14: The induced electric field and corresponding eddy currents inside a laminate.

the currents flow only in the horizontal direction in the figure. The electric field is linearly dependent on the distance *y* from the centre of the laminate, **E** = $E_x(y)$. Faraday's law of induction (3.27) then gives

$$2wE_x(y) = -\frac{d}{dt}\left(2wyB_z\right) \tag{3.30}$$

and

$$E_x(y) = -y\frac{dB_z}{dt} \tag{3.31}$$

The instantaneous power loss per unit volume from (3.29) becomes

$$p_{ec}(t, y) = \frac{1}{\rho}\left(\frac{dB_z}{dt}\right)^2 y^2 \tag{3.32}$$

and the mean value of the instantaneous loss across the cross section is

$$p_{ec}(t) = \frac{1}{wd}\int_{-d/2}^{d/2}\frac{1}{\rho}\left(\frac{dB_z}{dt}\right)^2 y^2 w\,dy = \frac{d^2}{12\rho}\left(\frac{dB_z}{dt}\right)^2 \tag{3.33}$$

Finally, the eddy current loss per unit volume of a laminate is expressed as

$$p_{ec}(t) = k_{ec}\left(\frac{dB}{dt}\right)^2, \quad k_{ec} = \frac{d^2}{12\rho} \tag{3.34}$$

where k_{ec} is called the eddy current loss coefficient.

In this derivation it is assumed that the insulation between the laminates is perfect, i.e. no currents flow between laminates. Also the magnetic field produced by the eddy currents that will oppose the applied field is neglected, i.e. full field penetration in a laminate is assumed.

Eddy current loss in a cylinder

Calculations of the eddy current loss in a cylinder, with radius r_0, is similar to the above, for a laminate. Also in this case full field penetration is assumed. With cylindrical coordinates Faraday's law of induction becomes

$$2\pi r E_\varphi(r) = -\frac{d}{dt}\left(\pi r^2 B_z\right) \tag{3.35}$$

and

$$E_\varphi(r) = -\frac{r}{2}\frac{dB_z}{dt} \tag{3.36}$$

The instantaneous power loss per unit volume becomes

$$p_{ec}(t,r) = \frac{1}{\rho}\left(\frac{dB_z}{dt}\right)^2 \frac{r^2}{4} \tag{3.37}$$

and the mean value of the instantaneous loss across the cross section is

$$p_{ec}(t) = \frac{1}{\pi r_0^2}\int_0^{r_0} \frac{1}{\rho}\left(\frac{dB_z}{dt}\right)^2 \frac{r^2}{4} 2\pi r\, dr = \frac{r_0^2}{8\rho}\left(\frac{dB_z}{dt}\right)^2 \tag{3.38}$$

Finally, the eddy current loss per unit volume of a cylinder is expressed as

$$p_{ec}(t) = k_{ec}\left(\frac{dB}{dt}\right)^2, \quad k_{ec} = \frac{r_0^2}{8\rho} \tag{3.39}$$

Eddy current loss in an iron powder material

When calculating eddy current loss in a laminated core the assumption was made that the insulation was perfect and no currents exist between laminates. If the same assumption is made for an iron powder material there will only be eddy currents circling inside the iron particles and no currents between particles. By this assumption the eddy current loss in iron powder materials is independent of the geometry of a specimen but dependent on the size and shape of the particles. However this assumption is in most cases not true, the eddy current loss is, to some extent, dependent on the geometry of the specimen due to the fact that the insulation between particles is not perfect and currents between particles exist. The bulk resistivity of an iron powder material is related to the ability of the insulation between particles, i.e. a high resistivity implies a good insulation, as a consequence the eddy currents circles to a high extent only inside particles and thereby the geometry dependence is low. A decrease in insulation lowers the bulk resistivity and increases the geometry dependence of the eddy current loss.

According to the discussion above the classical eddy current loss in an iron powder material can be separated into two parts. One part that is due to eddy currents in the bulk material, i.e. currents flowing in the entire cross section of the material and one part that is due to eddy currents set up in the interior of a powder particle. The total eddy current loss is a combination of the two parts and the contribution of each part is determined by the size and shape of the specimen respectively the particle and by the bulk resistivity of the material. Below approximate expressions for the two parts are derived from (3.39).

Eddy current loss in the bulk material

The insulation between particles in an iron powder material is not perfect, i.e. to some extent current flow between particles. To calculate the influence of these currents on the eddy current loss a homogeneous material with the resistivity equal to the bulk resistivity of the iron powder material is assumed. The eddy current loss in the bulk material is determined from the currents circling in the entire cross section of a homogeneous specimen.

For a specimen with a quadratic, or close to quadratic, cross section an approximation is made in order to be able to use (3.39) for eddy current loss calculation. The quadratic cross section of the specimen is assumed to be circular with unchanged area. By this approximation the radius in (3.39) is the effective radius, r_e, for a specimen with a quadratic cross sectional area, A_q,

$$r_e = \sqrt{\frac{A_q}{\pi}} \tag{3.40}$$

With the bulk resistivity denoted ρ_{bulk} of the material the eddy current loss per unit volume of the bulk material is

$$p_{ec_b}(t) = k_{ec_b}\left(\frac{dB}{dt}\right)^2, \quad k_{ec_b} = \frac{r_e^2}{8\rho_{bulk}} \tag{3.41}$$

Obviously, the bulk eddy current loss depends on the size of the specimen, i.e. this eddy current loss part is geometry dependent.

Eddy current loss interior in particles

If the insulation between particles is assumed perfect no eddy currents will circle in the cross section of the bulk material but only in the interior of separate particles.

The approximation made here is that the material is composed of cylinder shaped particles with radius r_p and the length equal to the diameter, then (3.39) predicts the eddy current loss of one particle per unit volume if ρ is the resistivity of the particle material, in this case pure iron. In order to calculate the loss per unit volume bulk material (3.39) must be multiplied by the packing fraction, η, i.e. the total volume of particles in the bulk material divided by the total volume of the bulk material. If the bulk material is assumed to consist exclusively of powder particles, which is a good assumption

for high permeability powder materials that has only a very small part of lubrication and binder, this packing fraction is close to one. The eddy current loss per unit volume bulk material, due to currents interior in particles is then expressed by

$$p_{ec_p}(t) = k_{ec_p}\left(\frac{dB}{dt}\right)^2, \quad k_{ec_p} = \eta\frac{r_p^2}{8\rho_{Fe}} \tag{3.42}$$

This shows a squared relation between the radius of a particle and the eddy current loss. In (Krause, et. al., 1998) a relation in the cubic range is indicated, but for acicular steel particles. Normally there is a big variation in the size of particles in an iron powder material, due to that an accurate determination of the eddy current loss interior in particles is hard to make.

Total eddy current loss in an iron powder material

The total eddy current loss in an iron powder material depends partly on geometry dependent eddy currents in the bulk material and partly on eddy currents in particles, dependent on the particle size. Which part that dominates depends on the specimen size, particle size, amount of insulation etc.

By adding (3.41) and (3.42) an expression of the total eddy current loss per unit volume in an iron powder material is derived

$$p_{ec}(t) = k_{ec}\left(\frac{dB}{dt}\right)^2, \quad k_{ec} = \frac{1}{8}\left(c_b\frac{r_e^2}{\rho_{bulk}} + c_p\eta\frac{r_p^2}{\rho_{Fe}}\right) \tag{3.43}$$

where c_b and c_p are factors establishing the contribution of the eddy current loss due to eddy currents in the bulk material respectively interior in particles, c_b and c_p will be between zero and one. In a material with perfect insulation between particles, with currents circling only inside the particles, $c_b = 0$ and $c_p = 1$, and when the effect of particles are neglected, with currents circling only in the bulk material, $c_b = 1$ and $c_p = 0$. The factors c_b and c_p must be empirically determined for each material. By using (3.43) the geometry dependence of the eddy current loss can be included.

Next, the behaviour of the total eddy current loss coefficient k_{ec}, in (3.43), will be discussed. These are approximate calculations, not supported by any measurements. Though (Takajo, Ozaki, 1998) indicates a similar behaviour when measuring and calculating the imaginary part of the complex permeability, associated with the power loss, based on intra-particle eddy

currents (in particles) respectively inter-particle eddy currents (in the bulk material). They come to the conclusion that the eddy current type dominating is determined by the degree of insulation between particles.

The total loss coefficient k_{ec} in (3.43) is calculated for the iron powder materials Somaloy 500 + 0.6% LB1 and Somaloy 500 + 0.5% Kenolube. Both materials are composed of the same type of particles, with a size < 150 μm, the average particle size is assumed to be 100 μm, i.e. r_p = 50 μm. The particle eddy current coefficient, k_{ec_p}, depends on resistivity and size of particles, and is the same for the two materials. The bulk eddy current coefficient, k_{ec_b}, on the other hand depends on the resistivity of the bulk material and the specimen cross section area. The bulk resistivities of the materials differ due to different mixes and difference in heat treatment. The mix with 0.5% Kenolube and heat treated at 500°C has a bulk resistivity ρ_{bulk} > 30 μΩm and the mix with 0.6% LB1 and heat treated at 275°C has ρ_{bulk} > 1000 μΩm. The total eddy current loss coefficient of the materials are seen in Table 3.2, with r_e the effective radius of the cross section. The packing fraction, η, is assumed to be one.

To be able to determine the factors c_b and c_p for a material, the eddy current part of the total loss must be determined for a number of specimen, of the material in question, with different cross sectional areas. With the particle size and resistivity of the particle and bulk material known the factors, that should be constant for a material, can be determined.

Material	$k_{ec} = c_b \cdot k_{ec_b} + c_p \cdot k_{ec_p}$
Somaloy 500 + 0.6 % LB1	$c_b \cdot r_e^2 \cdot 10^2 + c_p \cdot 3 \cdot 10^{-3}$
Somaloy 500 + 0.5 % Kenolube	$c_b \cdot r_e^2 \cdot 4 \cdot 10^3 + c_p \cdot 3 \cdot 10^{-3}$

Table 3.2: Total eddy current loss coefficient for use in (3.43).

When high permeability and high maximum flux density is a goal, like in Somaloy 500 + 0.5% Kenolube, the amount of insulation must be minimised. As a consequence the bulk resistivity decreases and the part of the eddy current loss dependent on the geometry of the specimen increases. This behaviour is indicated in the coefficients of Table 3.2 as a higher constant in the bulk eddy current loss coefficient of the Kenolube-material. Due to the low amount of insulation iron powder materials with maximised magnetic properties are not suited for higher frequencies. In a laminated core the insulation between laminates do not effect the magnetic properties, hence the insulation layer is

made thicker and currents between laminates are most often negligible, i.e. the eddy current loss is not dependent on the bulk material cross section but on the lamination cross section.

Eddy current loss at sinusoidal flux density

In many applications the flux density is sinusoidal or approximately sinusoidal, then (3.34), (3.39) and (3.43) can be simplified to (3.45) in a laminate, (3.46) in a cylinder respectively (3.47) in an iron powder material.

Laminate
At sinusoidal flux density the instantaneous eddy current loss of a laminate is

$$p_{ec}(t) = \frac{d^2}{12\rho}(\omega\hat{B}\cos\omega t)^2 \tag{3.44}$$

Since the average of a squared cosine function over one period is one half the maximum value, the average eddy current loss per unit volume at sinusoidal flux density is

$$p_{ec} = \frac{d^2}{12\rho}\frac{(\omega\hat{B})^2}{2} = k_{ec}2\pi^2(f\hat{B})^2 \tag{3.45}$$

Cylinder
In the same way, the average eddy current loss per unit volume of a cylinder at sinusoidal flux density is

$$p_{ec} = \frac{r_0^2}{8\rho}\frac{(\omega\hat{B})^2}{2} = k_{ec}2\pi^2(f\hat{B})^2 \tag{3.46}$$

Iron powder material
Also equation (3.43) for the total eddy current loss per unit volume in an iron powder material is rewritten for sinusoidal flux density

$$p_{ec} = k_{ec}2\pi^2(f\hat{B})^2, \quad k_{ec} = \frac{1}{8}\left(c_b\frac{r_e^2}{\rho_{bulk}} + c_p\frac{r_p^2}{\rho_{Fe}}\right) \tag{3.47}$$

Skin effect

The eddy currents in (3.28) induced by a varying magnetic field will in turn produce a magnetic field opposing the flux variations inside the contour. This is neglected in the calculations above and a uniform distribution of the flux density throughout the cross section is assumed, i.e. full field penetration is assumed.

Due to the eddy currents the flux density tends to gather at the surface of a specimen, thus the flux density is highest at the surface and decreases with the distance to the centre of the specimen. This phenomenon is called skin effect, a very similar phenomenon occurs in a conductor where an alternating current generates a magnetic field that in turn produces a current opposing variations in the applied current. Calculations on the skin effect in conductors are carried out in Chapter 4.3 on winding losses. The analysis on skin effect in a magnetic material due to an applied magnetic field as discussed here, is similar to that performed in Chapter 4.3 on conductors.

A measure on the influence of the skin effect is the skin depth, which is defined as the distance from the surface of the specimen where the amplitude of a sinusoidal varying flux density has decreased to $1/e$ of the amplitude at the surface. The skin depth is expressed by

$$\delta = \sqrt{\frac{\rho}{\pi f \mu_0 \mu_r}} \tag{3.48}$$

where f is the frequency of the sinusoidal flux density, μ_0 the permeability of free space and ρ and μ_r the resistivity respectively the relative permeability of the material.

In Table 3.3 the skin depth of some different bulk materials are calculated by (3.48) at 50 Hz and 1 kHz.

Material	Silicon-iron, 3% Si, 97 % Fe	Somaloy 500 + 0.5% Kenolube	Somaloy 500 + 0.6% LB1
ρ	0.5 μΩm	30 μΩm	1000 μΩm
μ_r	6000	500	200
$\delta @ f =$ 50 Hz	0.06 cm	2 cm	20 cm
$\delta @ f =$ 1 kHz	0.01 cm	0.4 cm	4 cm

Table 3.3: Skin depths of some core materials.

When the lamination thickness or the cross sectional dimensions of an iron powder core are small compared to the skin depth the flux density is considered uniform throughout the cross section, full field penetration is assumed, and the equations derived in this chapter is valid.

3.3 Anomalous loss

If the presence of domains in a material is neglected the magnetisation will be homogeneous in space and continuous in time and the total eddy current loss is solely due to macroscopic currents in the cross section of the material or/and in the particles. This eddy current loss generated by the external applied field is sometimes called classical eddy current loss. However, the domains can not be neglected, the effect of the domains is only more or less significant depending on the material composition.

At magnetisation, the walls surrounding the domains, jumps between pinning sites, and give rise to discontinuous steps in the magnetisation. This domain wall motion gives rise to eddy currents at the walls. The loss related to these microscopic eddy currents are called anomalous loss or sometimes excess eddy current loss.

A decrease in domain size gives a material with a finer domain structure, hence the magnetisation should be more homogeneous and the anomalous contribution to the total loss should be smaller. However, in a fine domain structure there is interaction between domain walls and the domain wall jumps clustering in time and space (Bertotti, 1984). The jump of a domain wall makes the surrounding domain structure unstable and triggers the jump of neighbouring walls to occur within a short time interval. This clustering makes groups of strongly interacting domain walls to act as large domain walls, which increases the inhomogeneity of magnetisation and thereby increases the anomalous loss. In a material with larger domains, on the other hand, the walls are more separated and the interaction between walls are weaker. But due to larger domain size the magnetisation becomes inhomogeneous and anomalous loss are still present.

A thorough investigation of the physical background of the anomalous loss is performed in (Bertotti, 1984) and (Bertotti, 1985). The intimate connection between domain wall motion and anomalous loss is pointed out and the investigation concludes in the derivation of an analytical expression of the anomalous loss. A material specimen with n simultaneously active magnetic

objects, in the cross section with area A, is considered. The designation 'magnetic object' is in a material with large domains identified by a single domain wall and in a material with a fine domain structure identified by a group of strongly interacting domain walls acting as a single domain wall. Activating a magnetic object means that the domain wall, or group of domain walls, associated with the magnetic object jumps to a new site and thereby makes a contribution to the magnetisation. Every magnetic object is associated with a local coercive field. At a very low frequency it is assumed that only one magnetic object is active at a time and an applied magnetic field must exceed the local coercive field of a magnetic object to make it active. With an increase in frequency magnetic objects begins to be active more simultaneously and the active magnetic objects generate an opposing eddy current field. At an increasing frequency the applied field must exceed the local coercive field and the opposing eddy current field to activate a magnetic object. This means, to still achieve a given magnetisation at an increasing frequency, the applied field must be increased to overcome the opposing eddy current field, increasing with frequency. The eddy current field generated due to domain wall motion, or activating of magnetic objects, is responsible for the anomalous loss.

In order to get a given flux rate, dB/dt, the applied field must be increased with a field corresponding to the eddy current field. At a given time, t, the opposing eddy current field $H_e(t)$ is generated by $n(t)$ active magnetic objects in the cross section area A of a specimen

$$H_e(t) = \frac{GA}{\rho\, n(t)} \cdot \frac{dB(t)}{dt} \tag{3.49}$$

G is a dimensionless coefficient (≈ 0.136 for a 180° domain wall) and ρ the resistivity of the material. An increase in number of active magnetic objects, n, with an increasing frequency occurs. An increase in frequency gives a higher eddy current field and then the applied field balancing the eddy current field must be increased to get a given flux density. The higher applied field acting as a further pressure on nonactive regions of a sample and forces more magnetic objects to be active.

$$n(t) = n_0 + \frac{H_e(t)}{V_0} \approx \frac{H_e(t)}{V_0} \tag{3.50}$$

n_0 is the number of active magnetic objects at a low frequency and V_0 a characteristic field controlling the increase in active magnetic objects due to the

applied field. The approximation in (3.50) is, in most cases, valid for frequencies above 50 Hz.

The eddy current field and the change in flux density determine the anomalous loss per unit volume generated in the material

$$p_a(t) = H_e(t) \cdot \frac{dB(t)}{dt} \tag{3.51}$$

which together with (3.49) and (3.60) is expressed as

$$p_a(t) = \sqrt{\frac{GV_0 A}{\rho}} \cdot \left| \frac{dB(t)}{dt} \right|^{3/2} \tag{3.52}$$

The parameter V_0 is a characteristic field [A/m] that represents the microstructural effects on the anomalous loss and has to be determined experimentally. From experiments (Bertotti, 1985) it is evident that V_0 decreases with increasing cross section area of the specimen, decreasing degree of magnetic orientation and decreasing grain size. It is also stated that V_0 is proportional to the hysteresis loss. A nonoriented material, characterised by high hysteresis loss and small grain size, follows the relation

$$V_0 = 2H_{hyst} \frac{s^2}{A} \tag{3.53}$$

with H_{hyst} the hysteresis field and s the average grain size. A decreasing quotient s^2 / A increases the number of grains in the cross section, thereby decreasing the degree of simultaneously active magnetic objects. This implies an increase in the homogeneity of the magnetisation process. A decrease in H_{hyst} is also contributing to the homogeneity. As stated in the beginning of this chapter an improvement in the magnetisation homogeneity reduces the anomalous loss.

Instead of determining V_0 in (3.52), the anomalous loss expression usually is rewritten as

$$p_a(t) = k_a \left| \frac{dB(t)}{dt} \right|^{3/2} \tag{3.54}$$

with an anomalous loss coefficient, k_a, which can be determined by loss separation, treated in Chapter 3.4.

There are many extensions made on the Preisach model to make it able to handle additional phenomenas. By dynamic Preisach models suggested e.g. by (Mayergoyz, 1988) and (Bertotti, 1992) the rate-dependent domain wall

motion that is the origin of anomalous loss is included. The consequence of this extension is an enlargement of the hysteresis loop with increasing frequency due to the dynamic effects of the domain wall motion. The area enclosed by the loop modelled by these dynamic Preisach models corresponds to the total loss due to hysteresis and excess eddy currents, i.e. hysteresis loss and anomalous loss.

Anomalous loss at sinusoidal flux density

At a sinusoidal flux density the instantaneous anomalous loss expression of (3.54) becomes

$$p_a(t) = k_a(\omega \hat{B} \cos \omega t)^{3/2} \tag{3.55}$$

The numerical average value of a cosine function raised to the power of 3/2 over one period is 0.556, thus the average anomalous loss per unit volume at sinusoidal flux density becomes

$$p_a = k_a 8.76(f\hat{B})^{3/2} \tag{3.56}$$

At sinusoidal flux density the anomalous loss coefficient is determined by loss separation, the same coefficient is then also applicable when using (3.54) for non-sinusoidal waveforms of the flux density.

3.4 Loss separation

In a laminated material loss separation is used to determine an approximate expression for the total core loss, including the three loss parts described above. An analytical expression describing the losses in a core material is a great aid in applications design. Here the use of loss separation in order to define an expression for the total core loss of an iron powder material is investigated.

The total average core loss over one cycle per unit volume at any arbitrary flux density waveform, at full field penetration, is obtained by summing the expressions of the three loss parts. For a laminated material (3.1), (3.34) and (3.54) is used and for an iron powder material the total core loss is determined by (3.1), (3.43) and (3.54)

$$p_c = f A_{hyst} + k_{ec} \frac{1}{T} \int_0^T \left(\frac{dB}{dt} \right)^2 dt + k_a \frac{1}{T} \int_0^T \left| \frac{dB}{dt} \right|^{3/2} dt \tag{3.57}$$

where $f = 1/T$ is the fundamental frequency of the applied field and A_{hyst} the area enclosed by the hysteresis loop in one cycle. In a laminated core the eddy current coefficient is

$$k_{ec} = \frac{d^2}{12\rho}$$

and in case of an iron powder core

$$k_{ec} = \frac{1}{8}\left(c_b \frac{r_e^2}{\rho_{bulk}} + c_p \frac{r_p^2}{\rho_{Fe}} \right)$$

If the flux density is sinusoidal (3.57) is simplified, and derived by summing (3.26), (3.45) and (3.56) respectively (3.26), (3.47) and (3.56). The corresponding energy loss per unit volume at sinusoidal flux density is

$$\frac{p_c}{f} = k_h \hat{B}^n + k_{ec} 2\pi^2 \hat{B}^2 \cdot f + k_a 8.76 \hat{B}^{3/2} \cdot \sqrt{f} \qquad (3.58)$$

From the energy loss equation in (3.58) and measurements of the total core energy loss the unknown parameters is determined. For the two investigated iron powder materials Somaloy 500 + 0.6% LB1 and Somaloy 500 + 0.5% Kenolube the parameters k_h and n are tabulated in Table 3.1 and k_{ec} in Table 3.2. If these three parameters are known the fourth parameter, the anomalous loss coefficient k_a, is determined by fitting (3.58) to measurements of the total core energy loss. In a case with a laminated material k_{ec} is determined from the known parameters, the thickness of a laminate and the resistivity. In the case of an iron powder material however c_b and c_p in k_{ec} are unknown, and for that reason also k_{ec} must be determined by the curve fitting.

In Figure 3.15 measurements of the total core loss of Somaloy 500 + 0.6% LB1, at different flux densities, are shown as circles. The best fit of (3.58) to the measurements is seen as a continuous line. At zero frequency the whole energy loss is due to hysteresis and the hysteresis part is independent of the frequency. The eddy current part changes linearly with frequency and the anomalous part changes with the square root of the frequency. Measurements are made on a toroidal ring with outer diameter 55 mm, inner diameter 45 mm and height 5 mm. This gives a quadratic cross section with area 25 mm^2 and by (3.36) the effective radius is calculated to 2.8 mm. The eddy current

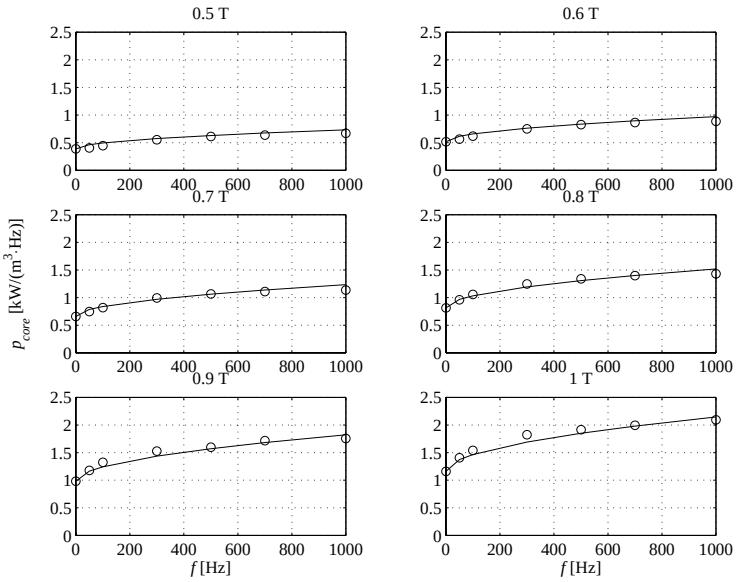

Figure 3.15: Loss separation of Somaloy 500 + 0.6% LB1, measured core loss (circles) and the best fit of equation (3.58) gives k_a = 3.6 and k_{ec} = 0 (line).

loss coefficient, from Table 3.2, becomes $c_b \cdot 8 \cdot 10^{-3} + c_p \cdot 3 \cdot 10^{-3}$. With k_h = 1160 and n = 1.6 the best fit in Figure 3.15 is obtained by k_a = 3.6 and k_{ec} = 0.

The same procedure is performed with the material Somaloy 500 + 0.5% Kenolube. With the hysteresis parameters k_h = 880 and n = 1.7 the best fit is provided when k_a = 1.4 and k_{ec} = 0. The fitted parameters of the two materials are listed in Table 3.4.

As stated in Chapter 3.3 the anomalous loss depends amongst other things on the hysteresis (3.54). Due to the more extend stress relieving heat treatment in the Kenolube-material it is less exposed to hysteresis and thereby also to anomalous loss compared to the LB1-material. This behaviour is observed from the curve fitting as a higher anomalous loss constant for the LB1-material. On the other hand the frequency dependence should be higher in the Kenolube-material, due to the lower degree of insulation the eddy current loss should be more pronounced. The zeros in the eddy current loss coefficients could be due to the small cross sectional area of the samples that keeps the geometry dependent bulk eddy current loss low.

In performing a further investigation of the frequency and flux density dependence of the core loss in the two materials, another approach is chosen. The total core loss is divided in a static and a dynamic part where the static part consist of the hysteresis loss and the dynamic part of the remaining loss. By this approach there are no restrictions on the exponents of f and B and the resulting exponents indicates the behaviour of the dynamic loss part as seen in the measurements. The new approach is expressed by, compared to (3.58),

$$\frac{p_c}{f} = \frac{1}{f}(p_{stat} + p_{dyn}) = k_h \hat{B}^n + k_{dyn} \hat{B}^{n_B} \cdot f^{n_f - 1} \tag{3.59}$$

	LB1	**Kenolube**
k_h	1160	880
n	1.6	1.7
k_a	3.6	1.4
k_{ec}	0	0
k_{dyn}	57	21
n_B	1.85	1.35
n_f	1.40	1.45

Table 3.4: Core loss parameters obtained by curve fitting.

Performing curve fitting of (3.59) to the measured total losses gives the parameters k_{dyn}, n_B and n_f of the alternative total core loss expression. The resulting parameters for the two iron powder materials are seen in Table 3.4. The Kenolube-material is exposed to higher frequency dependence due to its lower degree of insulation. The difference in the frequency exponent of the dynamic part is however only slight at this small cross sectional area.

In Figure 3.16 the agreement of the resulting curve fittings of the two core loss expressions are investigated for the two used materials. In the figure the broken lines represent the best fits of equation (3.58), while the continuous lines represent the best fits of (3.59). Measured values of the total core losses are seen as circles. The figure indicates that (3.59) gives a slightly improved agreement but the agreement of both representations is good. The dotted lines in Figure 3.16 determine the part of the total core loss associated with the static loss due to hysteresis.

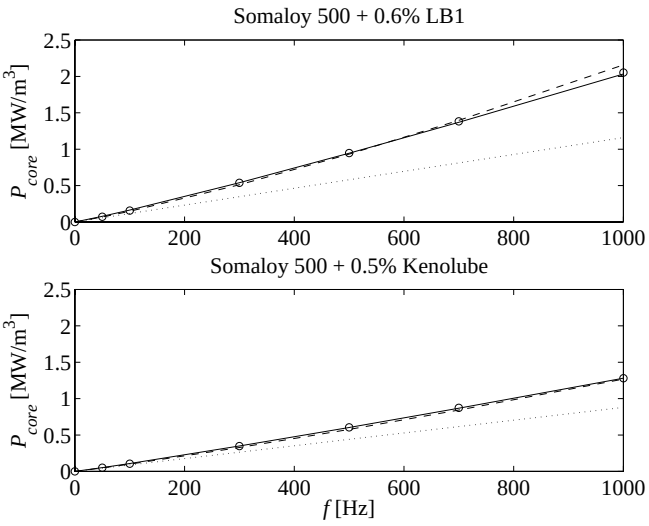

Figure 3.16: Core loss of Somaloy 500 + 0.6% LB1 respectively of Somaloy 500 + 0.5% Kenolube at B = 1 T. Measured values, dots, compared to fittings of equation (3.58), broken line, and equation (3.59), continuous line. The dotted lines show the hysteresis loss part.

3.5 Air gap loss

An air gap is most often introduced in the core of an inductor to reduce the volume of the core for a given inductance and to make the inductance more linear. At the same time the insertion of an air gap makes the magnetic flux in the core fringe around the air gap. The fringing of the flux is more thoroughly treated in Chapter 6.2 but the effects on the losses due to the fringing is discussed here.

The fringing gives rise to excess losses in both the core and the winding. The flux leaves the core at the air gap and returns in an angle more or less perpendicular to the core. In a laminated core this means more or less perpendicular to the direction of the lamination and thereby generating eddy currents in the plane of the laminate, not reduced by the lamination. This might give high eddy current loss in the core, at the air gap.

Two properties of iron powder material make this loss almost negligible in an iron powder cores. At first, there is a small air gap between every particle that gives a distributed air gap, i.e. many small air gaps in the core. The amount of fringing is determined by the length of an air gap and the very small gaps between particles make the fringing small. Second the iron powder core can be thought of as laminated in all directions, i.e. if an extra air gap is needed that give rise to fringing the eddy currents generated by the returning flux is always, independently of the direction, limited by the 'three dimensional lamination'.

In (Lee, Stephens, 1973) an empirical equation for determining the air gap loss in a laminated or a tape wound core is suggested. Here with some slight modifications

$$P_{gap} = K_{gap} \frac{n_{gap} l_{gap} w}{\rho} f \hat{B}^2 \tag{3.60}$$

where n_{gap} is the number of air gaps in the magnetic path, l_{gap} the length of an air gap, w the width of the laminate or the strip and ρ the resistivity of the core material. K_{gap} is an empirical coefficient found in Table 3.5, calculated from (McLyman, 1978), for some different configurations.

Configuration	K_{gap}
Tape wound C-core with two coils	$1.94 \cdot 10^{-4}$
Tape wound C-core with a single coil	$3.88 \cdot 10^{-4}$
Laminated EE or EI-core	$7.76 \cdot 10^{-4}$

Table 3.5: Gap loss coefficient for some different configurations.

Chapter 4

Winding losses

The winding of an inductor has a certain resistance determined by the length and cross sectional area of the conductors composing the winding and the resistivity of the conductor material. A current in the winding gives rise to resistive losses. With an alternating current eddy currents arises in the conductors and screens part of the conductor cross section, thus reducing the effective current carrying area and hence increasing the resistance of the winding.

4.1 The origin of winding losses

The winding of an inductor is usually made from copper due to its low resistivity that keeps the resistive losses of the winding low. Another advantage of copper is its high ductility, which makes it easy to wind the conductors close to the core and close to each other. Thereby the volume occupied by the winding and the length of the conductor can be minimised.

The power dissipated in the winding with a dc current applied is calculated by

$$P_w = R_{dc} I^2 \tag{4.1}$$

where R_{dc} is the dc resistance of the winding, which is for a circular conductor calculated by

$$R_{dc} = \rho \frac{l}{A} = \frac{4\rho N l_T}{\pi d^2} \tag{4.2}$$

ρ is the resistivity of copper, N is the number of turns in the winding, l_T is the average length of one turn and d is the diameter of the bare copper cross section of the conductor.

The resistivity of copper is dependent on temperature of the material. At 100°C the resistivity is about 1.33 times higher than at 20°C, where it is $\rho(20°) = 1.72 \cdot 10^{-8}$ Ωm. The resistivity as a function of the temperature, T, can be determined by

$$\rho(T) = (0.9125 + 4.125 \cdot 10^{-3} T)\,\rho(20°) \tag{4.3}$$

If an alternating current is applied to the winding the resistance of the winding will increase with the frequency of the applied current. The increase in resistance is due to skin and proximity effect that restricts the effective area of the copper cross section.

An alternating current in a conductor give rise to a magnetic field circling in the inside and at the outside of the conductor, upper plot of Figure 4.1 a. This magnetic field will in turn generate eddy currents opposing the applied current in the interior of the conductor, shown in the middle plot of the figure. This gathers the current on the surface of the conductor and shield the interior from the applied current, the current density decreases in the centre and increases on the surface, see lower plot of the figure. This behaviour is called skin effect and is similar to the skin effect discussed in Chapter 3.2 when a magnetic field is applied to a conducting material.

If the alternating current also is applied to conductors adjacent to the observed conductor the proximity effect will give additional non-uniform distribution of the current density in the conductor. The observed conductor is exposed to a field generated by the adjacent conductors, upper plot of Figure 4.1 b. If the field is uniform at the conductor, eddy currents opposing the applied current is generated in part of the conductor, middle plot of figure. This makes the current density increase in some part and decrease in the other, lower plot of figure. Two adjacent conductors with current in the same direction will have the currents gathered in the part furthest away from the other conductor. If the current direction is reversed in one of the conductors the current density will be highest in the part closest to the other conductor. In practice the proximity effect is interpreted as the eddy current effect in the conductors of a winding due to the magnetic field generated by the winding as a whole.

These eddy current effects shield more or less some parts of the conductor from the current flowing, i.e. the effective area of the cross section that is used

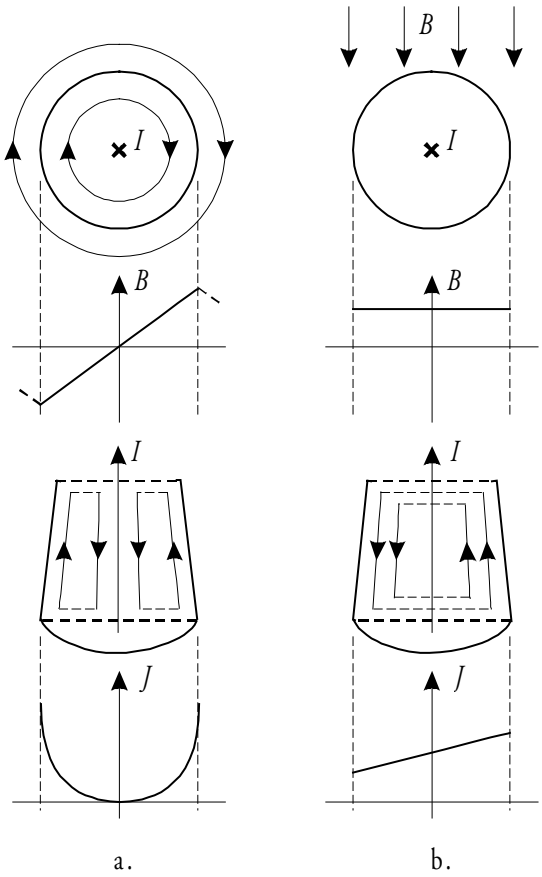

Figure 4.1: a. Skin effect and b. proximity effect in round conductors.

to conduct the current decreases. The decrease in effective area increases the resistance of the winding and in turn the winding loss increases. An increase in frequency makes the shielding more pronounced, i.e. the ac resistance increases with increasing frequency.

The skin effect makes the current in a conductor greatest at the surface and exponentially decaying with distance into the centre. The depth of penetration is defined as the depth beneath the surface of the conductor as the current is attenuated to $1/e$ or 37% of its value at the surface. This penetration depth, δ, is also called the skin depth and is calculated by

$$\delta = \sqrt{\frac{\rho_{Cu}}{\pi f \mu_0 \mu_{Cu}}} \tag{4.4}$$

where f is the frequency of the applied current, μ_0 the permeability of free space and ρ_{Cu} and μ_{Cu} is the resistivity respectively the relative permeability of copper.

If the skin depth is much less than the diameter the current flowing in the conductor is confined to a layer at the surface with a thickness of approximately the skin depth. The skin depth of copper at temperatures 20°C and 100°C and frequencies 50 Hz and 1 kHz is seen in Table 4.1.

	50 Hz	1 kHz
20°C	9.3 mm	2.1 mm
100°C	10.6 mm	2.4 mm

Table 4.1: Skin depth of copper at some different temperatures and frequencies.

4.2 Winding strategies to reduce loss

To reduce these eddy current effects Litz wires can be used. A Litz wire is composed of a bundle of many thin insulated strands, with a diameter much less than the skin depth. In the bundle each individual strand is cyclically transposed from the centre to the surface and back to the centre, each strand should periodically be located in every place in the cross section of the bundle. This stranding and transposing reduces the skin and proximity effect and makes the current density more uniform across the cross section.

To reduce the proximity effect it is however not necessary with Litz wires, it is enough to just twist the insulated strands into helical paths. Thereby the voltages induced in one half-twist of the wire are cancelled by the once induced with an opposite direction in the next half-twist. However the skin effect is not reduced by this winding strategy, it is the same as in a solid conductor having the same copper cross section as the bundle.

Drawbacks with the use of stranded wires and Litz wires is the reduced copper fill factor, i.e. the amount of copper per unit total cross sectional area occupied by the winding decreases. Further more the dc resistance of a Litz wire is higher compared to a solid conductor with equivalent total cross

sectional area and length, partly due to the decrease in copper in the cross section and partly due to increased length in the strands due to the transposing. Another drawback is the higher price of the Litz wire compared to a corresponding solid round copper conductor due to the more difficult manufacturing.

4.3 Analytical expressions

The eddy current behaviour in a round conductor can be regarded as one dimensional in cylindrical coordinates, which simplifies the derivation of an analytical expression. In a round conductor with a current applied in the *z*-direction, in cylindrical coordinates, the generated magnetic field, H_φ, is a function only of *r*.

If the external field, H_e, generated by the winding as a whole is assumed uniform across the cross section of a conductor an orthogonality exists between the skin and the proximity effect, reported in (Ferreira, 1989). Then the two eddy current parts can be calculated separately for each frequency component of the applied current, then adding the terms together to the total winding loss

$$P_w = R_{skin} I_{rms}^2 + G_{prox} H_e^2 \tag{4.5}$$

R_{skin} and G_{prox} are coefficients determined by conductor dimensions and the frequency of the applied current. The external field H_e in the winding is most often hard to determine in an accurate way, hence some approximations must be made. Under the assumption of a high permeability core and a winding that fills the entire winding window the winding loss due to skin and proximity effect can be expressed by

$$P_w = R_{ac} I_{rms}^2 = (R_{skin} + R_{prox}) I_{rms}^2 \tag{4.6}$$

where R_{skin} and R_{prox} is the winding resistance associated with the skin effect respectively the proximity effect. Derivation of expressions on that form are described below for a solid round conductor winding and a Litz wire winding.

The derived analytical expressions are used in (Bartoli, et al., 1995) and (Bartoli, et al., 1996) to calculate winding loss in high-frequency power inductors with a low permeability iron powder core. Experiments showed good agreement between calculated and measured values, i.e. the expressions show reasonable good results even if the assumption of a high permeability core is not fulfilled.

Solid round conductor winding

In (Ferreira, 1994) an analytical equation is derived for the ac resistance in a winding composed of a solid round conductor, see Appendix C. The ac resistance of the *m*th layer in the winding, with conductor diameter *d*, is

$$R_{ac_m} = R_{dc_m} \frac{\gamma}{2}\left[r_{skin} - 2\pi(2m-1)^2 r_{prox}\right] \tag{4.7}$$

with

$$r_{skin} = \frac{\mathrm{ber}\gamma\,\mathrm{bei}'\gamma - \mathrm{bei}\gamma\,\mathrm{ber}'\gamma}{\mathrm{ber}'^2\gamma + \mathrm{bei}'^2\gamma} \tag{4.8}$$

$$r_{prox} = \frac{\mathrm{ber}_2\gamma\,\mathrm{ber}'\gamma + \mathrm{bei}_2\gamma\,\mathrm{bei}'\gamma}{\mathrm{ber}^2\gamma + \mathrm{bei}^2\gamma} \tag{4.9}$$

and

$$\gamma = \frac{d}{\sqrt{2}\delta} \tag{4.10}$$

ber and bei stands for Bessel-real and Bessel-imaginary and can be calculated by infinite sums, found in Appendix D.

A porosity factor, η, is suggested in (Bartoli, et al., 1995) to improve the calculation for windings with a winding pitch greater than the winding diameter. The skin effect does not depend on the winding pitch and is not affected by the porosity factor. The external field generated by neighbouring conductors depends on the winding pitch, hence the second term in (4.7) corresponding to the proximity effect is affected by the winding pitch. The ac resistance becomes

$$R_{ac_m} = R_{dc_m} \frac{\gamma}{2}\left[r_{skin} - 2\pi\eta^2(2m-1)^2 r_{prox}\right] \tag{4.11}$$

with the porosity factor

$$\eta = \frac{d}{t}\sqrt{\frac{\pi}{4}} \tag{4.12}$$

and t is the distance between the centres of two adjacent conductors. In a winding with N_l layers, all with the same number of turns and same dc resistance (4.11) becomes

$$R_{ac} = R_{dc}\frac{\gamma}{2}\left[r_{skin} - 2\pi\eta^2\left(\frac{4(N_l^2-1)}{3}+1\right)r_{prox}\right] \tag{4.13}$$

In Figure 4.2 the resistance versus frequency is plotted for a winding composed of a solid round conductor and at some different copper diameters. The number of turns in the winding is N = 50, with an average length of one turn l_T = 10 cm, and wound in three layers, these figures are the same for all conductor diameters. The choice of the minimum resistance winding from the dimensions used in the figure is obviously depending on the operating frequency. In this example the thickest conductor is the optimum choice up to about 300 Hz but with an increasing frequency a thinner conductor may be a more efficient alternative. E.g. between just above 1 kHz and 4 kHz the

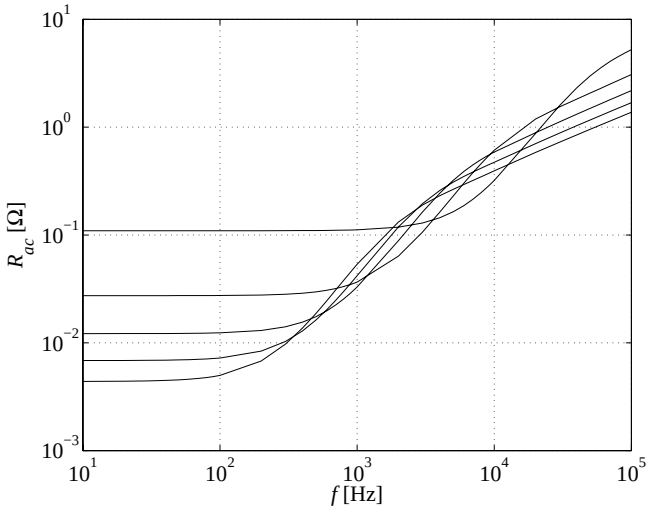

Figure 4.2: Resistance versus frequency for a winding composed of a solid round conductor with diameter, d = 1.0, 2.0 3.0, 4.0 and 5.0 mm (with decreasing dc resistance), wounded in three layers.

conductor with 2 mm diameter has the lowest resistance and between 4 kHz and 12 kHz the thinnest with d = 1 mm is the optimum choice.

It is the use of a multi-layer winding that gives this behaviour. In Figure 4.3 the same windings are used but wound in only one layer, which reduces the proximity effect considerably. In this case a thicker conductor always gives a lower resistance than a thinner one, due to the lower dc resistance. It is also noticeable that the ac resistance reduces considerably, up to about ten times, when changing from the multi-layer winding in Figure 4.2 to the single-layer winding in Figure 4.3, due to the reduction in proximity effect. It is obvious that the proximity effect is the main source of frequency dependent winding loss in an inductor using a multi-layer winding.

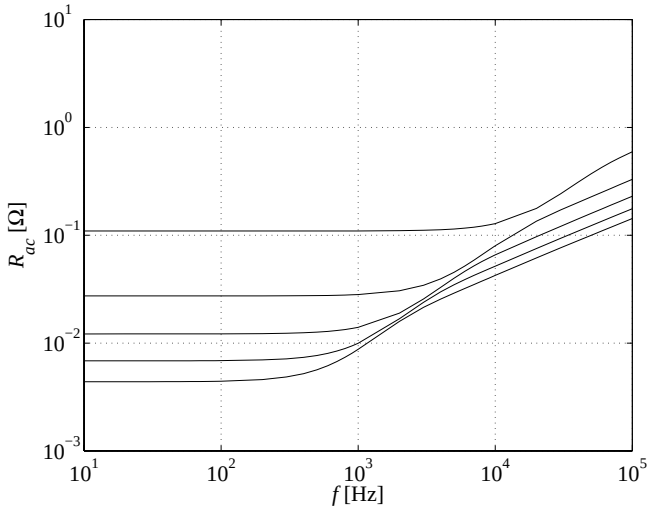

Figure 4.3: Resistance versus frequency for a winding composed of a solid round conductor with diameter, d = 1.0, 2.0 3.0, 4.0 and 5.0 mm (with decreasing dc resistance), wounded in one layer.

Litz wire winding

An analytical expression similar to (4.11) is derived in (Bartoli, et al., 1996) for the *m*th layer of a winding composed of Litz wire

$$R_{ac_m} = R_{dc_m} \frac{\gamma}{2}\left[r_{skin} - 2\pi n_s^2 \left(\eta_e^2 + \eta_i^2 \frac{p}{2\pi n_s} \right) (2m-1)^2 r_{prox} \right] \tag{4.14}$$

with the dc resistance of the layer

$$R_{dc_m} = \frac{4\rho N_m l_T}{n_s \pi d_s^2} \tag{4.15}$$

where N_m is the number of turns in the layer, n_s the number of strands in a bundle and d_s the diameter of a single strand. r_{skin} and r_{prox} is taken from (4.8) respectively (4.9). The diameter of a single strand is used to calculate γ

$$\gamma = \frac{d_s}{\sqrt{2}\delta} \tag{4.16}$$

The external porosity factor is

$$\eta_e = \frac{d_s}{t_c}\sqrt{\frac{\pi}{4}} \tag{4.17}$$

and t_c is the distance between the centres of two adjacent Litz wire conductors. The internal porosity factor is

$$\eta_i = \frac{d_s}{t_s}\sqrt{\frac{\pi}{4}} \tag{4.18}$$

and t_s is the distance between the centres of two adjacent strands. Finally, the packing factor of a Litz wire is

$$p = \frac{N\pi d_s^2 / 4}{\pi d_o^2 / 4} = N\frac{d_s^2}{d_o^2} \tag{4.19}$$

with d_o the overall diameter of the Litz wire excluding the insulating layer. For a Litz wire winding with N_l layers, with the same number of turns and the same dc resistance in each layer (4.14) becomes

$$R_{ac} = R_{dc}\frac{\gamma}{2}\left[r_{skin} - 2\pi n_s^2\left(\eta_e^2 + \eta_i^2 \frac{p}{2\pi n_s}\right)\left(\frac{4(N_l^2-1)}{3}+1\right) r_{prox} \right] \quad (4.20)$$

In Figure 4.4 equation (4.20) is used to calculate the ac resistance for two different Litz wires, both composed of strands with a diameter, d_s = 0.32 mm. The one with the highest dc resistance has n_s = 10 and an overall diameter of d_o = 1.2 mm, and the other one has n_s = 42 and d_o = 2.5 mm. The windings are wound in three layers with N = 50 and l_T = 10 cm. Also the resistance of the two windings from Figure 4.2 with diameters d = 1.0 and 2.0 mm wound in three layers are seen, they have about the same amount of copper in the cross section as respectively Litz wire winding, i.e. about the same dc resistance. The increase in length of the Litz wire due to the transposing is neglected.

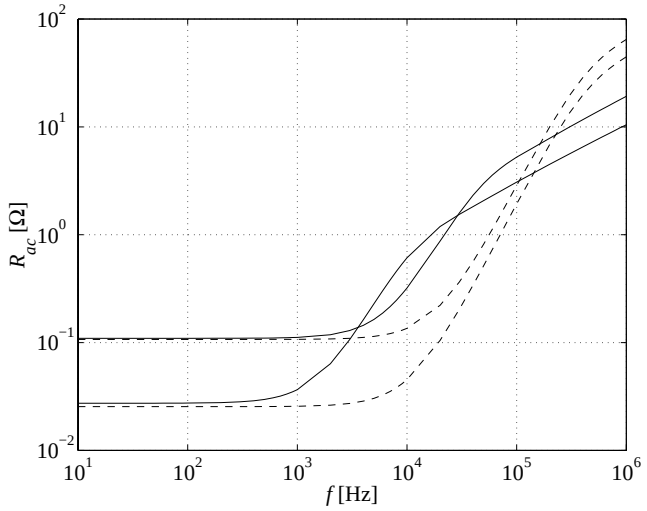

Figure 4.4: Resistance versus frequency for two Litz wire windings, broken lines, and two solid round conductor windings, continuous lines, with about the same dc resistance.

Obviously, the stranding and transposing of the Litz wire effectively reduces the eddy current effects at increasing frequency, but only up to certain level. At low frequencies the dc resistance is the same but the Litz winding requires a bigger space, here the overall diameter is about 20% greater. The conclusion is that a Litz wire is favourable only in a limited frequency range

depending on the winding configuration. In this example the Litz wire is favourable from 300 Hz to 130 kHz for the wire with 42 strands, lowest dc resistance, and from 1 kHz to 150 kHz for the one with 10 strands. At low frequencies where the resistance is about the same the solid round wire is preferred due to its better utilisation of the winding area and its lower price. The price of Litz wire is in the size of about ten times the price of solid round copper wire.

4.4 Air gap loss

The air gap loss in a core is treated in Chapter 3.4. The fringing of the flux around an air gap also increases the losses in the winding.

If the winding is in the vicinity of an air gap the fringing flux might penetrate the winding in a transverse direction and give rise to excess loss in the winding. The behaviour of this loss is similar to the proximity loss, described in preceding chapter, with the difference that the external field is determined by the fringing of the flux and not adjacent conductors. The magnetic field distorts the current density in the conductors, thus increasing the ac resistance of the winding.

In an iron powder core the distributed air gaps makes each air gap length very small, hence minimising the fringing and greatly reducing the air gap loss generated in the winding.

Chapter 5

Thermal heating

The losses generated in the core and the winding of an inductor give rise to heating. The heat is transferred to the surface and then further to the ambient by radiation and convection. The convection can be forced or free, in forced convection the inductor is ventilated by a fan or suchlike and in free convection air is circulating just due to the physical fact that hot air rises and gives space for cooler air. An equilibrium temperature is reached when the heat generated by the losses balances the heat transferred away by radiation and convection.

When designing power inductors the temperature rise is most often a restricting variable. Reduction of the size also reduces the cooling surfaces of the inductor and consequently the equilibrium temperature rises. Too high temperatures may deteriorate, or even destroy, the insulation of an inductor, e.g. in the winding, between laminates and between particles in an iron powder core. Also the maximum allowed temperature of neighbouring components might be a restriction.

A reasonably accurate determination of the temperature rise reduces the need of safety margins and may give the possibility of further optimising a component. However an analytical determination of the temperature is an intricate matter and some simplifying assumptions must be done.

5.1 Conduction

The heat generated inside the inductor, P_{cond}, must be conducted through the area A to the surface to be cooled away. The rate of heat flow per unit area is calculated as

$$q_{cond} = \frac{P_{cond}}{A} \tag{5.1}$$

The heat flows from a higher temperature to a lower, with the temperature difference dT the heat flow perpendicular to a lamina with thickness dx and thermal conductivity λ becomes

$$q_{cond} = \lambda \frac{dT}{dx} = \frac{dT}{R_T} \tag{5.2}$$

where $R_T = dx / \lambda$ is the thermal resistance.

The temperature rise inside a core in the shape of a long homogeneous cylinder with a heat generation that is uniform over the volume will be investigated. The cylinder has a length l and the cross section is seen in Figure 5.1, the heat generation per unit volume, p_c, is uniform inside the cylinder.

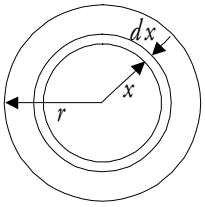

Figure 5.1: Cross section of a cylinder for calculation of temperature rise.

The conduction is assumed to be only in radial direction. The heat flow through the area at radius x is the heat produced within the radius divided by the area.

$$q_x = \frac{P_x}{A_x} = \frac{p_c \pi x^2 l}{2\pi x l} = \frac{p_c}{2} x \tag{5.3}$$

The temperature difference inside the core is calculated by (5.2)

$$dT = \frac{1}{\lambda} q_x dx = \frac{p_c}{2\lambda} x \, dx \tag{5.4}$$

and integration from 0 to r gives the difference in temperature between the centre and the surface of the core

$$\Delta T_c = \frac{p_c}{2\lambda}\int_0^r x\,dx = \frac{p_c}{4\lambda}r^2 \tag{5.5}$$

An approximate comparison is made between the conduction capability of a thermally isotropic iron powder material and a highly anisotropic laminated material. (Smith, 1985) calculates the effective thermal conductivities in a laminated material composed by 0.3 mm laminates of silicon steel with a thermal conductivity of 42 W/(m°C) and an insulating material with a thermal conductivity of 0.17 W/(m°C), the lamination pack has a stacking factor of 0.95. The effective thermal conductivity perpendicular to the laminates becomes λ_1 = 3.1 W/(m°C) and in a parallell direction λ_2 = 42 W/(m°C). The rate of heat, q, will be conducted the distance x in the laminated material, the assumption is made that $q/2$ is conducted parallell to the laminates and $q/2$ perpendicular to the laminates. Then the temperature rise in the laminated material, expressed with (5.2), is

$$\Delta T_L = \frac{q}{2}\left(\frac{x}{\lambda_1}+\frac{x}{\lambda_2}\right) = 0.17qx \quad \Rightarrow \quad R_T = 0.17x$$

The thermal conductivity in the iron powder material is λ = 17 W/(m°C) in both directions and the temperature rise becomes

$$\Delta T_P = q\frac{x}{\lambda} = qx\frac{1}{\lambda} = 0.059qx \quad \Rightarrow \quad R_T = 0.059x$$

This very approximate calculation gives a thermal resistance almost three times higher in the laminated material than in the iron powder material due to the anisotropy.

5.2 Radiation

The rate of heat per unit area dissipated from the surface by radiation is determined by the Stefan-Boltzmann law

$$q_{rad} = \sigma\varepsilon(T_s^4 - T_a^4) \tag{5.6}$$

where σ = 5.67·10^{-8} W/m^{2}K^4 is a constant and ε is the emissivity of the surface, ε = 1 for a blackbody. T_s is the surface temperature and T_a is the ambient temperature, in Kelvin.

The equation is derived under the assumption that the sample is enclosed on every side by very large planes, a very large plane can be treated as a blackbody. Also influences of radiation from the surroundings are neglected.

5.3 Convection

The equation for calculating the rate of heat per unit area transfered from the surface due to convection is

$$q_{conv} = \bar{h}(T_s - T_a) \tag{5.7}$$

where $\bar{h}$ is the average heat transfer coefficient and depends on many factors, like temperature, size and orientation of the surface and if the air flow are laminar or turbulent. It is impossible to find any general expression of the heat transfer coefficient but for a irregular solid (Holman, 1986) suggests

$$\bar{h} = 1.32\left(\frac{T_s - T_a}{L}\right)^{1/4} \tag{5.8}$$

which is valid for isothermal surfaces at a laminar air flow and atmospheric pressure. L is the characteristic length defined as the distance an air particle travels in the boundary layer and is shown for two different geometrical configurations in figure 5.2.

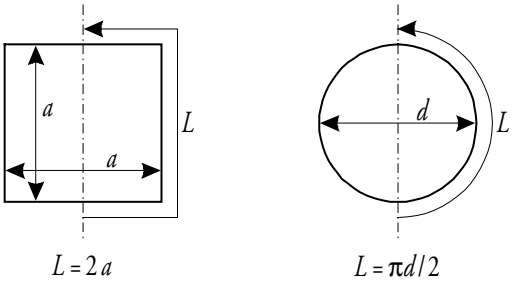

Figure 5.2: Characteristic length, L, for a long sample with a quadratic respectively a round cross section.

The flow at the irregular solid is laminar if

$$\frac{0.050}{(T_s - T_a)^{1/3}} < L < \frac{2.3}{(T_s - T_a)^{1/3}} \tag{5.9}$$

(5.8) inserted in (5.7) gives the rate of heat per unit area transferred by convection for an irregular solid

$$q_{conv} = 1.32 \frac{(T_s - T_a)^{5/4}}{L^{1/4}} \tag{5.10}$$

The distance to adjacent surfaces is of great importance, if the spacing between to surfaces is less than 10 mm the convection is smaller than calculated above and if the spacing approaches 3 mm the surfaces give no contribution to the total convection (Snelling, 1988).

5.4 Thermal calculations

Thermal calculations on an inductor at steady state operation are performed to investigate the influence on interior temperature rise due to heat transfer by conduction inside the inductor. The inductor has a toroidal core made of an iron powder material with isotropic thermal properties and a quadratic cross section with area A_c. To simplify calculations the cross section is assumed to be circular with equal area A_c and the characteristic radius r_c. A winding consisting of a round enamelled copper wire is wound in three layers on the core, Figure 5.3. Within the winding a polyester film is wound on the core to give an insulation layer between the core and the winding, the film is wound with an overlap resulting in an insulation of three layers of the film. A similar insulating layer is also wound on the outside of the winding. The winding covers the entire core surface. The power loss is assumed uniformly generated in the core respectively in the winding.

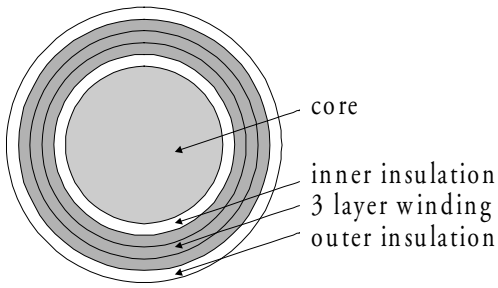

Figure 5.3: Circular cross section of toroidal inductor.

The including components have the following data:

Core:	iron powder	
	inner diameter,	d_i = 100 mm
	outer diameter,	d_o = 150 mm
	mean length,	$l_c = \pi(d_i+d_o)/2$ = 393 mm
	side length of cross section,	$a = (d_i-d_o)/2$ = 25 mm
	cross section area,	A_c = 625 mm^2
	char. radius of cross section,	$r_c = \sqrt{(A_c/\pi)}$ = 14.1 mm
	thermal conductivity,	λ_c = 17 W/(m°C)
Winding:	round enamelled copper	
	diameter,	d_{Cu} = 1.5 mm
	number of layers,	N_l = 3
	thermal conductivity,	λ_{Cu} = 386 W/(m°C)
Insulation:	polyester film	
	thickness,	t_i = 3·50 µm
	thermal conductivity,	λ_i = 0.15 W/(m°C)
Power loss:	core,	P_c = 20 W
	winding,	P_w = 30 W

The power loss in the core per unit volume is

$$p_c = \frac{P_c}{A_c l_c} = 81.4 \text{ kW/m}^3$$

The difference in temperature between the centre and the surface of the core is calculated by (5.5)

$$\Delta T_c = \frac{p_c}{4\lambda_c} r_c^2 = 0.24 \text{ °C}$$

Due to the fact that the radius of the insulation is much greater than the thickness of the insulating layer the area perpendicular to the heat flow is assumed constant throughout the insulation and the rate of heat through the inner insulation is

$$q_{ii} = \frac{P_c}{A_i} = \frac{P_c}{\pi r_c l_c} = 1.15 \text{ kW/m}^2$$

The thermal resistance of the inner insulating layer is

$$R_i = \frac{t_i}{\lambda_i} = 1.0 \text{ m°Cm}^2/\text{W}$$

and by (5.2) the temperature difference in the inner insulating layer becomes

$$\Delta T_{ii} = R_i q_{ii} = 1.15 \text{ °C}$$

The three layers of winding is seen as a homogeneous layer of copper with thickness $3d_{Cu}$ and due to the high thermal conductivity of copper the temperature rise in this copper layer is neglected. The rate of heat through the outer insulating layer is composed by the loss in the core and in the winding

$$q_{io} = \frac{P_c + P_w}{A_{io}} = \frac{P_c + P_w}{\pi(r_c + N_l d_{Cu}) l_c} = 2.18 \text{ kW/m}^2$$

The thermal resistance of the outer insulating layer is the same as of the inner layer above which gives the temperature difference

$$\Delta T_{io} = R_i q_{io} = 2.18 \text{ °C}$$

The total rise in temperature between the surface of the inductor and the centre of the core becomes

$$\Delta T = \Delta T_c + \Delta T_{ii} + \Delta T_{io} = 3.6 \text{ °C}$$

The equilibrium surface temperature of the inductor is reached when the heat generated by the losses balances the heat transferred away by radiation and convection, i.e.

$$q_{loss} = q_{rad} + q_{conv} \tag{5.11}$$

q_{loss} is derived by dividing the total power loss by the total surface area, q_{rad} is taken from (5.6) and q_{conv} from (5.10). If the entire core is covered by the winding (5.11) becomes, with temperatures in Kelvin,

$$\frac{P_c + P_w}{A_{surf}} = 1.32 \frac{(T_s - T_a)^{5/4}}{L^{1/4}} + \sigma\varepsilon(T_s^4 - T_a^4) \tag{5.12}$$

The inductor with quadratic core cross section has the overall dimensions:

inner diameter, $D_i = d_i - 2N_l\, d_{Cu} = 91$ mm
outer diameter, $D_o = d_o + 2N_l\, d_{Cu} = 159$ mm
thickness, $t = a + 2N_l\, d_{Cu} = 34$ mm

Then

$$A_{surf} = 2\frac{\pi}{4}(D_o^2 - D_i^2) + \pi(D_o + D_i)t = 0.0534 \text{ m}^2$$

and

$$L = \frac{D_o - D_i}{2} + t = 0.068 \text{ m}$$

The total power that will be dissipated is 50 W, i.e. the cooling of the inductor should be 936 W/m^2. To manage this, with an ambient temperature T_a = 40°C and an emissivity of the surface ε = 0.9, the surface temperatures becomes T_s = 100°C. At the temperature difference of 60°C the characteristic length should be 0.013 < L < 0.59 m to get a laminar flow, according to (5.9). This criterion is well satisfied in this example. Of the total power transferred away is 54% transferred by radiation and 46% by convection. The maximum temperature in the inductor, according to the calculations above, becomes less than 104°C. It is obvious that the temperature rise in the interior of an inductor most often can be neglected in comparison to the temperature rise of the surface. This is owing to the large area for conducting heat to the surface together with relatively short path lengths and the high thermal conductivities of the involved materials.

The parameter sensitivity in the determination of the surface temperature by (5.12) is investigated in Figure 5.4. The variation in the surface temperature due to a 10% variation in some of the parameters of (5.12) is plotted. A 10% change in the total power loss gives a 5% change in the surface temperature while a 10% change in the emissivity, the coefficient of convection or the ambient temperature gives a change of about 2 - 3%. Consequently a possible error in the emissivity, convection coefficient or ambient temperature has only a limited impact on the resulting surface temperature.

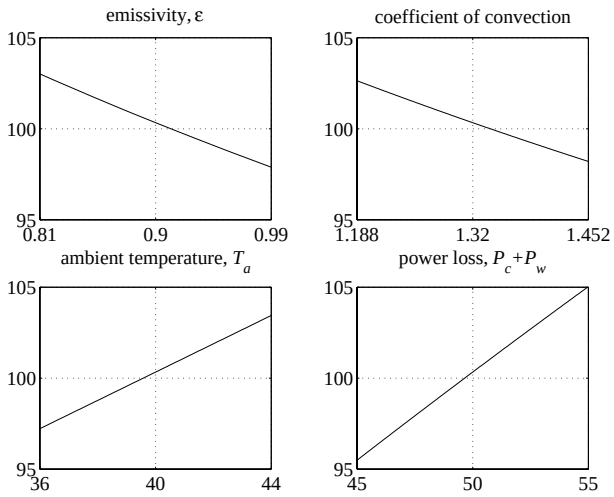

Figure 5.4: Sensitivity in the determination of the surface temperature, T_s, due to a 10 % variation in some parameters of equation (5.12).

Chapter 6

Inductor design program

A program for design of power inductors is developed in the software environment MATLAB®. The program calculates a design from a set of specified application parameters. In the program a choice can be made between some different core materials, core geometries and winding configurations. The program makes use of the equations derived previously in the thesis for calculating losses and thermal heating.

6.1 The program structure

The flow chart in Figure 6.1 shows the program routine seen by the user. The user interface is the input window, Figure 6.2, where all the data needed for computation are entered.

At first the core material, core geometry and the winding configuration are chosen. Three databases containing the possible materials, geometries respectively windings to chose between are included in the program. At the moment only a small number of items are included in the different databases but new can be added.

The material database currently includes three different materials to chose between. The materials are two Soft Magnetic Composite materials based on iron powder that are discussed in this thesis (list of properties in Appendix B) and a laminated material based on a silicon-iron alloy. When selecting a material a window showing the dc hysteresis loop together with the bulk resistivity, coercivity and remanence appears to give an idea of the magnetic and electric behaviour of the selected material. These parameters with the addition of e.g. the permeability curve, thermal conductivity, density and core

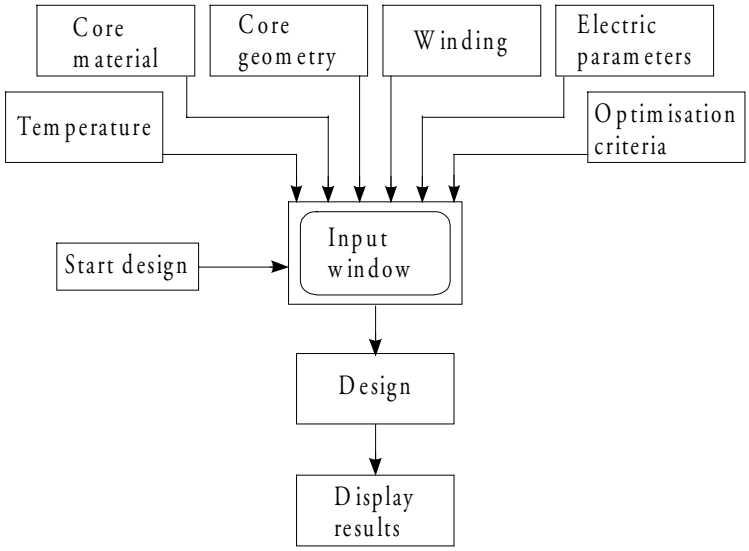

Figure 6.1: Flow chart of the inductor design program outline.

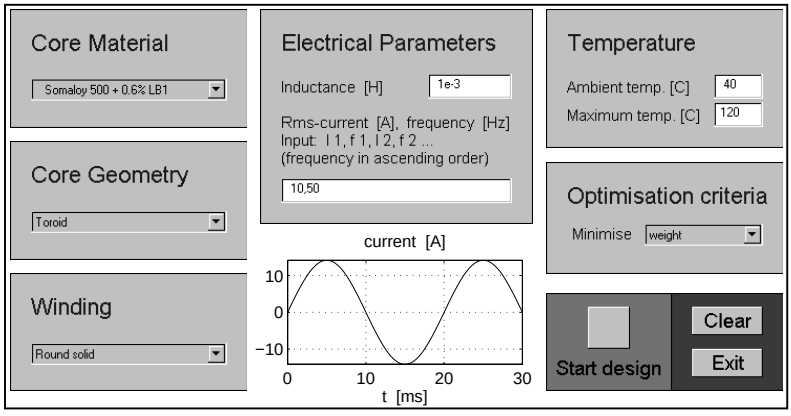

Figure 6.2: The input window – the main window of the program where all data are inputted.

loss coefficients of the selected material is also loaded from the database into the program for use in the subsequent calculations.

Core configurations currently available in the core geometry database are EE-, EI-, C- and toroidal cores. When selecting a core type a window appears

showing the chosen geometry. The window also contains a field for setting the number of air gaps in the core, which is a fixed parameter in the following design procedure. Also possible restrictions on the geometry can be defined.

The winding configurations possible to choose between consist of round solid conductors, square solid conductors or Litz wires. The choice activates a window for choosing a number of parallel conductor strands in a turn, the default value is 1.

Next the electrical parameters, inductance and current, will be fed in. The current is divided in its frequency components and fed in as a vector of rms values and its corresponding frequencies. The resulting current waveform composed of the frequency components is seen in a plot in the input window. This step provides the design procedure with the current and frequency components, the total rms and peak values of the current and of course the inductance.

The input window also contains fields for changing the ambient temperature and maximum allowed temperature of the inductor. Default values are 20°C for the ambient temperature and 120°C as the maximum allowed temperature. The maximum level is set to 120°C to ensure no long time changes in the materials due to over-heating, but due to e.g. adjacent components with lower temperature limits the level may need to be decreased.

Finally, before starting the design procedure an optimisation criterion should be selected. The criteria, or object functions, to choose between is minimum total weight and minimum cost, where cost is determined by the cost of material consumption and the cost due to losses arising at utilisation.

6.2 The design procedure

When all selections of the input window, seen in Figure 6.1, are made, the design step begins. The design procedure hiding behind this square is shown as a flow chart in Figure 6.3. The procedure starts with a set of parameters describing the geometry of the core and also containing the current density in the winding. In the subsequent design the properties of the design defined by the parameter set are calculated. Then the parameter set is varied until the optimal design with respect to the chosen optimisation criteria is found. As seen in Figure 6.3 the design procedure includes six steps for calculating the properties of the design.

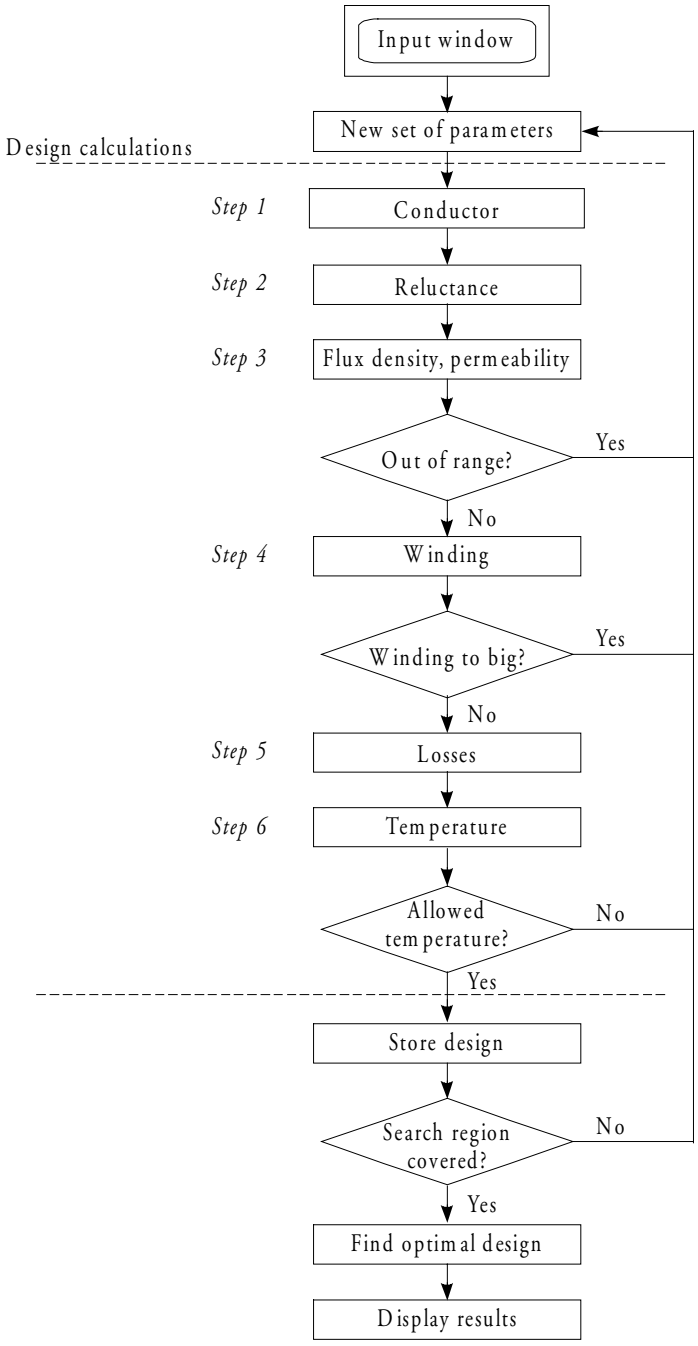

Figure 6.3: Flowchart of the design procedure.

When the final design is found the program presents an outline of the inductor with a list of core and winding dimensions. Also the calculated properties of the design, like maximum flux density in the core, power loss and surface temperature are presented.

In this chapter the design procedure is described for an iron powder toroidal core with a winding composed of a solid round conductor, but the differences due to other materials, core geometries and winding configurations are limited.

The set of parameters used in the design procedure for defining the inductor consists of the geometrical dimensions of the selected core type, Figure 6.4, the air gap length, l_{gap}, and the rms current density, J_{rms}. The set of parameters for the toroid is [D_i, D_o, d, l_{gap}, J_{rms}].

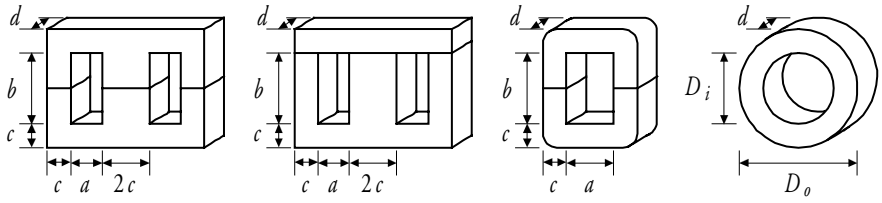

Figure 6.4: Dimensional parameters of EE-, EI-, C-, respectively toroidal cores.

Step 1. Conductor

The cross sectional copper area of the conductor, A_{Cu}, is calculated by the total rms current, I_{rms}, rms current density, J_{rms}, and the number of parallel strands, n_{par}

$$A_{Cu} = \frac{I_{rms}}{J_{rms} n_{par}} \tag{6.1}$$

Then a conductor with the diameter of the bare copper, d_{Cu}, closest to the calculated is selected from a table of standard conductor dimensions (Appendix E). From the table also the overall diameter of the conductor, d_{cond}, is taken. After selecting the conductor from the table the current density must be re-calculated by (6.1) using the selected copper area.

In this step also the skin depth of the conductor is calculated at the different frequency components, $f(n)$, of the applied current, to be used later when the winding losses are calculated.

$$\delta(n) = \sqrt{\frac{\rho_{Cu}}{\pi \mu_0 \mu_{Cu} f(n)}} \tag{6.2}$$

with the resistivity, ρ_{Cu}, and relative permeability, μ_{Cu}, of copper.

Step 2. Reluctance
The reluctance is the magnetic resistance of the magnetic path in the inductor. Before calculating the reluctance of the core the cross sectional area, A_{core}, and the mean magnetic length, l_{core}, i.e. the average length the flux travels in the core, is determined. For the toroidal core with the number of air gaps, n_{gap},

$$A_{core} = \frac{D_o - D_i}{2} d \tag{6.3}$$

and

$$l_{core} = \pi \frac{D_o - D_i}{2} - n_{gap} l_{gap} \tag{6.4}$$

As discussed in Chapter 3.5 the flux in the core fringes in the vicinity of the air gap. Because of this fringing the effective cross sectional area of the air gap increases, Figure 6.5, and hence reduces the flux density in the gap. A

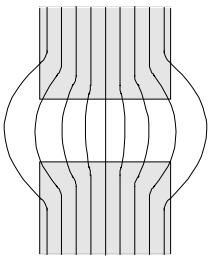

Figure 6.5: Fringing flux at the air gap.

general analysis of the fringing and its influence on the behaviour of the inductor is complicated since, as the gap length increases the fringing becomes dependent not only on the gap length but also on the configuration and geometry of the winding and the core. However, in (Snelling, 1988) an expression for calculating the effective semi-width of the gap is proposed (a

similar expression is suggested by (Lee, et al., 1988)). The radius of a core with a circular cross section or the half side of a squared cross section increases by a fringing factor, k_{fringe}, times the air gap length, with

$$k_{fringe} = 0.241 + \frac{1}{\pi}\ln\left(\frac{l_{leg}}{l_{gap}}\right) \tag{6.5}$$

where l_{leg} is the total inside length of the leg containing the air gap. For the EE-, EI- and C-core in Figure 6.4 $l_{leg} = b$, while for the toroid it is assumed that $l_{leg} = \pi D_i/2$, i.e. half the inside perimeter. (Snelling, 1988) claims an accuracy within 2% when calculating the effective permeability of a pot core over a wide range of gap lengths by using (6.5). It is also stated that (6.5) is valid if the gap length is much shorter than the width of the gap and l_{leg}/l_{gap} is larger than about 5. However the calculation of the fringing factor is valid only if the winding does not cover the gap. A winding surrounding the gap has a tendency of keeping the flux better inside the core and reduces the fringing (Lee, et al., 1988). By using the fringing factor according to (6.5) the equivalent cross sectional air gap area of the toroid becomes

$$A_{gap} = \left((D_o - D_i)/2 + k_{fringe} l_{gap}\right) \cdot \left(d + k_{fringe} l_{gap}\right) \tag{6.6}$$

Now the reluctance of the air gap and the core can be calculated. The general expression for calculating the reluctance is

$$R = \frac{l}{\mu A} \tag{6.7}$$

The total reluctance of the air gaps becomes

$$R_{gap} = n_{gap} \frac{l_{gap}}{\mu_0 A_{gap}} \tag{6.8}$$

and for the core

$$R_{core} = \frac{l_{core}}{\mu_0 \mu_{core}(B_{peak}) A_{core}} \tag{6.9}$$

where the relative permeability is non-linear and depends on the peak value of the flux density. In the toroidal core the reluctances, R_{gap} and R_{core}, are in series and the total reluctance of the magnetic path is

$$R_{tot} = R_{gap} + R_{core} = \frac{1}{\mu_0}\left(n_{gap}\frac{l_{gap}}{A_{gap}} + \frac{l_{core}}{\mu_{core}A_{core}} \right) \tag{6.10}$$

Step 3. Flux density and permeability

The permeability μ_{core} in (6.9) is the amplitude permeability (Chapter 2.1) and depends on the peak value of the flux density in the core. The permeability as a function of the peak flux density is taken from the $B_{peak}H_{peak}$-curve of the selected material (Figure 6.6 shows the curve for Somaloy 500 + 0.6% LB1). The permeability at a flux density waveform with peak value B_{peak} is calculated by taking the slope of a line between origo and the point (H_{peak}, B_{peak}) on the curve in Figure 6.6.

The $B_{peak}H_{peak}$-curve of the selected material is determined by the Preisach model, Chapter 3.1. A number of *BH*-loops over a wide range of amplitudes are modelled by Preisach and the curve in Figure 6.6 corresponds to peak values of *B* and *H* for the set of modelled loops.

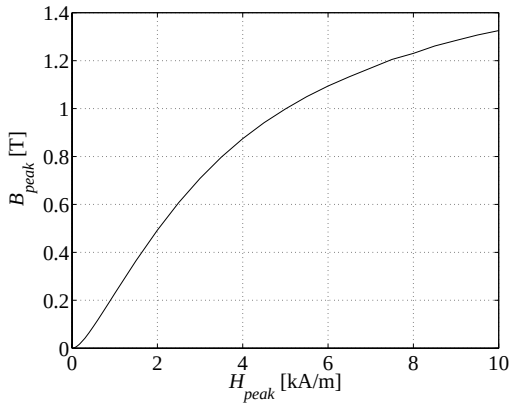

Figure 6.6: $B_{peak}H_{peak}$-curve, peak values of *B* and *H* taken from loops modelled by Preisach. The slope between origo and a point on the curve corresponds to the amplitude permeability at the point.

The material is assumed to be linear in the region $-B_{peak} < B < B_{peak}$ to simplify calculations, i.e. the permeability is constant. From Ampere's law the so-called 'Ohm's law for magnetic circuits' can be derived, with the

magnetomotive force, Ni, driving the flux, $\Phi = BA_{core}$, determined by the total reluctance, R_{tot}, in the circuit

$$Ni = \Phi R_{tot} = BA_{core} R_{tot} \tag{6.11}$$

For the toroid $R_{tot} = R_{gap} + R_{core}$, with reluctances from (6.8) and (6.9) and changing to the peak value of current and flux density (6.11) becomes

$$NI_{peak} = \frac{B_{peak}}{\mu_0}\left(n_{gap} l_{gap} \frac{A_{core}}{A_{gap}} + \frac{l_{core}}{\mu_{core}(B_{peak})} \right) \tag{6.12}$$

The permeability and the flux density in the core are determined by finding the B_{peak} that satisfies (6.12). Since the number of turns, N, is not yet determined, N must be substituted with known parameters.

The inductance of an inductor is defined by

$$L = \frac{d\Psi}{di} = \frac{N d\Phi}{di} \tag{6.13}$$

with the flux linkage Ψ. If the material is assumed linear (6.13) can be rewritten as

$$L = \frac{N\Phi}{i} \tag{6.14}$$

and (6.14) together with (6.11) can be written as

$$L = \frac{N}{i}\frac{Ni}{R_{tot}} = \frac{N^2}{R_{tot}} \tag{6.15}$$

which implies that the inductance is dependent only on the magnetic circuit and independent on the current, if a linear material is assumed. Now, with N substituted, (6.11) becomes

$$B_{peak} = \frac{I_{peak}}{A_{core}}\sqrt{\frac{L}{R_{tot}}} \tag{6.16}$$

and with (6.8) and (6.9)

$$B_{peak} = \frac{I_{peak}}{A_{core}} \sqrt{\frac{\mu_0 L}{\frac{n_{gap} l_{gap}}{A_{gap}} + \frac{l_{core}}{\mu_{core}(B_{peak}) A_{core}}}} \tag{6.17}$$

Figure 6.7 shows the left hand side (broken line) respectively the right hand side (continuous line) of (6.17) as a function of B_{peak}, the crossing point satisfies the equation and determines the peak flux density flowing in the toroidal core, in this case B_{peak} = 0.95 T. In practice this is done in MATLAB by use of the function *fzero* that finds the zero of the subtraction (left hand side) – (right hand side). The permeability μ_{core} can be determined by calculating the slope of a line between origo and the point at B_{peak} on the $B_{peak}H_{peak}$-curve in Figure 6.6, with B_{peak} = 0.95 T the permeability becomes μ_{core} = 165. With the permeability of the core known the total reluctance of the toroid is calculated by (6.10).

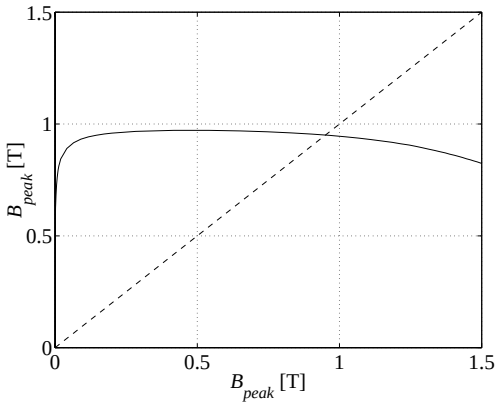

Figure 6.7: Left hand side (broken line) respectively right hand side (continuous line) of (6.17) as a function of B_{peak}. The crossing point satisfies the equation.

If, due to a bad choice of geometry, the right hand side of (6.17) is always above the left hand side (no crossing between the continuous and the broken line in Figure 6.7) a parameter, *OutOfRange*, is set to 1 in the program.

Step 4. Winding
If the parameter *OutOfRange* is still 0, the procedure continues by calculating the winding properties. The number of turns needed in the winding is calculated from the desired inductance. The expression is derived from (6.15)

$$N = \sqrt{L R_{tot}} \tag{6.18}$$

An approximate winding configuration is determined by calculating the number of strands, the number of layers and the number of turns in each layer. It is assumed that there is no distance between two adjacent conductors in a layer and that the height of a layer equals the conductor diameter, including the insulation.

The total number of conductor strands in the winding is calculated by

$$N_{strand} = n_{par} N \tag{6.19}$$

For the toroid it is also assumed that the winding is uniformly distributed throughout the core. The number of turns fitting in a layer changes with the distance to the core on a toroid. Expressions for the number of strands in layer m of the winding on the inside respectively the outside of the core is

$$\begin{aligned} N_{in\ layer\_in}(m) &= \pi(D_i - (2m-1)d_{cond}) / d_{cond} \\ N_{in\ layer\_out}(m) &= \pi(D_o + (2m-1)d_{cond}) / d_{cond} \end{aligned} \tag{6.20}$$

These expressions are used in the design program for calculating the number of turns in each layer and also the number of layers on the inside respectively the outside. The MATLAB routine is

```
% Layers on the inside of the core
m = 1
N_in layer_in(m) = min[ floor (π (D_i - (2m - 1) d_cond) /d_cond), N_strand ]
N_rest = N_strand - N_in layer_in(m)
while (N_rest > 0) & (N_in layer_in(m) > 0)
    m = m + 1;
    N_in layer_in(m) = min[ floor (π (D_i - (2m - 1) d_cond) /d_cond), N_rest ]
    N_rest = N_rest - N_in layer_in(m)
end
N_layer_in = m

if N_in layer_in(m) ≥ 0
```

```
    % Layers on the outside of the core
    m = 0
    N_rest = N_strand
    while N_rest > 0
        m = m + 1
        N_in layer_out(m) = min[ floor (π (D_o + (2m - 1) d_cond) /d_cond), N_rest ]
        N_rest = N_rest - N_in layer_out(m)
    end
    N_layer_out = m

else
    WindingToBig = 1
end
```

If $N_{in\ layer\_in}(m)$ becomes negative the winding window is to small to contain the winding and the parameter *WindingToBig* is set to 1.

Calculation of the winding configuration for the other core types are simpler, because each layer contains the same number of strands and the number of layers are the same on the inside and on the outside.

Step 5. Losses

Core losses are treated in Chapter 3 and winding losses in Chapter 4. In order to calculate core losses, the Preisach model described in Chapter 3.1 is used. The general data needed in the model is only the limiting dc hysteresis loop of the selected material, which is loaded from the database when selecting a material in the input window. With the waveform of the magnetic field in the core, $H_{core}(t)$, as input, the corresponding flux density waveform, $B_{core}(t)$ and the resulting hysteresis loop are determined by the Preisach model. The waveform of the magnetic field is derived from the current waveform, $i(t)$. Equation (6.14) gives

$$L = \frac{N\Phi}{i} = \frac{NB_{core}A_{core}}{i} = \frac{N\mu_0\mu_{core}H_{core}A_{core}}{i} \tag{6.21}$$

and the magnetic field becomes

$$H_{core}(t) = \frac{L}{\mu_0\mu_{core}A_{core}N}i(t) \tag{6.22}$$

Because the material is assumed to be linear in the range of $H_{core}(t)$ all parameters but $i(t)$, taken from the indata, are constants determined in earlier steps.

The equation for calculating the total average core loss over one cycle per unit volume is taken from (3.57). Multiplication with the core volume, V_{core}, gives

$$P_{core} = V_{core}\left(f\,A_{hyst} + k_{ec}\,\frac{1}{T}\int_0^T\left(\frac{dB_{core}}{dt}\right)^2 dt + k_a\,\frac{1}{T}\int_0^T\left|\frac{dB_{core}}{dt}\right|^{3/2} dt \right) \quad (6.23)$$

where A_{hyst} is the area enclosed by the modelled hysteresis loop which together with the fundamental frequency, $f = 1/T$, determines the hysteresis loss. The derivative of the flux density waveform is derived for use in the calculation of eddy current and anomalous losses. The coefficients k_{ec} and k_a are loaded from the database and depends on the selected material (k_{ec} and k_a for the used iron powder materials are found in Table B.1 in Appendix B).

If a laminated material is selected, the air gap loss of the core, Chapter 3.4, also have to be calculated, by (3.59),

$$P_{gap} = K_{gap}\,\frac{n_{gap}\,l_{gap}\,w}{\rho_{core}}\,f\,B_{peak}^2 \quad (6.24)$$

where K_{gap} is the gap loss constant (Table 3.4), w the width of the laminate and ρ_{core} the resistivity of the core material.

The resistive loss of the winding is calculated for each frequency component of the current, $I_{rms}(n)$, separately, with $R_{ac}(n)$ the total ac resistance of the strands in the winding at the different frequency components

$$P_w(n) = R_{ac}(n)\,I_{rms}^2(n) \quad (6.25)$$

The ac resistance of the winding is calculated layer for layer at each frequency component. The ac resistance of layer m in a winding composed of solid round conductors is (4.11)

$$R_{ac_m} = R_{dc_m}\,\frac{\gamma}{2}\left[r_{skin} - 2\pi\eta^2(2m-1)^2\,r_{prox}\right] \quad (6.26)$$

where

$$\gamma = \frac{d_{Cu}}{\sqrt{2}\,\delta} \tag{6.27}$$

and the porosity factor

$$\eta = \frac{d_{Cu}}{d_{cond}}\sqrt{\frac{\pi}{4}} \tag{6.28}$$

r_{skin} and r_{prox} is calculated by (4.8) respectively (4.9) and the dc resistance of layer m is, according to (4.2), given by

$$R_{dc_m} = \frac{\rho_{Cu} N_{in\,layer}(m) l_T(m)}{A_{Cu}} \tag{6.29}$$

with $l_T(m)$ the length of a strand in one turn. In a toroid $N_{in\ layer}$ differs on the outside and the inside of the core, as determined in *Step 5*. Of course, the total number of strands are the same on the outside and on the inside, $\Sigma N_{in\ layer\_out} = \Sigma N_{in\ layer\_in}$, but the number of layers are higher on the inside, $N_{layer\_in} > N_{layer\_out}$, and hence the average length of a strand on the 'inside-half' is greater, the approximation made of the winding is seen in Figure 6.8. Because of this difference the ac resistance of the 'inside-half' is higher than the one of the 'outside-half'. The ac resistance of the two halves is calculated separately by summing the resistances of each layer on the inside respectively on the outside. The total ac resistance, R_{ac} in (6.25), is determined by the average of these two sums.

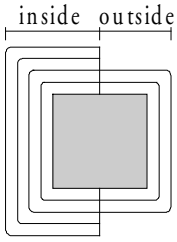

Figure 6.8: A cross-sectional view of the inductor with the winding split in an 'inside-' and an 'outside-half' for calculating the ac resistance.

Finally, the total power loss in the winding is determined by summing the loss calculated by (6.25) for each frequency component.

$$P_{wind} = \sum_{n} P_w(n) \tag{6.30}$$

Step 6. Temperature
Calculation on thermal heating and the resulting temperature of the inductor is treated in Chapter 5, and the derived expression is used in the program. The main equation for calculating the steady-state temperature of the surface, T_{surf}, is (5.12)

$$\frac{P_{core} + P_{wind}}{A_{surf}} = 1.32 \frac{(T_{surf} - T_{amb})^{5/4}}{L^{1/4}} + \sigma\varepsilon(T_{surf}^4 - T_{amb}^4) \tag{6.31}$$

This equation determines the equilibrium between heat generated by the losses and the heat transferred from the inductor by convection and radiation. A_{surf} is the total surface area of the inductor, in the case of the toroid A_{surf} is the surface area of the winding and the difference in thickness of the winding on the inside and on the outside is taken into consideration. This is also taken into consideration when calculating the characteristic length L (Figure 5.2), the average between L on the inside and on the outside is taken. The radiation is determined by the emissivity, ε, of the surface. The ambient temperature, T_{amb}, is specified in the input window. In the program, T_{surf} is found by calculating p_{diff} = (right hand side) – (left hand side) of (6.31) and find the zero of p_{diff} (by the MATLAB function *fzero*).

As stated in Chapter 5 the additional temperature rise in the interior of a power inductor is most often negligible compared to the temperature rise of the surface. Therefore only the temperature rise of the surface is calculated in the design procedure.

6.3 Optimisation

When the six steps of the design procedure are completed for a set of parameters the behaviour of the inductor defined by the parameter set is known and a check is made to see if the optimum design is found. The optimum is found for the set of parameters that within the constraints gives the minimum object function.

The object functions, $f(\mathbf{x})$, possible to select in the program are minimum weight and minimum cost, $\mathbf{x}$ is a vector with the set of parameters defining the design (for the toroid $\mathbf{x} = [D_i, D_o, d, l_{gap}, J_{rms}]$).

$$\begin{aligned} &\text{weight}: \quad f(\mathbf{x}) = m_{core} + m_{wind} \\ &\text{cost}: \quad f(\mathbf{x}) = c_{core} m_{core} + c_{wind} m_{wind} + c_{loss}(P_{core} + P_{wind}) \end{aligned} \tag{6.32}$$

c_{core} and c_{wind} is the cost, in per unit, of the core and the winding material respectively. The cost of iron powder and laminated materials in the core are assumed to be the same. c_{loss} is the cost per watt dissipated in the losses during the lifetime of the inductor. c_{loss} is calculated under the assumptions that a lifetime of 30 years correspond to full operation for 10 years, with a energy price of 0.50 SEK / kWh. This gives a cost of $c_{loss} \approx 50$ SEK / W. The different costs for use in (6.32) is seen in Table 6.1.

	SEK	per unit
c_{core}	10 SEK / kg	1.0
c_{wind}	25 SEK / kg	2.5
c_{loss}	50 SEK / W	5.0

Table 6.1: Costs for use in (6.32).

There are also constraints that restrict the design within an allowed region. The temperature of the surface, T_{surf}, is restricted to not exceed the maximum allowed temperature, T_{max}, specified in the input window. Also a constraint can be set on the flux density, to restrict B to a maximum value B_{max}, e.g. in order to not allow saturation of the core material. These constraints are equality constraints, i.e. $g_i(\mathbf{x}) \le 0$,

$$\begin{aligned} &g_1(\mathbf{x}) = T_{surf} - T_{\max} \\ &g_2(\mathbf{x}) = B - B_{\max} \qquad \text{(optional)} \end{aligned} \tag{6.33}$$

The design program uses the most simple optimisation routine. The properties of a number of different inductors defined by different parameter sets are calculated. The different parameter sets covers a region of core sizes and the parameter set that gives the smallest object function, within the constraints, is taken as the optimal set inside the region. An advantage of this search strategy is that the minimum found is the global minimum of the investigated region, there is no risk to get stuck at a local minimum. The main drawback is

that it is a highly time consuming strategy. The parameters in the set are varied in steps, small steps give higher accuracy and large steps reduce the computing time, i.e. a compromise between accuracy and computing time must be undertaken.

6.4 Magnetic properties of the inductor

When the design is completed and the optimal solution is found the effective permeability, μ_{eff}, of the design is calculated. If the total core, including the air gap, is substituted by a uniform core without gap, with the same physical size as the total core the permeability of this new core that gives the same inductance is defined as the effective permeability.

The inductance of the inductor with the original core is expressed by (6.15) and together with (6.10) it is written as

$$L = \frac{\mu_0 N^2}{n_{gap}\dfrac{l_{gap}}{A_{gap}} + \dfrac{l_{core}}{\mu_{core} A_{core}}} \tag{6.34}$$

The inductance of the inductor with the uniform core is written in terms of effective parameters

$$L_{eff} = \frac{N^2}{R_{eff}} = \frac{\mu_0 \mu_{eff} A_{eff} N^2}{l_{eff}} \tag{6.35}$$

The effective length is

$$l_{eff} = n_{gap} l_{gap} + l_{core} \tag{6.36}$$

and the effective area is

$$A_{eff} = A_{core} \tag{6.37}$$

Now (6.35) is re-written as

$$L_{eff} = \frac{\mu_0 \mu_{eff} A_{core} N^2}{n_{gap} l_{gap} + l_{core}} \tag{6.38}$$

With $L = L_{eff}$ the effective permeability becomes

$$\mu_{eff} = \frac{n_{gap} l_{gap} + l_{core}}{n_{gap} l_{gap} \frac{A_{core}}{A_{gap}} + \frac{l_{core}}{\mu_{core}}} \tag{6.39}$$

By introducing an air gap in the magnetic path the effects of the non-linear characteristics of the core is reduced. The presence of an air gap in (6.34) reduces effects due to variations in the core permeability with changes in flux density. This results in a more constant inductance at an alternating flux density.

In a gapped inductor most of the energy is stored in the air gap. By increasing the air gap length the core length can be reduced with maintained energy storage capability, i.e. the insertion of an air gap reduces the volume of the core in an inductor with given electrical parameters, L and I. In an iron powder material the air gap is distributed due to the insulation between particles, an increase in insulation increases the total air gap and thereby reduces the effective permeability. The magnetic energy possible to store in the inductor is

$$W = \frac{1}{2} LI^2 = \frac{1}{2} BHV_{core} = \frac{1}{2} \frac{B^2}{\mu_0 \mu_{eff}} V_{core} \tag{6.40}$$

thereby

$$V_{core} = \mu_{eff} \frac{\mu_0 LI^2}{B^2} \tag{6.41}$$

If B is kept constant using a core circuit with lower effective permeability, e.g. by inserting an air gap in the magnetic path, may reduce the volume of the core. However by inserting an air gap the total reluctance of the circuit increases and to keep the inductance constant the number of turns must be increased (6.15), hence the winding volume increases. Consequently, a lower effective permeability allows a decrease in the core volume but at the same time the winding volume must be increased. Of course, the total core respectively winding losses follows the changes in volume, i.e. by changing μ_{eff} the origin of the losses can be controlled to some extent.

Chapter 7

Measurement system

A resonant method for measuring the inductance and total loss of an inductor is suggested (Skarrie, 2000). The measurement system is making use of the damped oscillation arise at resonance frequency when a known capacitor is discharged over the 'unknown' inductor. A similar system is used in (Ferreira, 1989) for determining the ac resistance of inductor coils.

7.1 The measurement principle

When a charged capacitor is connected to an inductor an oscillation arises at the resonance frequency of the *LC*-circuit. If no energy is supplied to the circuit the oscillation decays due to losses in the circuit. The losses are modelled as a resistance in the circuit and the *LC*-circuit becomes an *RLC*-circuit. By measuring this decaying oscillation the inductance and the series resistance of the inductor are determined. When knowing the series resistance and the current in the circuit the total loss of the inductor can be determined.

The equivalent circuit of an inductor with inductance L (and reactance X_L) is seen in Figure 7.1 a, with the resistances R_w and R_c representing the winding loss respectively the core loss. Stray capacitance and leakage inductance is disregarded. The impedance of the equivalent circuit is

$$Z = R_w + \frac{R_c X_L^2}{R_c^2 + X_L^2} + j\frac{R_c^2 X_L}{R_c^2 + X_L^2} \tag{7.1}$$

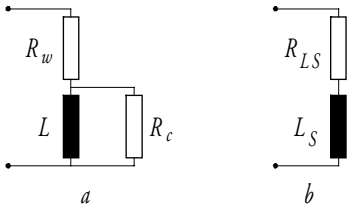

Figure 7.1: Equivalent circuits of an inductor.

Alternatively the equivalent circuit of the inductor is modelled as a series inductance L_S (reactance X_{LS}) and a series resistance R_{LS}, Figure 7.1 b. The impedance of the series equivalent circuit is

$$Z_S = R_{LS} + jX_{LS} \tag{7.2}$$

With $Z = Z_S$ the series resistance and series reactance expressed in resistances R_w and R_c and reactance X_L (= ωL) becomes

$$R_{LS} = R_w + R_c' = R_w + \frac{R_c X_L^2}{R_c^2 + X_L^2} \tag{7.3}$$

$$X_{LS} = \omega L_S = \frac{R_c^2 X_L}{R_c^2 + X_L^2} \tag{7.4}$$

where R'_c is the parallel core loss resistance, R_c, re-calculated to a resistance in series with the winding resistance.

An equivalent circuit of the measurement system is seen in Figure 7.2. The system consists of a charging unit, the capacitor, a thyristor module and the

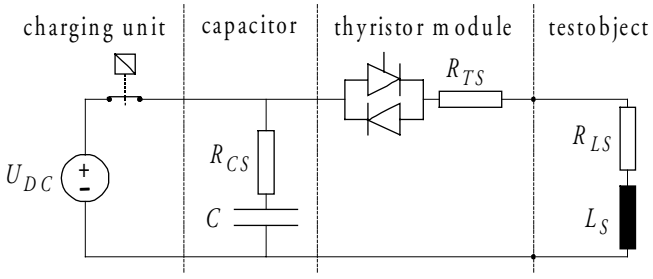

Figure 7.2: Equivalent circuit of the measurement system.

inductor under test. The charging unit is composed of a dc voltage source and a breaker to connect the voltage source for charging the capacitor. For connecting the capacitor to the inductor the thyristor module is used, it consists of a thyristor and an anti-parallel diode. To be able to derive the inductance and the resistance of the inductor from a measurement the capacitor must be known, capacitance C and equivalent series resistance R_{CS}, and also the equivalent series resistance of the thyristor module R_{TS}. During a measurement the current in the circuit together with the voltage over the capacitor respectively the inductor are measured. There is also a pick-up coil wound on the inductor for determining the flux density in the core.

A measurement begins with charging of the capacitor to a specified voltage. When the voltage level is reached the charging unit is disconnected and instead the capacitor is connected to the inductor by the thyristor module. The capacitor and the inductor are forming a series *RLC*-circuit, where the resistance is composed of all the series resistances of components included in the circuit. The total series resistance R_S consists of the equivalent series resistance of the capacitor, the inductor and the thyristor module

$$R_S = R_{CS} + R_{LS} + R_{TS} \tag{7.5}$$

A second-order differential equation representing the current in the *RLC*-circuit is described by

$$\frac{d^2 i}{dt^2} + \frac{R_S}{L_S}\frac{di}{dt} + \frac{1}{L_S C} i = 0 \tag{7.6}$$

With an initial voltage V_{C0} on the capacitor the solution to the differential equation becomes

$$i(t) = \frac{V_{C0}}{\omega_0 L_S} e^{-\alpha t} \sin \omega_0 t \tag{7.7}$$

where α is the damping of the oscillation and ω_0 the angular velocity at the oscillation frequency f_0

$$\alpha = \frac{R_S}{2L_S} \tag{7.8}$$

$$\omega_0 = 2\pi f_0 = \sqrt{\frac{1}{L_S C} - \left(\frac{R_S}{2L_S}\right)^2} = \sqrt{\frac{1}{L_S C} - \alpha^2} \tag{7.9}$$

With the capacitance known and by determining the damping and the frequency from the measurement the series inductance and the total series resistance can be calculated by

$$L_S = \frac{1}{C(\omega_0^2 + \alpha^2)} \tag{7.10}$$

$$R_S = 2L_S\alpha \tag{7.11}$$

The inductance is approximately constant during a measurement, unless saturation is reached. A constant inductance gives an almost constant frequency, thus the winding resistance R_w is about constant. The core resistance R_c on the other hand depends on the flux density in the core, which decays during a measurement. Owing to this the losses can be determined at different flux densities in one measurement. To use an approximately constant flux density the damping is calculated in the interval between to consecutive peaks of the current, Figure 7.3. The average flux density in the interval is taken as the flux density related to the core losses.

The peak values of the current in t_1 and t_2 of Figure 7.3 coincide with the exponential function describing the damping in the interval. Hence the current at t_1 and t_2 is

$$\begin{aligned} i_1 &= I_0 e^{-\alpha t_1} \\ i_2 &= I_0 e^{-\alpha t_2} \end{aligned} \tag{7.12}$$

The damping is calculated as

$$\alpha = \frac{\ln i_1 - \ln i_2}{t_1 - t_2} \tag{7.13}$$

and the frequency as

$$f_0 = \frac{1}{t_2 - t_1} \tag{7.14}$$

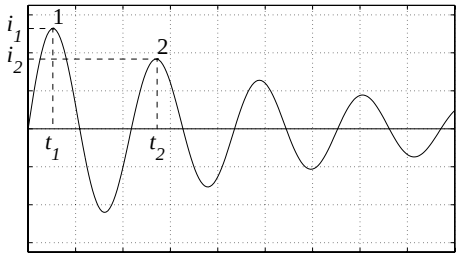

Figure 7.3: Interval for determining the inductor parameters.

If the total series resistance is determined by (7.11) the series resistance of the inductor is determined by subtracting the internal resistances of the capacitor and the thyristor module

$$R_{LS} = R_S - R_{CS} - R_{TS} \tag{7.15}$$

A good estimation of R_{LS} requires a good knowledge of the series resistances of the capacitor and the thyristor module (Chapter 7.2). These resistances shall be kept as small as possible to minimise its impact on the measurements and improve the accuracy.

When R_{LS} is determined the total average loss of the inductor in the interval is

$$P_L = \frac{1}{t_2 - t_1} \int_{t_1}^{t_2} R_{LS} i^2(t)\, dt \tag{7.16}$$

To be able to separate the total loss into winding and core loss R_{LS} should be divided into R_w and R'_c, this is however not possible without first determine the winding resistance. The winding resistance can be determined by a similar winding wound on a non-magnetic core where the whole loss is associated with the winding. The absence of the magnetic core will however to some extent affect the proximity loss part of the winding loss. Further more the inductance of the circuit decreases and thus the frequency increases, i.e. the winding resistance found is determined at a higher frequency. However if the resistance is close to the dc resistance the error in the resistance estimation due to the increased frequency is small.

With R_w known R'_c can be determined, then the winding loss is calculated by

$$P_w = \frac{1}{t_2 - t_1} \int_{t_1}^{t_2} R_w i^2(t)\, dt \tag{7.17}$$

and the core loss by

$$P_c = \frac{1}{t_2 - t_1} \int_{t_1}^{t_2} R'_c i^2(t)\, dt \tag{7.18}$$

The remaining parameters of the equivalent circuit in Figure 7.1 a, besides the winding resistance R_w, can be derived from (7.3) and (7.4). The parallel core loss resistance R_c respectively the true reactance X_L and inductance L becomes

$$R_c = \frac{X_{LS}^2 + R'^2_c}{R'_c} \tag{7.19}$$

$$X_L = \frac{X_{LS}^2 + R'^2_c}{X_{LS}} \tag{7.20}$$

$$L = \frac{X_L}{\omega} \tag{7.21}$$

In most cases $R'^2_c << X_{LS}^2$, then (7.19) and (7.20) approximately becomes

$$R_c \approx \frac{X_{LS}^2}{R'_c} \tag{7.22}$$

$$X_L \approx X_{LS} \tag{7.23}$$

This implies that the true inductance of the tested inductor in most cases can be assumed to be the same as the series inductance determined from measurements by (7.10).

As stated above the inductor parameters can be determined at different flux densities during one measurement. To investigate the frequency dependence of the parameters different capacitances is used in the circuit to vary the resonance frequency.

7.2 Discussion about the measurement system

The main advantage of the measurement system is that an error in the phase angle between measured voltages and current is not affecting the results. The ratio between the reactance and resistance of an inductor is called the inductor quality factor and is defined as

$$Q = \frac{X_{LS}}{R_{LS}} = \frac{\omega L_S}{R_w + R_c'} \tag{7.24}$$

with notations from Figure 7.1. By multiplying the numerator and denominator with I^2 (7.24) becomes

$$Q = \frac{\omega L_S I^2}{R_w I^2 + R_c' I^2} = \frac{2\omega(\text{average stored energy})}{\text{winding loss} + \text{core loss}} \tag{7.25}$$

In most inductors little loss is associated with the inductance, i.e. Q is high. When Q is high the phase angle φ is close to 90° and $\cos\varphi$ is close to zero. When φ is used in the power loss calculations a small error in the angle, e.g. due to difference in timing in the measurements, may introduce considerable error in the calculations.

In the measurement system suggested here only the damping of the signals are used for calculating the losses, a possible error in the phase angle is of no importance.

Another advantage is that thermal heating does not have to be considered. Because a measurement is very fast (< 1 s) no heating appears.

A difficulty with the system is that the accuracy in the determination of the inductor resistance is dependent on the accuracy in the knowledge of remaining equivalent resistances in the circuit. For example the equivalent resistance of the thyristor/diode module that connects the capacitor to the inductor under test is not known with any high accuracy. In addition to that the module has a forward voltage that affects the measurements to some extent. If the equivalent resistances of the measurement circuit can be reduced compared to the inductor resistance a possible inaccuracy becomes of less importance. A possibility to do this is to exchange the thyristor module by a contactor with very small contact resistance. However the contactor must be almost free from bounces otherwise a great part of the energy aimed for oscillation is wasted during bouncing.

7.3 Realisation of the system

The capacitance in the circuit is composed of a number of capacitors, that can be connected in series, parallel or a combination to vary the resonance frequency of the circuit. The capacitors used are metallized polypropylene capacitors PHU 484 from RIFA specially designed for low series resistance. The datasheet properties are

$$C = 47\ \mu\text{F}$$

$$R_{CS} = \frac{\tan\delta}{2\pi f C} \tag{7.26}$$

with $\tan\delta \le 2\cdot 10^{-4} + K_d f \cdot 10^{-9}$ and the dissipation factor $K_d = 740$. The total series resistance depends on how the capacitors are connected, in series, parallel or a combination. The total capacitance respectively series resistance is

$$C_{tot} = \frac{n_{par}}{n_{ser}} C \tag{7.27}$$

$$R_{CS_{tot}} = \frac{n_{ser}}{n_{par}} R_{CS} \tag{7.28}$$

The thyristor/diode module that connects the capacitor and the inductor is a SKKH 162 from SEMIKRON. After the thyristor is triggered the trigger pulse is high until the measurement is completed. Half a period the thyristor is in the on state and for the other half the diode is in the on state. The mean on state power dissipation is for a sinewave (the same in both the thyristor and the diode)

$$P_{av} = \frac{2V_F}{\pi}\hat{I} + \frac{r_T}{2}\hat{I}^2 = R_{TS}\frac{\hat{I}^2}{2} \tag{7.29}$$

This gives the series resistance

$$R_{TS} = \frac{4}{\pi}\frac{V_F}{\hat{I}} + r_T \tag{7.30}$$

where the forward voltage V_F = 0.85 V and the on state slope resistance r_T = 1.5 mΩ.

LabVIEW® supervises the measurement procedure. The initial voltage level on the capacitor is controlled by a dc source, when the level is reached LabVIEW® disconnects the dc source and sends a pulse that keeps the thyristor module triggered during the measurement. LabVIEW® also handles the acquisition of measurement data, the voltage over the capacitor respectively the inductor, the current in the circuit and the electromotive force induced in the pick-up coil. When the data acquisition is completed the calculations of the inductor parameters and the losses described in Chapter 7.1 is performed in MATLAB®.

Chapter 8

Application

The developed design program described in Chapter 6 is used to design the line filter inductors of a three phase on-board battery charger for charging of electrical vehicles (Heckford, 2000). Two designs with different core material are carried out. This chapter describes the application and defines the design specifications and restrictions. The calculated properties of the resulting inductor designs are also presented.

8.1 Battery charger for electric vehicles

The on-board battery charger is based on a self commutated converter topology, composed of Pulse Width Modulated (PWM) Voltage Source Converters (VSC) based on IGBTs, with the possibility of using bi-directional power flow. A circuit diagram of the charger is illustrated in Figure 8.1.

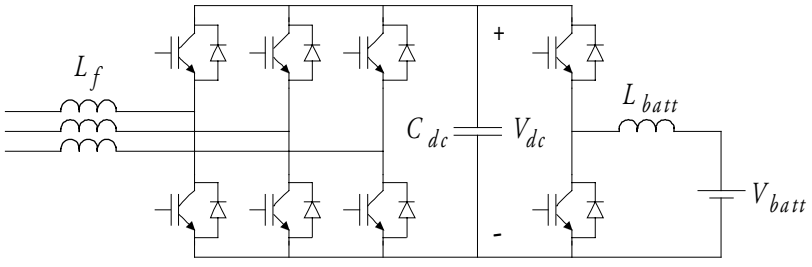

Figure 8.1: The battery charger.

On the line side the charger consists of a three phase PWM VSC. In the interface between the charger and the grid the line side filter inductors, L_f, attenuates current harmonics raised by the PWM of the converters. On the battery side a two quadrant dc-dc converter is used. The battery side contains a smoothing inductor, L_{batt}, for reducing the ripple in the dc current.

Specification

The specification of the charger is listed in Table 8.1. PWM based on a triangular carrier wave is used, which implies a fixed switching frequency.

Rated power	S_n	10 kVA
Grid voltage	V_n	400 V
Grid frequency	f_1	50 Hz
Dc-link voltage	V_{dc}	650 V
Switching frequency	f_{sw}	5 kHz
Distortion index	DIN	< 3%

Table 8.1: Specification of the three phase on-board battery charger.

The part of the charger treated in this thesis is the line side filter inductors, L_f, in Figure 8.1. The filter inductors of a power electronic converter are most often heavy and bulky and represent a large part of the total weight. In this case the charger will be on-board the vehicle, i.e. size and weight are crucial. Hence, minimising the weight of the inductors is important in keeping the total weight of the battery charger low.

The inductance of the filter inductors is chosen in order to keep the harmonic content of the phase currents below a certain level.

The harmonic content of the current can be quantified either by the total harmonic distortion, THD, or the distortion index, DIN. The total harmonic distortion is defined by

$$\mathrm{THD} = \frac{1}{I_1}\sqrt{\sum_{h=2}^{\infty} I_h^2} \tag{8.1}$$

with the current at the fundamental frequency, I_1, and h the harmonic order. The definition of the distortion index includes the rms value of the total current, I_{rms},

$$\mathrm{DIN} = \frac{1}{I_{rms}} \sqrt{\sum_{h=2}^{\infty} I_h^2} \tag{8.2}$$

For a low distortion level the two definitions result in equal value. In this case the harmonic content of the battery charger is specified according to the distortion index, the harmonic content should fulfil DIN < 3%, Table 8.1.

Line filter inductor specification

The battery charger is simulated in SIMULINK with data according to the specifications. The waveform of one of the phase voltages from the simulation is seen in Figure 8.2 together with its normalised frequency spectrum. The spectrum indicates that the phase voltage consists of the fundamental frequency component together with components in bands close to the switching frequency, f_{sw} = 5 kHz, and multiples of f_{sw}.

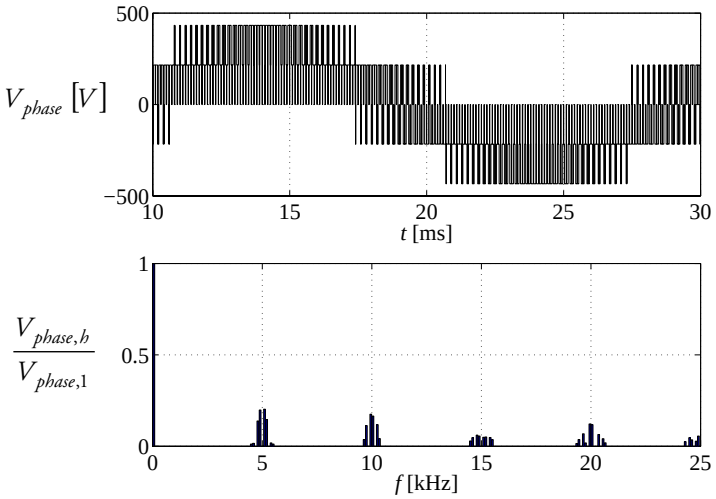

Figure 8.2: The waveform of a phase voltage and the corresponding normalised frequency spectrum.

The frequency components of the corresponding phase current are calculated by

$$I_{phase,h} = \frac{1}{\omega_1 L} \cdot \frac{V_{phase,h}}{h} \tag{8.3}$$

where L is chosen in order to fulfil the specification of DIN < 3%. The harmonics of the phase current is seen in the frequency spectrum in Figure 8.3, where also the resulting phase current waveform is included.

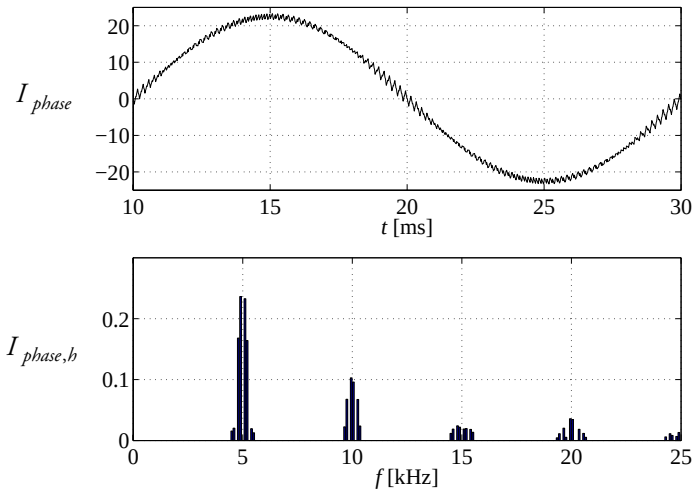

Figure 8.3: The waveform of a phase current and the corresponding frequency spectrum.

The distortion index is determined at a phase current I_{phase} = 16 A rms. To obtain DIN < 3% the inductance L = 6.6 mH is chosen, which gives DIN = 2.8% and THD = 2.7%.

8.2 Design of the inductor

When a suitable inductance is selected and the harmonic content of the current associated with the inductance is determined from simulations, the design process follows. The first step is to feed the inductor design program with all data needed for computation.

Input of necessary data

All data necessary in subsequent calculations are fed into the program at the input window, as described in Chapter 6.1. The core material, core geometry and winding configuration are selected from their respective database.

Furthermore the electrical parameters; inductance and frequency components composing the current, temperatures etc. will be fed into the program.

All data provided for the program for designing the line filter inductors used in the battery charger is put together in Table 8.2.

Core material	Somaloy 500 + 0.6% LB1
Core geometry	toroid
Winding	Round solid
parallel strands	3
Electrical parameters	
inductance	6.6 mH
rms current, fundamental frequency	16 A 50 Hz
rms current, harmonic frequencies	0.16 A 4 800 Hz
	0.24 4 900
	0.23 5 100
	0.16 5 200
	0.07 9 750
	0.10 9 950
	0.10 10 050
	0.07 10 250
Temperature	
ambient	40°C
maximum	120°C
Optimisation criteria	weight

Table 8.2: Data provided for the inductor design program before starting a design optimisation of the battery charger line filter inductor.

Somaloy 500 + 0.6% LB1 is chosen as the core material due to its lower relative permeability compared to Somaloy 500 + 0.5% Kenolube. The lower permeability reduces the core volume and by that the core weight, Chapter 6.4. To reduce the core weight even further an extra air gap is introduced in the magnetic path, in addition to the distributed air gap of the powder material. To maintain the inductance, the number of turns must be increased when the permeability is decreased, thereby increasing the copper weight. Hence, a balance between core and copper weight must be made.

The relatively low bulk permeability compared to laminated materials makes it advantageous to use a toroidal core in order to get an adequate

magnetic shielding. The winding covers the entire surface of the core and thereby forces the main part of the flux to be kept inside the core. This minimises the leakage fields and reduces the disturbance on adjacent components. Though one drawback of the toroid is the difficulty of winding it. The winding must be wound directly on the core in contrast to e.g. a C- or EI-core where the winding is pre-wound on a bobbin that is mounted on the core.

The low fundamental frequency and the small amount of high frequency current harmonics makes a winding composed of a round solid conductor most suitable. The conductor is divided into three parallel strands in order to simplify the winding process. The fill factor is most often not crucial in a toroid because the winding usually does not occupy the entire winding window.

When feeding the electrical parameters into the program only the eight most significant current harmonics are considered. The influence of the remaining harmonics on the design is negligible.

The design

Before starting the design, some extra prerequisites are introduced in the program. In order to get a fairly linear behaviour of the inductor, the maximum flux density allowed in the core is restricted to 1 T, i.e. magnetic saturation is avoided. It is also specified that the air gap should be divided into eight separate gaps evenly distributed in the core in order to reduce each air gap length, hence reducing the fringing of the flux. Furthermore, this distribution also simplifies manufacturing due to the easier produced smaller parts composing the core.

Finally, a design is calculated from the specifications introduced in Table 8.2. The program presents the resulting minimum weight design in an outline, see Figure 8.4 (showing a front and a side plot), together with a listing of calculated data of the inductor, Table 8.3.

Core dimensions		
inner diameter	D_i	90 mm
outer diameter	D_o	140 mm
thickness	d	25 mm
total air gap length	$n_{gap} \cdot l_{gap}$	8·0.9 mm
Winding		
number of turns	N	253
copper area	A_{Cu}	2.0 mm^2
Magnetic properties		
inductance	L	6.6 mH
maximum flux density	B_{max}	1.0 T
effective permeability	μ_{eff}	48
Losses		
hysteresis	P_{hyst}	12 W
eddy current	P_{ec}	0 W
anomalous	P_{anom}	10 W
winding	P_{Cu}	34 W
total	P_{tot}	56 W
Temperature		
maximum	T_{max}	120°C
Weight		
core	m_{core}	1.59 kg
winding	m_{Cu}	1.83 kg

Table 8.3: Calculated specification of the designed minimum weight inductor, with Somaloy 500 + 0.6% LB1 in the core.

The eddy current part of the core losses in Table 8.3 is estimated to zero by the program. The dynamic loss coefficients, eddy current and anomalous loss coefficients, used in the program are determined by loss separation, Chapter 3.4. The loss separation is performed on measurements from a toroidal core with much smaller cross sectional area, where possible geometry dependent eddy currents are small, thus the eddy current loss coefficient becomes zero. However for this larger core, the eddy current loss coefficient is not necessarily still zero due to higher eddy currents possible in the larger cross section. For the inductor based on Somaloy 500 + 0.5% Kenolube, treated later, the

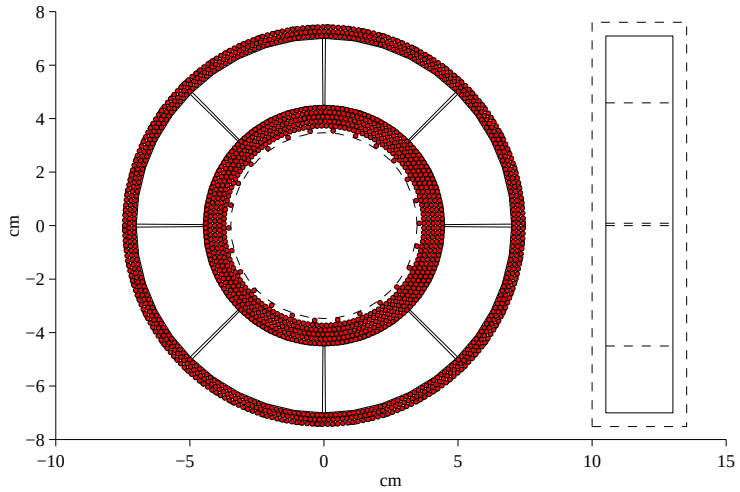

Figure 8.4: Outline of the designed inductor, front and side plot.

geometry dependent eddy currents should be even more apparent due to the smaller amount of insulation between powder particles.

A minimum weight inductor is the aim of this design, owing to that the flux density is maximised in order to minimise the cross sectional area of the core. Furthermore, the surface temperature of the design becomes the maximum allowed when optimising. Because the size of the surface area determines the temperature, a maximised temperature minimises the surface area needed for cooling the inductor. The flux density and the temperature are usually the restricting parameters when designing inductors for use in power applications.

The presence of harmonics in the current is responsible for about 10 W, or 18%, of the total loss of the inductor. As seen in Figure 8.5 the harmonics give rise to minor loops in the hysteresis loop. However, the area enclosed by the minor loops is almost negligible compared to the major loop area, i.e. the hysteresis loss is almost not affected by the harmonics. Instead the small high frequent changes in magnetisation produces eddy currents in the core and thereby increases the dynamic core losses. The harmonics also give rise to a small increase in the winding losses, due to skin and proximity effects.

In the minimum weight design, the core loss is less than the winding loss, see Table 8.3. This relation is favourable in a toroid and improves the thermal behaviour. Because the winding covers the entire core the core losses must be

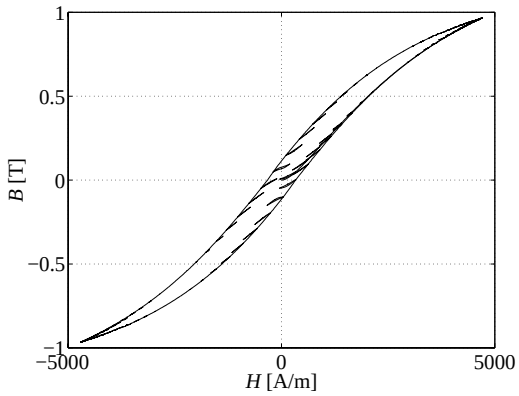

Figure 8.5: Hysteresis loop produced by the current specified in Table 8.2. The harmonics give rise to minor loops.

transferred first to the winding and then further on to the air, while the winding losses is transferred directly to the air. Hence, losses produced in the winding are more easily transferred from the inductor.

To compare the two iron powder materials investigated in this thesis, Somaloy 500 + 0.6% LB1 and Somaloy 500 + 0.5% Kenolube, calculations are made also on an inductor including the latter material. This second inductor is made with exactly the same core geometry and winding configuration as the first one but thus with the difference in core material. A listing of the resulting calculated data of this inductor is seen in Table 8.4. Due to the higher relative permeability the inductance, the maximum flux density and the effective permeability increases. The core loss, on the other hand, decrease due to the lower loss per unit volume at low frequencies in the Kenolube-material. The reason for the reduced loss per unit volume is the more intense heat treatment exposed to the material, which reduces low frequency loss, hysteresis loss, but increases high frequency losses, eddy current loss. As a consequence of the reduction in losses the maximum temperature of the inductor is also reduced. The more intense heat treatment also enhances the density compared to the LB1-material, which results in a slightly heavier core.

Core dimensions		
inner diameter	D_i	90 mm
outer diameter	D_o	140 mm
thickness	d	25 mm
total air gap length	$n_{gap} \cdot l_{gap}$	8·0.9 mm
Winding		
number of turns	N	253
copper area	A_{Cu}	2.0 mm^2
Magnetic properties		
inductance	L	7.5 mH
maximum flux density	B_{max}	1.1 T
effective permeability	μ_{eff}	54
Losses		
hysteresis	P_{hyst}	10 W
eddy current	P_{ec}	0 W
anomalous	P_{anom}	5 W
winding	P_{Cu}	34 W
total	P_{tot}	49 W
Temperature		
maximum	T_{max}	110°C
Weight		
core	m_{core}	1.64 kg
winding	m_{Cu}	1.83 kg

Table 8.4: Specification of the designed inductor, with Somaloy 500 + 0.5% Kenolube in the core.

As a rough comparison approximate calculations are also performed on a laminated steel sheet core. To make the comparison easy a similar core geometry with the same dimensions as the one used in the powder cores is investigated. Also the winding configuration is similar with the same number of turns. In order to maintain the specified inductance the total air gap length must be increased due to the higher permeability of the laminated material, the effective permeability should not be altered. The material used is manufactured by Surahammars Bruk AB, Sweden, (Surahammars Bruk AB, 1998), grade CK40 with a laminate thickness of 0.5 mm. The resulting figures are presented

in Table 8.5. In this inductor the major part of the core losses is associated with the harmonics due to eddy currents generated in the thick laminations. The use of a similar winding as in the powder cores gives no change in the winding losses. The weight of this laminated core exceeds the weight of the powder core due to higher density. However, the laminated core is far from the maximum temperature, i.e. the core size, and thus the weight, can be reduced to some extent before reaching the limiting temperature.

Core dimensions		
inner diameter	D_i	90 mm
outer diameter	D_o	140 mm
thickness	d	25 mm
total air gap length	$n_{gap} \cdot l_{gap}$	8·1.3 mm
Winding		
number of turns	N	253
copper area	A_{Cu}	2.0 mm^2
Magnetic properties		
inductance	L	6.6 mH
maximum flux density	B_{max}	1.0 T
effective permeability	μ_{eff}	48
Losses		
core	P_{core}	8 W
winding	P_{Cu}	34 W
total	P_{tot}	42 W
Temperature		
maximum	T_{max}	100°C
Weight		
core	m_{core}	1.70 kg
winding	m_{Cu}	1.83 kg

Table 8.5: Specification of approximate calculations on an inductor with laminated steel sheet core, laminate thickness 0.5 mm, grade CK40 by Surahammars Bruk AB.

8.3 Manufacturing of the inductors

The two inductors described in Table 8.3 and 8.4 are manufactured. The cores are composed of eight parts separated with air gaps, Figure 8.4. These parts are tooled from bulk material cylinders with diameter 100 mm and height 115 mm. The parts are joined together with an air gap of 0.9 mm (the accuracy is within 0.005 mm) between each part. Linlan Permedyn AB provides the tooling and assembling of the cores. A picture of the finished cores is seen in Figure 8.6.

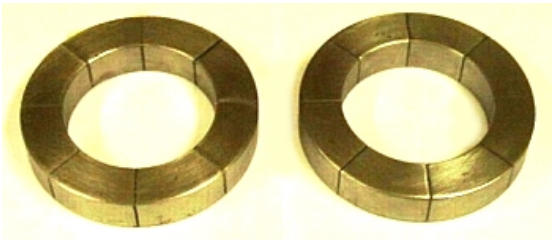

Figure 8.6: The manufactured cores, one with Somaloy 500 + 0.5% Kenolube and one with Somaloy 500 + 0.6% LB1.

The winding consist, as stated earlier, of three parallel strands. To be able to measure the flux density in the core, four separate pick-up coils with twenty turns each, are first wound on the core. On top of the pick-up coils the three strands constituting the main winding are wound together in a bundle. A layer of insulating film is wounded directly on the core within the windings and a layer is also wound on top of the windings. The winding is fabricated at Tramo-ETV AB.

Chapter 9

Measurements

The two manufactured inductors (designated LB1 and Kenolube) are tested by the measurement system, described in Chapter 7. From the measurement system the inductor parameters, resistance and inductance can be determined. The measurements and the following calculation of parameters are described in this chapter with references to equations in Chapter 7.

9.1 Inductor parameters

As the capacitance in the measurement circuit four capacitors with the measured value C = 49.3 μF each is used in different arrangements. This gives the possibility to vary the resonance frequency and to determine the inductor parameters at the arisen frequencies. The different capacitor arrangements used and the resulting resonance frequencies when connected to the two tested inductors are seen in Table 9.1.

parallel	**serial**	**capacitance (μF)**	**frequency (Hz)**	
			LB1	**Kenolube**
4	1	197.2	151	140
2	1	98.6	213	197
1	1	49.3	301	279
1	2	24.6	426	397

Table 9.1: The different capacitor arrangements and the resulting resonance frequencies.

Figure 9.1 shows the damped oscillation between four parallel capacitors (C = 197.2 μF) and the inductor under test (Kenolube in this case) of the measurement system. The continuous line represents the current in the circuit and the broken line represents the induced voltage measured by a pick-up coil. From the damped oscillation the inductor parameters, inductance and resistance are determined. The vertical dotted lines show the maximum points of the voltage. The inductance is determined from the frequency of the oscillation while the resistance is determined from the damping. The resistance of the inductor together with the current in the circuit gives the total loss of the inductor. Calculations are made in each interval between two vertical lines, i.e. from one measurement the inductor parameters can be determined at different current and flux density values.

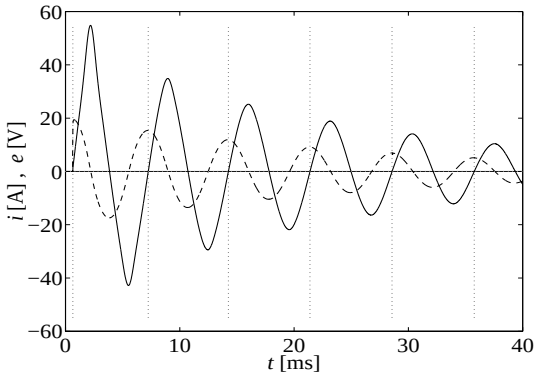

Figure 9.1: An oscillation obtained by the resonant system, continuous line – current, broken line – induced voltage measured by a pick-up coil. The vertical dotted lines shows the maximum points of the voltage, calculations are executed in each interval between these lines.

Inductance

The flux density in the core is calculated from the induced voltage measured by the pick-up coil. The upper plots of Figure 9.2 and 9.3 shows the relation between the current in the inductor and the flux density in the core for respective inductor. The dots in the figures represents measurements, the continuous lines are calculated assuming fringing of the flux at the air gaps and

the broken lines are valid if the fringing is negligible. Note that the dots and the broken line coincide in the figures, especially in 9.2, which makes the broken line a little hard to discern.

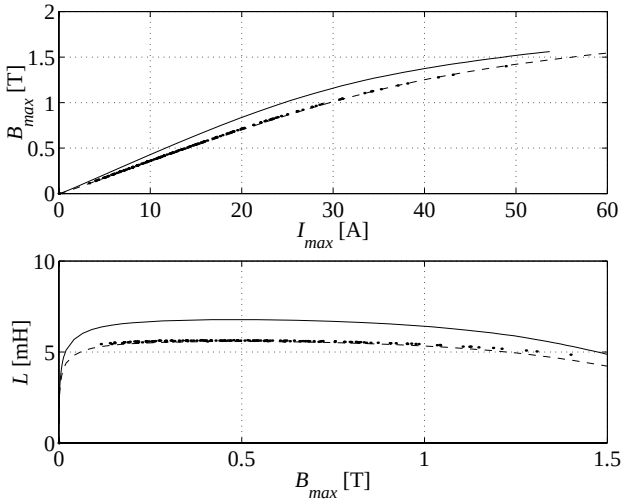

Figure 9.2: $B(I)$ and $L(B)$ for the inductor with core material Somaloy 500 + 0.6% LB1. Measurements (dots) compared to calculations assuming fringing flux (continuous line) and calculations assuming no fringing (broken line).

The lower plots of Figure 9.2 and 9.3 shows the variation of the inductance against the peak flux density at an increase in amplitude of the applied ac field. The resonance frequency is determined from the time interval between two vertical lines in Figure 9.1. From the frequency and by the known capacitance the inductance is calculated by (7.10). In the figure the inductance determined from measurements are represented by the dots, while the continuous line represents calculations considering fringing flux and the broken line calculations without considering fringing. The calculated inductance is determined by

$$L = \frac{\mu_0 N^2}{n_{gap}\dfrac{l_{gap}}{A_{gap}} + \dfrac{l_{core}}{\mu_{core} A_{core}}} \tag{9.1}$$

where the degree of fringing determines the ratio between A_{gap} and A_{core} and μ_{core} is a function of the peak flux density.

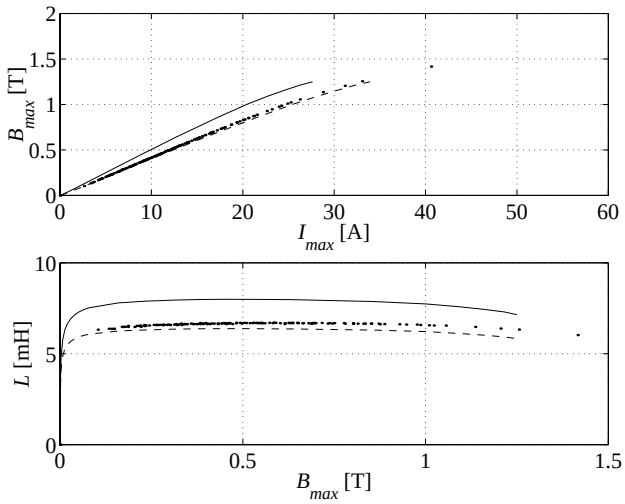

Figure 9.3: $B(I)$ and $L(B)$ for the inductor with core material Somaloy 500 + 0.5% Kenolube. Measurements (dots) compared to calculations assuming fringing flux (continuous line) and calculations assuming no fringing (broken line).

Originally a fringing of the flux at the air gaps was assumed. The fringing increases the effective area at the air gap and thus reducing the reluctance of the magnetic path, i.e. increases the inductance. The effect of the fringing on the reluctance was calculated according to (6.5) – (6.10). The fringing factor in (6.5) is valid if the winding does not surround the air gap. In this case however the winding fully covers the gaps and thereby assisting in keeping the flux inside the core (Lee, et al., 1988). From Figures 9.2 and 9.3 it is obvious that calculating the fringing factor with (6.5) assuming that the winding at the gaps not affects the fringing clearly overestimates the fringing and as a consequence also overestimates the inductance. On the contrary the measured values are close to the broken line calculated under the assumption of no fringing, i.e. the winding at the gaps reduces the fringing almost completely.

The maximum value of the measured inductance of the LB1-inductor is 5.6 mH, Figure 9.2, while the specified inductance was 6.6 mH. As mentioned above the design calculated from specifications assumed fringing, which gives a

maximum inductance of 6.6 mH. Calculation without fringing gives 5.6 mH, which corresponds well with the measured maximum value. For the Kenolube-inductor the maximum inductance considering fringing is 8.0 mH, Figure 9.3. Calculation without considering fringing gives 6.4 mH and from measurements L = 6.6 mH. The higher inductance of the Kenolube-inductor compared to the LB1-inductor is due to the higher permeability of the core material.

Resistance

The damping of the oscillation is calculated by (7.13) in each interval between two vertical lines in Figure 9.1. However, in the measurements referred to in this chapter the damping of the induced voltage is used instead of the current damping as used in Chapter 7. The reason for this is that the expression for determining the damping is only valid for sinusoidal waveforms and the current becomes non-sinusoidal when approaching saturation, as seen in the first periods of Figure 9.1, while the induced voltage still is sinusoidal.

The total resistance of the circuit is calculated by (7.11) and the resistance of the inductor, R_{LS}, is determined by (7.15). The expressions of the equivalent resistances of the capacitor and the thyristor module for use in (7.15) is found in (7.28) respectively (7.30). With R_{LS} in each interval known the total power loss of the inductor is calculated by the resistance and the rms current in the interval (7.16).

R_{LS} is composed of a winding resistance R_w and a series resistance representing the core losses R'_c (7.3). R_w depends on the winding arrangement and the applied frequency while R'_c depends on the core material, the frequency and the flux density. During a measurement the frequency is almost constant due to the fairly constant inductance, i.e. R_w is nearly constant. The flux density on the other hand is decreasing during a measurement, which reduces the parallel core loss resistance R_c, Figure 7.1. A decrease in the parallel resistance R_c gives an increase in the series resistance R'_c (7.22). Consequently R_{LS} increases slightly during a measurement, i.e. the damping is somewhat higher than exponential. Because of this variation in R'_c the inductor resistance R_{LS} must be calculated for each interval to reduce the influence of the flux density damping. The average peak flux density in the interval is taken as the value used in the core loss calculation together with the frequency. Summing the core losses, calculated by (3.59) with parameters from Table 3.4, and the

winding loss, as described by (6.25) – (6.30), gives the calculated value of the total inductor loss.

The total power loss of the two inductors at different currents is determined at the resonance frequencies defined by the different capacitor arrangements listed in Table 9.1. Figure 9.4 and 9.5 shows the power loss as a function of the rms current for Somaloy 500 + 0.6% LB1 respectively Somaloy 500 + 0.5% Kenolube. The measurements (dots) agree fairly well with calculated total loss (continuous line), with an error within 10% for the Kenolube-inductor and within 10% for the LB1-inductor at the lowest frequencies but increasing up to almost 20% at the highest frequency.

At a given current the induced voltage measured by the pick-up coil increases as the frequency increases. A limiting highest allowed value in the voltage measurement circuit is the cause of the reduction in highest possible current as the frequency increases in Figure 9.4 and 9.5.

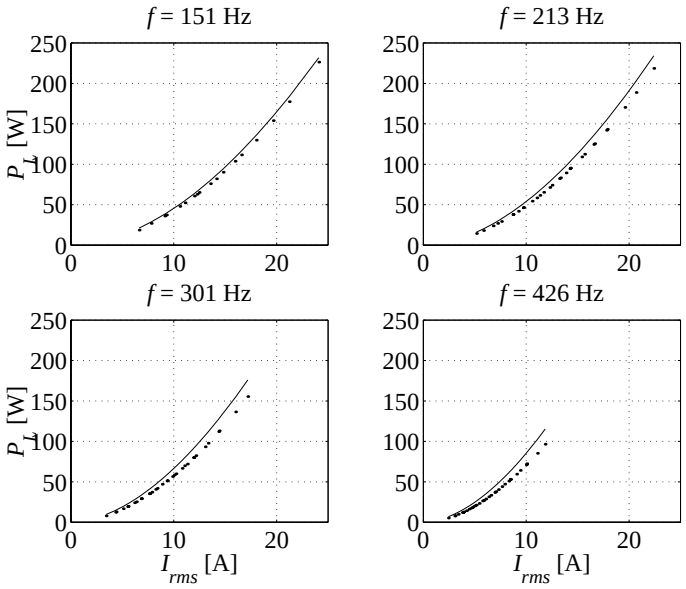

Figure 9.4: The continuous line represents calculated total losses of the inductor with core material Somaloy 500 + 0.6% LB1. Measurements by the resonant system are represented by the dots.

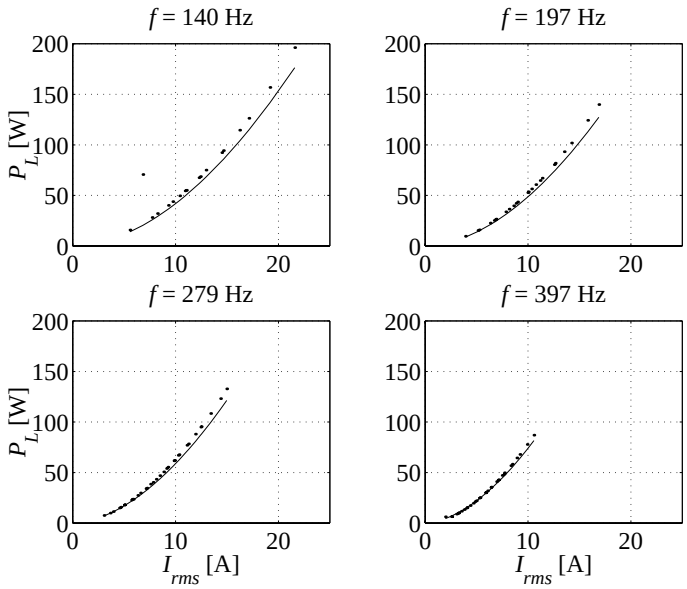

Figure 9.5: The continuous line represents calculated total losses of the inductor with core material Somaloy 500 + 0.5% Kenolube. Measurements by the resonant system are represented by the dots.

At the low frequencies investigated here the Kenolube-inductor shows a lower total loss due to the lower core loss compared to the LB1-inductor. Due to the identical windings of the two inductors the winding loss is the same in both cases. The frequency dependence of the winding losses is almost negligible at these frequencies, thereby the ac resistance of the windings is very close to the dc resistance. The increase in total loss with frequency is almost solely related to the increase in core losses.

9.2 Magnetic measurements

The insertion of air gaps in the magnetic path reduces the effective permeability of the path. It also improves the linearity of the inductor. Figure 9.6 shows the dc hysteresis loop of a ring sample of Somaloy 500 + 0.6% LB1 without gaps in the path, broken line. The dc hysteresis loop of the ready magnetic component including eight gaps of 0.9 mm each is also seen, the

continuous line. The introduction of air gaps cause a shearing of the loop that provides a more linear behaviour and increases the current level possible without saturating the material.

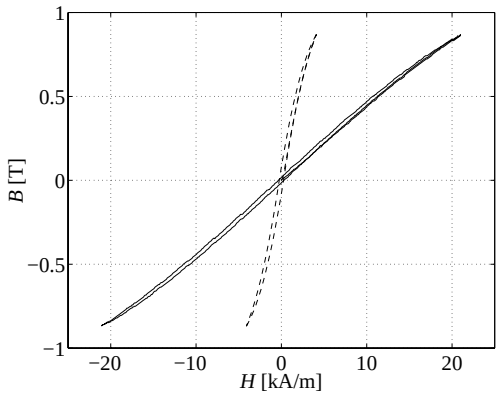

Figure 9.6: Shearing of the dc hysteresis loop of Somaloy 500 + 0.6% LB1 due to insertion of air gaps in the flux path. In a core without air gaps the loop follows the broken line. The used core including eight distributed air gaps of 0.9 mm each is subjected to the loop described by the continuous line.

Chapter 10

Conclusions

In this thesis expressions for calculating core loss, winding loss and thermal heating is derived. These expressions are used together with a design procedure in the implementation of a program for designing inductors. An inductor, with iron powder core, is designed by the program for use as the line side filter of a battery charger for electrical vehicles. The inductor is manufactured with two different core material compositions and the properties calculated by the design program are compared to measurements. This chapter discusses the results from these calculations and measurements. Finally, some suggestions for future work are presented.

10.1 Results

In Chapter 6 the inductor design program is presented. The design procedure used in the program is described in the same chapter with expressions for calculating core loss, winding loss and thermal heating included from Chapter 3, Chapter 4 respectively Chapter 5.

To evaluate the calculations made by the developed program an iron powder inductor is designed for a specified application, as the line side filter inductor of an on-board battery charger for electrical vehicles. The application is described in Chapter 8 with the specification listed in Table 8.1 and 8.2. The inductor is manufactured with two different iron powder core materials, with difference in magnetic and electric behaviour. The calculated properties for the design of the inductor with core material Somaloy 500 + 0.6% LB1 are presented in Table 8.3, while the corresponding properties of the inductor with a core composed of Somaloy 500 + 0.5% Kenolube are specified in Table 8.4.

The designed inductors are manufactured and tested by the measurement system described in Chapter 7. The results from these measurements are discussed and compared to the once predicted by the design program in Chapter 9. In this chapter a summary between some measured and calculated properties are presented, in Table 10.1 for the inductor with the core material Somaloy 500 + 0.6% LB1 and in Table 10.2 for the inductor with the core composed of Somaloy 500 + 0.5% Kenolube.

		measured	**calculated**	**proc. diff. [%]**
I_{rms} **[A]**	f **[Hz]**	**Total loss [W]**		
20	151	159	165	4
	301	—	—	—
15	151	93	97	4
	301	123	138	11
10	151	43	46	7
	301	58	66	12
		Maximum inductance [mH]		
		5.6	5.6	0

Table 10.1: Comparison between some measured and calculated properties of the inductor with the core composed of Somaloy 500 + 0.6% LB1.

		measured	**calculated**	**proc. diff. [%]**
I_{rms} **[A]**	f **[Hz]**	**Total loss [W]**		
20	140	170	154	10
	279	—	—	—
15	140	98	90	9
	279	133	122	9
10	140	45	42	7
	279	63	59	7
		Maximum inductance [mH]		
		6.6	6.4	3

Table 10.2: Comparison between some measured and calculated properties of the inductor with the core composed of Somaloy 500 + 0.5% Kenolube.

The winding loss is about the same for the two inductors, since the resistance is close to dc resistance and the frequency dependence is almost negligible. The difference in loss is instead due to the core losses, where the Kenolube-material is the one with the lowest loss per unit volume at a given flux density. However, the two inductors show about the same amount of loss at a given current. This is due to the higher effective permeability of the Kenolube-core, which results in a higher flux density at the given current, i.e. higher core loss. The inductance is calculated assuming no fringing flux, this assumption is discussed in more detail in Chapter 9.1.

Table 10.1 and 10.2 shows good agreement between calculations, performed by the design program, and measurements, supplied by the resonant measurement system. However the accuracy of the system can be further improved by better knowledge of the equivalent series resistances of the circuit. Some suggested ways to improve this is discussed in Chapter 7.2.

The design of laminated core inductors is not fully developed in the design program. However, approximate calculations on an inductor including a laminated steel sheet core, with thick laminations – 0.5 mm, are performed in Chapter 8. The similar core geometry and winding configuration as for the powder cores is used, but in order to maintain the specified inductance the air gap length is increased. The resulting figures in Table 8.5 shows a reduction in core loss, and thus also in surface temperature, compared to the iron powder toroidal cores. This indicates that for the low frequency application treated here the use of a laminated core will result in a lighter and smaller inductor. However, in a toroidal core the three-dimensional flux paths possible in an iron powder material is not utilised.

10.2 Future Work

Reasonably accurate core loss expressions of iron powder materials based on the physical origin of the losses is of utmost interest for an application designer when using these materials for designing e.g. inductors and electrical machines. The core loss model used in this thesis shows fairly good agreement for the investigated materials. However, some suggestions for future work on these core loss models for iron powder materials are

- further evaluation of the extended Preisach model used for hysteresis loss estimation, Chapter 3.1. Parameter determination and investigation of the agreement with additional materials should be executed.

- investigation of the geometry dependence in the eddy current loss. The behaviour of the geometry dependence in the dynamic losses could be investigated by measurements of the dynamic losses on cores with different material compositions and sizes. Then, based on these measurements, trying to find a physically based loss expression describing the variations due to the amount of insulation, particle size etc. E.g. the expression suggested in Chapter 3.2, including losses originating from both eddy currents in the bulk material and eddy currents in the interior of particles could be investigated.

Regarding the inductor design program the main step in a further development would be

- a more efficient search strategy for the optimisation. This will speed up the design procedure and make it possible to search larger regions in a shorter time.

References

Bartoli, M., Noferi, N., Reatti A., (1995), "Modelling winding losses in high-frequency power inductors", *Journal of Circuits, Systems and Computers*, vol. 5, no. 4, pp. 607-626.

Bartoli, M., Noferi, N., Reatti A., (1996), "Modelling Litz-wire winding losses in high-frequency power inductors", *Proceedings of the Power Electronics Specialists Conference (PESC'96)*, Baveno, Italy, pp. 1690-1696.

Bertotti, G. (1984), "Space time correlation properties of the magnetization process and eddy current losses", *Journal of Applied Physics*, vol. 55, no. 12, pp. 4339-4355.

Bertotti, G. (1985), "Physical interpretation of eddy current losses in ferromagnetic materials", *Journal of Applied Physics*, vol. 57, no. 6, pp. 2110-2126.

Bertotti, G. (1992), "Dynamic generalization of the scalar Preisach model of hysteresis", *IEEE Transactions on Magnetics*, vol. 28, no. 5, pp. 2599-2601.

Bozorth, R. M. (1978), *Ferromagnetism*. IEEE Press, ISBN 0-7803-1032-2.

Chikazumi, S. (1997), *Physics of ferromagnetism*. Oxford ClarendonPress, ISBN 0-19-851776-9.

Ferreira, J. A. (1989), *Electromagnetic modelling of power electronic converters.* Kluwer Academic Publishers, ISBN 0-7923-9034-2.

Ferreira, J. A. (1994), "Improved analytical modeling of conductive losses in magnetic components", *IEEE Transactions on Power Electronics*, vol. 9, no. 1, pp. 127-131.

Gélinas, C., Chagnon, F., Pelletier, S., Lefebvre, L.-P., (1998), "Effect of curing conditions on properties of iron-resin materials for low frequency applications", *Advances in Powder Metallurgy & Particulate Materials*, part 8, 1998.

Heckford, Simon (2000), *Design of an onboard battery charger for an electrical vehicle*, Master Thesis, Department of Industrial Electrical Engineering and Automation, Lund University, Sweden.

Holman, J. P. (1986), *Heat transfer*. Mc Graw-Hill, ISBN 0-07-114320-3.

Höganäs AB (1997), *Somaloy™ 500, Soft Magnetic Composites from Höganäs Metal Powders*, Product Guide, Höganäs AB, Sweden.

Jansson, P. (1998), "Soft magnetic composites – from dc to 1 MHz with iron powder", *1998 Powder Metallurgy World Congress*, Granada, Spain.

Jansson, P. (2000), "SMC materials – including present and future applications", *PM2TEC 2000*, New York, USA.

Jiles, D. C., Atherton, D. L. (1983), "Ferromagnetic hysteresis", *IEEE Transactions on Magnetics*, vol. 19, no. 5, pp. 2183-2185.

Jiles, D. C., Atherton, D. L. (1986), "Theory of ferromagnetic hysteresis", *Journal of Magnetism and Magnetic Materials*, vol. 61, no. 1-2, pp. 48-60.

Jiles, D. C., Thoelke, J. B., Devine, M. K. (1992), "Numerical determination of hysteresis parameters for the modeling of magnetic properties using the theory of ferromagnetic hysteresis", *IEEE Transactions on Magnetics*, vol. 28, no. 1, pp. 27-35.

Jiles, D. C. (1998), *Introduction to magnetism and magnetic materials*. Chapman & Hall, ISBN 0-412-79860-3.

Kordecki, A., Weglinski, B., (1990), "Development and applications of soft magnetic PM materials", *Powder Metallurgy*, vol. 33, no. 2, pp. 151-155.

Krause, R. F., Bularzik, J. H., Kokal, H. R., (1998), "Alternating current magnetic properties of cores made from pressed acicular steel particles", *Journal of Applied Physics*, vol. 83, no. 11, 6477-6479.

Lee, R., Stephens, D. S., (1973), "Influence of core gap in design of current-limiting transformers", *IEEE Transactions on Magnetics*, vol. 9, no. 3, pp. 408-410.

Lee, R., Wilson, L., Carter, C. E., (1988), *Electronic transformers and circuits*. Wiley, ISBN 0-471-81976-X.

Mayergoyz, I. D, (1986), "Mathematical models of hysteresis", *IEEE Transactions on Magnetics*, vol. 22, no. 5, pp. 603-608.

Mayergoyz, I. D, (1988), "Dynamic Preisach models of hysteresis", *IEEE Transactions on Magnetics*, vol. 24, no. 6, pp. 2925-2927.

McLyman, W. T., (1978), *Transformer and inductor design handbook*. Marcel Dekker, ISBN 0-8247-6801-9.

Naidu, S. R. (1990), "Simulation of the hysteresis phenomenon using Preisach's theory", *IEE Proceedings A*, vol. 137, no. 2, pp. 73-79.

Pelletier, S., Gélinas, C., Lefebvre, L.-P., (1998), "Effect of thermal cycling on properties of soft magnetic iron-resin composites", *Advances in Powder Metallurgy & Particulate Materials*, part 8, 1998.

Preisach, F. (1935), "Über die magnetische nachwirkung", *Zeitschrift für Physik*, vol. 94, pp. 277-302.

Sellers, C. H., Hyde, T. A. (1997), "Soft magnetic composites for applications in ac electrical components", *MPIF 1997 Magnetics Seminar*, Indianapolis, USA.

Skarrie, H. (2000), "A resonant system for determination of inductor parameters", *NORPIE 2000*, Aalborg, Denmark, June, 2000.

Smith, S. (1985), *Magnetic components, design and applications*. Van Nostrand, ISBN 0-442-20397-7.

Snelling, E. C. (1988), *Soft ferrites, properties and applications*. Butterworths, ISBN 0-408-02760-6 .

Stoll, R. L. (1974), *The analysis of eddy currents*. Oxford University Press, ISBN 0-19-859311-2.

Surahammars Bruk AB (1998), *Non-oriented fully processed electrical steels*, Product Guide, Surahammars Bruk AB, Sweden

Takajo, S., Ozaki, Y. (1998), "Frequency dependence of the permeability and iron loss of iron powder dust cores for high frequency applications", *Proceedings of PCIM INTER '98*, Japan.

Watson, G. N. (1944), *A treatise on the theory of bessel functions*. Capital City Press, ISBN 0-521-09382.

Zhu, J. (1994), *Numerical modelling of magnetic materials for computer aided design of electromagnetic devices*. PhD thesis, University of Technology, Sydney.

Appendix A

Equations for the Preisach model

With a magnetic field, H, applied the Preisach model calculates the corresponding flux density, B, following the hysteresis loop, by

$$B = \int_{S+} \mu(\alpha,\beta)\,d\alpha d\beta - \int_{S-} \mu(\alpha,\beta)\,d\alpha d\beta \tag{A.1}$$

For practical use of the model the distribution function of dipoles, $\mu(\alpha,\beta)$, must be determined. A way to relate the calculation of flux density to a Preisach diagram determined by a limiting hysteresis loop is suggested by (Zhu, 1994), where the only input data needed for hysteresis modelling is the limiting loop. The suggested method is described here, a more careful description is made in (Zhu, 1994).

Initial magnetisation

When magnetising a material from the demagnetised state, Figure A.1 a, it follows the initial magnetisation curve, from the Preisach diagram in Figure A.1 b the flux density on this curve is calculated by

$$\begin{aligned} B_i(H) &= \int_{S+} \mu(\alpha,\beta)\,d\alpha d\beta - \int_{S-} \mu(\alpha,\beta)\,d\alpha d\beta = \\ &= \int_{\Delta ABC} \mu(\alpha,\beta)\,d\alpha d\beta = T(H,-H) \end{aligned} \tag{A.2}$$

where

$$T(\alpha,\beta)=\int_{\beta}^{\alpha}\int_{y}^{\alpha}\mu(x,y)dxdy=\int_{\beta}^{\alpha}\int_{\beta}^{x}\mu(x,y)dydx \tag{A.3}$$

is the area integration of the triangle ABC with vertex (α,β) in figure A.1 b, $T(\alpha,\beta) = T(-\beta,-\alpha)$, since $\mu(\alpha,\beta) = \mu(-\beta,-\alpha)$ and $T(\alpha,\alpha) = 0$.

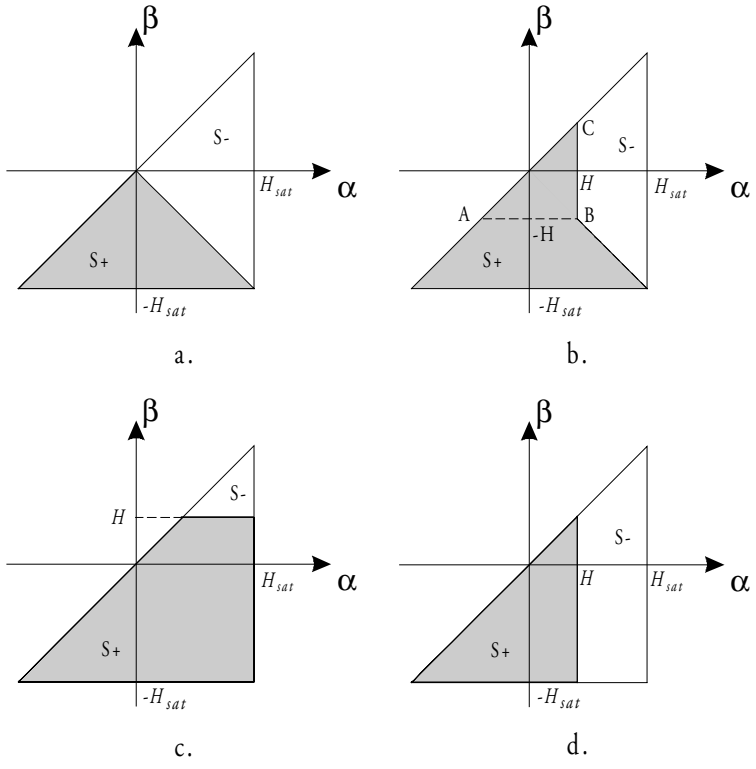

Figure A.1: Preisach diagram of
a. unmagnetised state
b. magnetisation along initial curve
c. downward trajectory of the limiting loop
d. upward trajectory of the limiting loop

Downward trajectory of the limiting loop

After saturation the applied field is decreased and the flux density follows the downward, upper, trajectory of the limiting hysteresis loop, calculated by

$$\begin{aligned} B_d(H) &= \int_{S+} \mu(\alpha,\beta)d\alpha d\beta - \int_{S-} \mu(\alpha,\beta)d\alpha d\beta = \\ &= B_i(H_{sat}) - 2T(H_{sat},H) \end{aligned} \tag{A.4}$$

Upward trajectory of the limiting loop

After negative saturation the applied field is increased, the flux density now follows the upward, lower, trajectory of the limiting loop, which is calculated by

$$\begin{aligned} B_u(H) &= \int_{S+} \mu(\alpha,\beta)d\alpha d\beta - \int_{S-} \mu(\alpha,\beta)d\alpha d\beta = \\ &= -B_i(H_{sat}) + 2T(H,-H_{sat}) \end{aligned} \tag{A.5}$$

General situation

In a general situation, where the downward and upward trajectory not necessarily follows the limiting loop, the flux density after n reversal points can be expressed as

$$B(H) = B(H_n) - 2T(H_n,H) \tag{A.6}$$

on a downward trajectory, and

$$B(H) = B(H_n) + 2T(H,H_n) \tag{A.7}$$

on a upward trajectory. The index n denotes the last reversal point, H_n the magnetic field at the last reversal point and $B(H_n)$ the corresponding flux density.

Parameter identification

To be able to calculate the flux density by (A.6) and (A.7) the parameter $T(\alpha,\beta)$ must be identified. From the Preisach diagrams of Figure A.1 c and d the following can be derived

$$T(\alpha,\beta)=\frac{B_u(\alpha)-B_d(\beta)}{2}+\int_{-H_{sat}}^{\beta}\int_{\alpha}^{H_{sat}}\mu(x,y)dxdy \tag{A.8}$$

In order to separate the α- and β- dependence of the distribution function, $\mu(\alpha,\beta)$, a function transform is suggested by (Naidu, 1990)

$$\mu(\alpha,\beta) = m_A(\alpha)m_B(\beta)$$

$$\mu(-\beta,-\alpha) = m_A(-\beta)m_B(-\alpha)$$

The symmetry condition $\mu(\alpha,\beta) = \mu(-\beta,-\alpha)$ gives $m_A(\alpha)m_B(\beta) = m_A(-\beta)m_B(-\alpha)$. Therefore the transform functions can be related as

$$m_A(\alpha) = m_B(-\alpha)$$

$$m_B(\beta) = m_A(-\beta)$$

and

$$\mu(\alpha,\beta) = m_A(\alpha)m_B(\beta) = m_A(\alpha)m_A(-\beta)$$

Then (A.8) becomes,

$$\begin{aligned}T(\alpha,\beta)&=\frac{B_u(\alpha)-B_d(\beta)}{2}+\int_{\alpha}^{H_{sat}}m_A(x)dx\int_{-H_{sat}}^{\beta}m_A(-y)dy=\\&=\frac{B_u(\alpha)-B_d(\beta)}{2}+\int_{\alpha}^{H_{sat}}m_A(x)dx\int_{-\beta}^{H_{sat}}m_A(y)dy=\\&=\frac{B_u(\alpha)-B_d(\beta)}{2}+F(\alpha)F(-\beta)\end{aligned} \tag{A.9}$$

where

$$F(\alpha)=\int_{\alpha}^{H_{sat}}m_A(x)dx$$

From Figures A.1 b - d, when $H \geq 0$, the upward respectively the downward trajectory of the limiting loop and the initial magnetisation curve also can be expressed in terms of $F(H)$ and $F(-H)$ as

$$\begin{aligned} B_u(H) &= B_i(H) - \int_{H}^{H_{sat}} m_A(\alpha)d\alpha \int_{-H_{sat}}^{-H} m_A(-\beta)d\beta = \\ &= B_i(H) - \int_{H}^{H_{sat}} m_A(\alpha)d\alpha \int_{H}^{H_{sat}} m_A(\beta)d\beta = \\ &= B_i(H) - F^2(H) \end{aligned} \tag{A.10}$$

$$\begin{aligned} B_d(H) &= B_u(H) + 2\int_{H}^{H_{sat}} m_A(\alpha)d\alpha \int_{-H_{sat}}^{H} m_A(-\beta)d\beta = \\ &= B_u(H) + 2\int_{H}^{H_{sat}} m_A(\alpha)d\alpha \int_{-H}^{H_{sat}} m_A(\beta)d\beta = \\ &= B_u(H) + 2F(H)F(-H) \end{aligned} \tag{A.11}$$

$$\begin{aligned} B_i(H) &= \int_{-H}^{H} m_A(\alpha)d\alpha \int_{-H}^{H} m_A(-\beta)d\beta = \\ &= \int_{-H}^{H} m_A(\alpha)d\alpha \int_{-H}^{H} m_A(\beta)d\beta = \\ &= \left[F(-H) - F(H)\right]^2 \end{aligned} \tag{A.12}$$

From these equations $F(H)$ can be solved, (A.12) gives

$$B_i(H) = F^2(-H) + F^2(H) - 2F(-H)F(H)$$

and together with (A.10) and (A.11)

$$B_u(H) + F^2(H) = F^2(-H) + F^2(H) - B_d(H) + B_u(H)$$

That simplifies to

$$F^2(-H) = B_d(H)$$

and

$$F(-H) = \sqrt{B_d(H)}$$

(A.11) also gives

$$F(H) = \frac{B_d(H) - B_u(H)}{2F(-H)} = \frac{B_d(H) - B_u(H)}{2\sqrt{B_d(H)}}$$

Therefore,

$$F(H) = \frac{B_d(H) - B_u(H)}{2\sqrt{B_d(H)}}, \qquad H \geq 0 \tag{A.13}$$

$$F(H) = \sqrt{B_d(-H)}, \qquad H < 0 \tag{A.14}$$

Appendix B

Properties of iron powder materials

Two different Soft Magnetic Composite (SMC) materials, manufactured by Höganäs AB, are used in this thesis. Both materials are based on Somaloy 500, a water atomised highly pure iron powder particle with an oxide surface coating serving as an electrical insulator.

The first material has optimised magnetic properties and is suitable for low frequency applications. It is achieved by mixing the particles with 0.5% lubricant (Kenolube).

The second material exhibits a slight decrease in magnetic properties but an increase in resistivity, which makes it suitable for higher frequency applications. It is achieved by a mix with 0.6% lubricating binder (LB1). The use of a lubricating binder also improves the strength.

Both materials are compacted at 800 MPa and heat treated in air, Somaloy 500 + 0.5% Kenolube at 500°C for 30 minutes and Somaloy 500 + 0.6% LB1 at 275°C for 60 minutes.

In Table B.1 a summary of some material properties of the two materials are listed. The magnetic properties are based on measurements on a ring sample with the geometrical dimensions:

outer diameter	55 mm
inner diameter	45 mm
height	5 mm

The power loss factors are used to calculate core losses. In Equation (3.55) the core losses are divided into static and dynamic parts (k_h, n, k_{dyn}, n_B and n_f

are used), while in (3.53) and (3.54) the losses are divided into hysteresis, anomalous and eddy current loss (k_h, n, k_a and k_{ec} are used).

	+ 0.6% LB1	**+ 0.5% Kenolube**
Max flux density, B_{max} @ H = 100 kA/m	2.0 T	2.1 T
Remanence, B_m	0.13 T	0.25 T
Coercive force, H_c	400 A/m	250 A/m
Resistivity, ρ	> 1000 μΩm	30 μΩm
Thermal conductivity, λ	16 W/(m°C)	17 W/(m°C)
Max permeability, μ_{max}	200	500
Initial permeability, μ_i	80	130
Density	7200 kg/m^3	7400 kg/m^3
Strength (TRS)	100 MPa	50 MPa
Power loss factors		
Static loss (hysteresis):		
k_h	1160	880
n	1.6	1.7
Dynamic loss (eddy current + anomalous):		
k_{dyn}	57	880
n_B	1.85	1.35
n_f	1.40	1.45
Anomalous: k_a	3.6	1.4
Eddy current: k_{ec}	0	0

Table B.1: A summary of material properties of the two used iron powder materials, with a slight difference in composition and fabrication process.

Appendix C

Winding ac resistance

A single solid conductor, with diameter d, not exposed to any external field will only be subjected to skin effect. The exact analytical solution of the ac resistance of the single solid conductor is determined by (Stoll, 1974) and is also described here.

Maxwell's equations state

$$\operatorname{curl}\mathbf{E} = -\frac{\partial \mathbf{B}}{\partial t} = -\frac{dB}{dH}\frac{\partial \mathbf{H}}{\partial t} \tag{C.1}$$

$$\operatorname{curl}\mathbf{H} = \mathbf{J} \tag{C.2}$$

$$\operatorname{div}\mathbf{B} = 0 \tag{C.3}$$

The relation between the electric field strength and current density is

$$\mathbf{J} = \frac{\mathbf{E}}{\rho} \tag{C.4}$$

with the resistivity of copper ρ. The permeability of free space, μ_0, and the relative permeability, μ_r, determines the relation between the magnetic field and the flux density.

$$\mathbf{B} = \mu_0 \mu_r \mathbf{H} = \mu \mathbf{H} \tag{C.5}$$

Combining (C.2) and (C.4) gives

$$\text{curl curl}\,\mathbf{H} = \text{curl}\,\frac{\mathbf{E}}{\rho} \tag{C.6}$$

that can be written as

$$\text{grad div}\,\mathbf{H} - \nabla^2\mathbf{H} = \frac{1}{\rho}\,\text{curl}\,\mathbf{E} + (\text{grad}\,\frac{1}{\rho}) \times \mathbf{E} \tag{C.7}$$

Equation (C.3) together with (C.5) gives

$$\text{div}\,\mathbf{B} = \text{div}\,\mu\mathbf{H} = \mu\,\text{div}\,\mathbf{H} + \mathbf{H}\,\text{grad}\,\mu \tag{C.8}$$

thereby

$$\text{div}\,\mathbf{H} = -\mathbf{H}\frac{1}{\mu}\,\text{grad}\,\mu \tag{C.9}$$

Now (C.7), with (C.1), (C.2), (C.4) and (C.9), becomes

$$\nabla^2\mathbf{H} = \frac{1}{\rho}\frac{dB}{dH}\frac{\partial\mathbf{H}}{\partial t} - \text{grad}\,(\mathbf{H}\frac{1}{\mu}\,\text{grad}\,\mu) - \rho(\text{grad}\,\frac{1}{\rho}) \times \text{curl}\,\mathbf{H} \tag{C.10}$$

In a linear magnetic material with constant resistivity (C.10) can be simplified to

$$\nabla^2\mathbf{H} = \frac{1}{\rho}\mu_0\mu_r\frac{\partial\mathbf{H}}{\partial t} \tag{C.11}$$

If a current flowing along the axis of the conductor, and the axis correspond to the z-direction of a cylindrical coordinate system, the magnetic field generated by the current will be in the φ-direction and independent of φ and z. Then $\mathbf{H} = H_\varphi$ and

$$(\nabla^2\mathbf{H})_\varphi = \frac{d^2H_\varphi}{dr^2} + \frac{1}{r}\frac{dH_\varphi}{dr} - \frac{H_\varphi}{r^2} \tag{C.12}$$

With a sinusoidal magnetic field $\partial/\partial t$ can be substituted with $j\omega$, then (C.11) becomes

$$\frac{d^2H}{dr^2} + \frac{1}{r}\frac{dH}{dr} - \left(\alpha^2 + \frac{1}{r^2}\right)H = 0 \tag{C.13}$$

where

$$\alpha^2 = j\frac{\omega\mu_0\mu_r}{\rho} = j\frac{2}{\delta^2} \tag{C.14}$$

δ is the skin depth. (C.13) has the solution

$$H = AI_1(\alpha r) + BK_1(\alpha r) \tag{C.15}$$

with $I_1(\alpha r)$ and $K_1(\alpha r)$ first-order modified Bessel functions of the first respectively the second kind. The coefficients A and B are found by applying the boundary conditions. In the centre, $r = 0$, $K_1(\alpha r)$ goes to infinity but H must be finite, that gives $B = 0$. At the surface, $r = d/2$, Ampere's law gives $H = I / \pi d$. Then

$$H = \frac{I}{\pi d}\frac{I_1(\alpha r)}{I_1(\alpha d/2)} \tag{C.16}$$

In the cylindrical coordinates (C.2) is expressed as

$$J = \frac{1}{r}\frac{d}{dr}(rH) = \frac{dH}{dr} + \frac{H}{r} \tag{C.17}$$

and

$$J = \frac{I}{\pi d}\frac{1}{I_1(\alpha d/2)}\left(\frac{d}{dr}\left[I_1(\alpha r)\right] + \frac{1}{r}I_1(\alpha r)\right) = \frac{\alpha I}{\pi d}\frac{I_0(\alpha r)}{I_1(\alpha d/2)} \tag{C.18}$$

The impedance per unit length of the conductor becomes

$$Z = \left(\frac{E}{I}\right)_{r=d/2} = \left(\frac{\rho J}{I}\right)_{r=d/2} = \frac{\alpha\rho}{\pi d}\frac{I_0(\alpha d/2)}{I_1(\alpha d/2)} \tag{C.19}$$

α is complex, hence the Bessel functions can be separated into real and imaginary parts. The real part of (C.19) corresponds to the resistance per unit length of the conductor

$$r = \gamma\frac{2\rho}{\pi d^2}\frac{\mathrm{ber}\,\gamma\,\mathrm{bei}'\gamma - \mathrm{bei}\,\gamma\,\mathrm{ber}'\gamma}{\mathrm{ber}'^2\gamma + \mathrm{bei}'^2\gamma} \tag{C.20}$$

with, $\gamma = |\alpha|d/2$. The real and imaginary parts of the Bessel functions, ber respectively bei, are tabulated in for example (Watson, 1944) and are also found in Appendix D.

With the dc resistance of the conductor per unit length expressed by

$$r_{dc} = \frac{4\rho}{\pi d^2} \tag{C.21}$$

the ac resistance in a solid round conductor due to skin effect is

$$R_{skin} = R_{dc}\frac{\gamma}{2}\frac{\mathrm{ber}\gamma\,\mathrm{bei}'\gamma - \mathrm{bei}\gamma\,\mathrm{ber}'\gamma}{\mathrm{ber}'^2\gamma + \mathrm{bei}'^2\gamma} \tag{C.22}$$

with, from (C.14),

$$\gamma = \frac{d}{\sqrt{2}\delta} \tag{C.23}$$

Finally, the skin effect loss in the winding is calculated by

$$P_{skin} = R_{skin} I_{rms}^2 \tag{C.24}$$

The winding loss due to the proximity effect is calculated by

$$P_{prox} = G_{prox} H_e^2 \tag{C.25}$$

where H_e is the external field generated by the winding as a whole and G_{prox} is calculated in (Ferreira, 1989) for a solid round conductor

$$G_{prox} = -2\pi\rho\gamma\frac{\mathrm{ber}_2\gamma\,\mathrm{ber}'\gamma + \mathrm{bei}_2\gamma\,\mathrm{bei}'\gamma}{\mathrm{ber}^2\gamma + \mathrm{bei}^2\gamma} \tag{C.26}$$

The total ac resistance can be calculated if the round conductor is replaced with a square-shaped conductor of equal cross sectional area and under the assumption of a high permeability core and a winding that fills the entire winding window. The one-dimensional solution of the total ac resistance of the mth layer, due to skin and proximity effect, is (Ferreira, 1994)

$$R_{ac} = R_{dc}\frac{\xi}{2}\left[\frac{\sinh\xi + \sin\xi}{\cosh\xi - \cos\xi} + (2m-1)^2\frac{\sinh\xi - \sin\xi}{\cosh\xi + \cos\xi}\right] \tag{C.27}$$

with

$$\xi = \frac{\sqrt{\pi}d}{2\delta} \tag{C.28}$$

If the external field is assumed to be uniform over the conductor cross section (Ferreira, 1989) shows that an orthogonality exists between eddy

currents due to skin effect respectively proximity effect. This othogonality gives that the two eddy current parts can be calculated separately and then adding the terms together to calculate the total eddy current loss. In (Ferreira, 1994) it is shown that due to the orthogonality (C.22) and (C.26) can be substituted into (C.27). The ac resistance of the *m*th layer in a winding composed of a solid round conductor is

$$R_{ac} = R_{dc}\frac{\gamma}{2}\left[r_{skin} - 2\pi(2m-1)^2 r_{prox}\right] \tag{C.29}$$

with

$$r_{skin} = \frac{\mathrm{ber}\gamma\,\mathrm{bei}'\gamma - \mathrm{bei}\gamma\,\mathrm{ber}'\gamma}{\mathrm{ber}'^2\gamma + \mathrm{bei}'^2\gamma} \tag{C.30}$$

$$r_{prox} = \frac{\mathrm{ber}_2\gamma\,\mathrm{ber}'\gamma + \mathrm{bei}_2\gamma\,\mathrm{bei}'\gamma}{\mathrm{ber}^2\gamma + \mathrm{bei}^2\gamma} \tag{C.31}$$

For a non-sinusoidal current the orthogonality also gives that the losses for each frequency component can be calculated separately and then added together to the total winding loss.

Appendix D

Bessel functions

The real, ber, and imaginary part, bei, of Bessel functions written as infinite sums (Watson, 1944). Zero order, second order respectively derivative of zero order

$$\mathrm{ber}(z) = \sum_{k=0}^{\infty} (-1)^k \frac{1}{((2k)!)^2} \left(\frac{z}{2}\right)^{4k} \tag{D.1}$$

$$\mathrm{bei}(z) = \sum_{k=0}^{\infty} (-1)^k \frac{1}{((2k+1)!)^2} \left(\frac{z}{2}\right)^{4k+2} \tag{D.2}$$

$$\mathrm{ber}_2(z) = \sum_{k=0}^{\infty} (-1)^k \frac{1}{(2k+1)!(2k+3)!} \left(\frac{z}{2}\right)^{4k+4} \tag{D.3}$$

$$\mathrm{bei}_2(z) = \sum_{k=0}^{\infty} (-1)^{k+1} \frac{1}{(2k)!(2k+2)!} \left(\frac{z}{2}\right)^{4k+2} \tag{D.4}$$

$$\mathrm{ber}'(z) = \frac{\partial}{\partial z} \mathrm{ber}(z) = \sum_{k=1}^{\infty} (-1)^k \frac{2k}{((2k)!)^2} \left(\frac{z}{2}\right)^{4k-1} \tag{D.5}$$

$$\mathrm{bei}'(z) = \frac{\partial}{\partial z} \mathrm{bei}(z) = \sum_{k=1}^{\infty} (-1)^k \frac{2k+1}{((2k+1)!)^2} \left(\frac{z}{2}\right)^{4k+1} \tag{D.6}$$

Appendix E

Conductor table

Table taken from (Snelling, 1988).

Copper diameter, nominal	Overall diameter, maximal	Copper diameter, nominal	Overall diameter, maximal
mm	mm	mm	mm
1.000	1.093	2.360	2.488
1.060	1.155	2.500	2.631
1.120	1.217	2.650	2.784
1.180	1.279	2.800	2.938
1.250	1.351	3.000	3.142
1.320	1.423	3.150	3.294
1.400	1.506	3.350	3.498
1.500	1.608	3.550	3.702
1.600	1.711	3.750	3.905
1.700	1.813	4.000	4.160
1.800	1.916	4.250	4.414
1.900	2.018	4.500	4.668
2.000	2.120	4.750	4.923
2.120	2.243	5.000	5.177
2.240	2.366		

Table E.1: Enamelled solid round copper conductors, Grade 2.